# Multiscale simulation of elongated particles in fluidised beds

Fitzgerald, Barry W.; Zarghami, Ahad; Mahajan, Vinay V.; Sanjeevi, Sathish K.P.; Mema, Ivan; Vikrant, Vikrant; El Hasadi, Yousef M.F.; Padding, Johan T.

**Important note**
To cite this publication, please use the final published version (if applicable).
Please check the document version above.

# Multiscale simulation of elongated particles in fluidised beds

Barry W. Fitzgerald *, Ahad Zarghami, Vinay V. Mahajan, Sathish K.P. Sanjeevi, Ivan Mema, Vikrant Verma, Yousef M.F. El Hasadi, Johan T. Padding *

*Delft University of Technology, Process & Energy Department, Complex Fluid Processing, Leeghwaterstraat 39, 2628 CB Delft, The Netherlands*

## ARTICLE INFO

## ABSTRACT

In this paper, we present a number of key numerical methods that can be used to study elongated particles in fluid flows, with a specific emphasis on fluidised beds. Fluidised beds are frequently used for the production of biofuels, bioenergy, and other products from biomass particles, which often have an approximate elongated shape. This raises numerous issues in a numerical approach such as particle-particle contact detection and the accurate description of the various hydrodynamic forces, such as drag, lift, and torque, that elongated particles experience when moving in a fluid flow. The modelling is further complicated by a separation of length scales where industrial flow structures that can extend for many metres evolve subject to solid-solid and solid-fluid interactions at the millimetre scale. As a result, it is impossible to simulate both length scales using the same numerical approach, and a multiscale approach is necessary. First, we outline the direct numerical simulation (DNS) approach that may be employed to estimate hydrodynamic force closures for elongated particles in a fluid flow. We then describe the key aspects of a CFD-DEM approach, which can be used to simulate laboratory scale fluidisation processes, that must be addressed to study elongated particles. Finally, we briefly consider how current industrial-scale models, which concretely assume particle sphericity, could be adapted for the simulation of large collections of elongated particles subject to fluidisation.

## 1. Introduction

Numerous industrial operations involve the processing of multiphase flows, which can be defined as flows that consist of more than one distinctive phase or component. Such flows are frequently encountered in the chemical (Kapteijn et al., 2001; Stitt, 2002; Kreutzer et al., 2005; Son and Kim, 2006; Mattisson et al., 2018), food (Norton and Sun, 2006; Kumar et al., 2007; Joardder et al., 2017; Azmir et al., 2018), pharmaceutical (Ricard et al., 2005; Kremer and Hancock, 2006; Gutmann et al., 2015; Tong et al., 2017), petrochemical (Williams and Williams, 1999; Gao et al., 2015; Xue et al., 2016; Valus et al., 2017; Aydin and Larachi, 2005), and bioenergy industries (Cui and Grace, 2007; Nikoo and Mahinpey, 2008; Svoboda et al., 2009; Molino et al., 2016; Pio et al., 2017). Multiphase flows are treated in a variety of equipment such as packed bed reactors (Jafari et al., 2008; Dasgupta and Atta, 2018; Li et al., 2018), fluidised bed reactors (Alauddin et al., 2010; Paudel and Feng, 2013; Hejazi et al., 2014; Molino et al., 2016; Zhong et al., 2016), cyclone separators (Cortes and Gil, 2007; Chu et al., 2011; Zhou et al., 2018), airlift tower loop reactors (Lbbert and Larson, 1990; Dejaloud et al., 2018), combustors (Cheng and Farmer, 2006; Bauerheim et al., 2015; Mei et al., 2017), and fermenters (Trad et al., 2016; Zhang et al., 2012; Desobgo, 2018). Hence, a thorough understanding of the behaviour of multiphase flows can have implications for the formulation and efficiency of processes, the fundamental design of equipment, and the choices made in relation to the materials that constitute multiphase flows.

The simplest multiphase flow is a two-phase flow, where one phase is an interstitial liquid or gas and the second phase is a mixture of solid particles. In particular, multiphase flows in many fluidisation processes can be categorised as dense gas-solid flows where particle-particle interactions are dominant due to the large number of solid particles transported in the flow (van der Hoef et al., 2008). In the bioenergy industry, dense gas-solid fluidised beds are frequently used for biomass gasification in the production of biofuels and bioenergy. To facilitate the fluidisation process and augment pyrolysis, the biomass material is typically fluidised in the presence of an inert material such as sand (Paudel and Feng, 2013). While fluidised bed reactors can process different types of biomass, challenges remain in the gasification and downstream processing of biomass in such reactors for viable commercial applications (Kumar et al., 2009). The challenges with gasification are to understand the influence of variable operating conditions

on gasification reactions for the reliable prediction and optimisation of product compositions, and for obtaining maximal efficiencies. Characterisation of the hydrodynamics of, and coupled to this the heat and mass transfer in, multiphase flows consisting of biomass particles can directly impact the design and operation of fluidised bed reactors, and is thus imperative for the economic viability of future gasification energy conversion processes (Cui and Grace, 2007).

Traditional efforts to study gasification processes in the laboratory routinely involve the construction of replicas of industrial scale equipment. With regards to the hydrodynamics, such apparatus can allow for the measurement of particle dynamics using approaches such as magnetic particle tracking (MPT) (Buist et al., 2017), where the trajectory of a single magnetic tracer particle is tracked through a reactor, or Particle Tracking Velocimetry (PTV) (Mahajan et al., 2018), which can concurrently estimate the velocity of multiple particles in the reactor. However, the construction of laboratory experiments can be both costly and time consuming, requiring extensive calibration and validation before utilising the apparatus for dedicated investigations. In reality, laboratory apparatus are simply scaled-down versions of industrial apparatus, and as a result they cannot capture certain flow behaviours that may be dependent on the length scale of the reactor.

An alternative approach for the study of fluidisation processes is via numerical simulations, which have numerous advantages over laboratory experiments. Firstly, numerical codes can be quickly created and evaluated in comparison to the development of preliminary laboratory-scale prototypes of industrial designs. Secondly, numerical codes are reusable and easily adapted to simulate other apparatus. An experimental apparatus may have to undergo significant reconstruction and redesign to study another process. Thirdly, numerical codes are relatively cheap to develop in comparison to experimental setups. Fourthly, a numerical code can also be used to safely study operational conditions that would otherwise be dangerous in laboratory or industrial settings. Finally, numerical simulations allow for access to information that would be difficult to measure in experimental or industrial apparatus. Nonetheless, the simulation of the processing of multiphase flows in industrial fluidised bed reactors is complicated by mainly two factors; namely particle shape and size distribution, and the large separation of relevant length scales.

Biomass particles in fluidised beds are inherently non-spherical, typically elongated, with a large range of particle sizes (Cui and Grace, 2007; Guo et al., 2012). Examples of microscopic images of elongated biomass particles and pellets are shown in Fig. 1. In comparison to spherical particles, elongated particles have a larger surface area-to-volume ratio, which can promote greater heat and mass transfer rates as well as affect the devolatilisation of the biomass (Lu et al., 2010). Biomass particles, and certainly pelletised biomass, are typically large (with a Sauter mean diameter larger than a millimetre), making them part of the Geldart D group (Geldart, 1973). Such particles require a large fluidisation velocity and can form large bubbles. Group D particles have been the subject of recent investigations in laboratory scale fluidised beds (Kruggel-Emden and Vollmari, 2016; Mahajan et al., 2018).

Typically, biomass particles are fluidised in a mixture with an inert material such as sand, alumina, or calcite to overcome difficulties in the fluidisation and promote faster pyrolysis. Nonetheless, there have been numerous experimental studies on the fluidisation response of packings consisting of elongated biomass-like particles only (Vollmari et al., 2015; He et al., 2016; Kruggel-Emden and Vollmari, 2016; Vollmari et al., 2016; Mahajan et al., 2017, 2018; Rezaei et al., 2018), motivated not only by the use of biomass particles in fluidised bed reactors, but also in other industrial processes where biomass particles are integral. In these experimental studies, imaging of the fluidisation process is
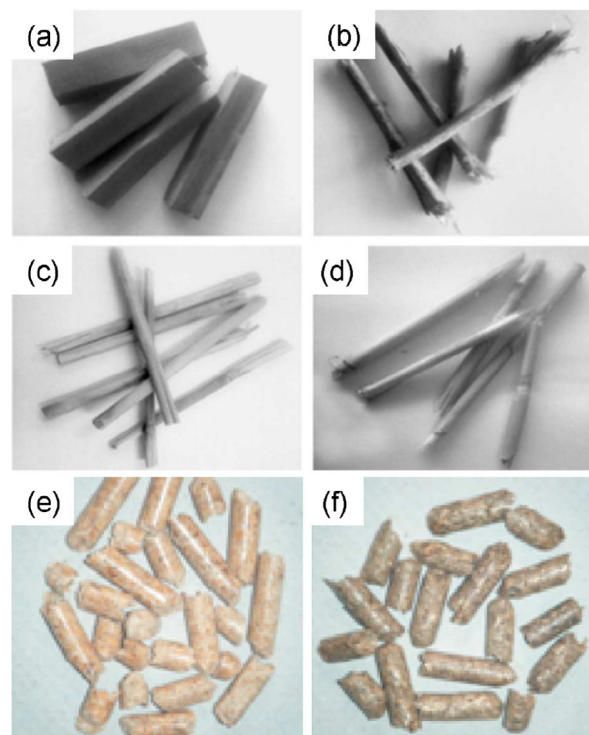


Fig. 1. (a)–(d): Microscopic images of various biomass materials demonstrating their elongated nature after pre-treatment. (a) Pine. (b) Beanstalk. (c) Rice straw. (d) Reed. Images taken from Guo et al. (2012). (e) and (f): Images of processed pellets. (e) Grass pellet. (f) Wood pellet. Images taken from Roy et al. (2013).

commonplace, typically via the use of high resolution cameras (Vollmari et al., 2016; Mahajan et al., 2018). Post-processing routines such as Digital Image Analysis (DIA), Particle Image Velocimetry (PIV), and Particle Tracking Velocimetry (PTV) can subsequently be used to ascertain bed height, particle orientation, particle coalignment, void fraction, and particle coordination number (Vollmari et al., 2016; Mahajan et al., 2018).

For simplicity, in most numerical studies of fluidised beds, particles are treated as idealised spheres subject only to drag for ease of computation, with the other hydrodynamical forces deemed to have negligible effects on particle dynamics (Tsuji et al., 1993; Hoomans et al., 1996; Xu and Yu, 1997; Deen et al., 2007; Zhu et al., 2008; van der Hoef et al., 2006, 2008). Capturing the true shape of real biomass particles, which are elongated, severely complicates the detection of particle-particle contacts and associated contact forces. In addition to hydrodynamic drag, elongated particles are also subject to hydrodynamic lift, pitching torque, and rotational torque, which are dependent on particle orientation relative to the incoming fluid flow. These additional hydrodynamic forces can appreciably affect the trajectory of elongated particles in fluidised beds and must be accounted for in any numerical study involving elongated particles.

To accurately model multiphase flows relevant for the industrial scale, where flow structures can extend over the order of metres, we need information on the particle scale, where the typical size of particles is of the order of millimetres. Due to this separation of length scales, it is impossible to capture both the particle scale and industrial scale simultaneously in a numerical scheme without sacrificing computational efficiency and lengthening computation time. For the case of a complex system such as a fluidised bed, a multiscale simulation approach must allow for correlation of different phenomena between length scales, to couple both spatial and temporal variations, and identify the emergent critical phenomena (Li et al., 2004). Instead of a single simulation algorithm,

a suite of algorithms is thus required, with each algorithm focusing on a specific length scale. For a fluidised bed reactor, this equates to algorithms that can capture responses at the particle scale, laboratory scale and, ultimately, the industrial scale.

The idea of using a multiscale approach to model fluidised beds is certainly not new; it has been reviewed extensively in the literature (van der Hoef et al., 2006, 2008). Most previous multiscale modelling methods papers have focused on spherical particles. However, such an interpretation of particle shape is not representative of real systems where biomass units are non-spherical or elongated in nature. Therefore, in this paper, we present the numerical methods and associated considerations that are of greatest relevance for the study of fluidised biomass. In particular, we highlight the differences and peculiarities that arise when one models fluidised beds consisting of elongated particles as opposed to spherical particles. At the particle scale, we outline a direct numerical simulations (DNS) approach that can be used to evaluate the varying hydrodynamic forces experienced by elongated particles subject to varying particle orientation and flow conditions (Section 3). Such simulations lead to correlations that can be incorporated in coupled computational fluid dynamics - discrete element method (CFD-DEM) simulations, which are suitable for the simulation of laboratory scale processes (Section 4). In CFD-DEM, collisions between elongated particles can be handled through the use of specific collision detection schemes. We also briefly consider how CFD-DEM simulations can be used to define constitutive relations that are specifically relevant for elongated particles that can be used in industrial-scale models. Such relations are currently unavailable in the literature. Finally, we consider the current status of industrial-scale models such as the two-fluid model (TFM) (Gidaspow, 1994; van der Hoef et al., 2008) and the multi-phase particle-in-cell (MP-PIC) method (Andrews and O'Rourke, 1996) (Section 5). TFM is based on expressions for solid stress that are traditionally derived from the Kinetic Theory of Granular Flow (KGTF) (Chapman et al., 1990), which assumes particle sphericity and isotropy, binary interactions, and uncorrelated pre-collisional velocities. Such assumptions are certainly not applicable for dense multiphase flows consisting of elongated particles, making the need for a proper flow of information from lower level models to these industrial-scale models much more urgent than in the case of spherical particles.

This paper is presented as follows. First, we give an overview of the multiscale approach before introducing details of the associated numerical approaches. For the algorithms at the particle scale (Section 3) and laboratory scale (Section 4), we present results from our own studies and compare findings with the state-of-the-art in the field. At the industrial scale (Section 5), we highlight the issues with defining an algorithm suitable for elongated particles, and suggest possible solutions and directions of future research. Although we focus here on the implementation of a multiscale approach for the fluidisation of elongated particles that approximate the shape of biomass feedstocks, the algorithms can be easily adapted and applied to study other unit operations where multiphase flows of non-spherical particles are relevant.

## 2. Overview of multiscale approach for fluidized bed modelling

As argued in the introduction, a multiscale modelling approach is a necessity to cover all relevant length scales in a fluidised bed. The algorithms that comprise a multiscale approach for multiphase flows can be distinguished by their treatment of the solid and fluid phases (van der Hoef et al., 2008) (Table 1). There are two primary methods for numerically describing the solid phase of a typical multiphase flow. First, the solid phase can be depicted as a set of dispersed or discrete particles that collide with each other and

**Table 1**
Treatment of the gas and solid phases in particle-scale, laboratory-scale and industrial-scale numerical algorithms.

| Scale | Numerical approach | Gas phase | Solid phase |
|---|---|---|---|
| Particle | DNS | Resolved | Lagrangian (deterministic collisions) |
| Laboratory | CFD-DEM | Resolved | Lagrangian (deterministic collisions) |
| Industrial | MP-PIC | Resolved | Lagrangian and Eulerian (implicit collisions) |
| Industrial | TFM | Resolved | Eulerian (implicit collisions) |

any rigid boundaries or walls in a geometry. Such particles follow trajectories that are evolved subject to Newton's laws of motion. This representation is referred to as *Lagrangian*. For the second representation, which is referred to as *Eulerian*, the solid phase is described using a continuum approach that may be based upon the Navier-Stokes equations, combined with a constitutive equation describing the solid phase rheology, where the phase is represented as a grid of cells with each cell containing information related to the phase properties. The fluid phase is usually also treated in such a continuum manner. The direct numerical simulation (DNS) approach (Deen et al., 2012, 2014; van der Hoef et al., 2006), which is presented in detail in Section 3, and the coupled computational fluid dynamics - discrete element method (CFD-DEM) approach (Deen et al., 2007; Mema et al., 2017, 2019; Mahajan et al., 2018), which is discussed in Section 4, are both so-called Lagrangian-Eulerian approaches since the solid phase is described in a discrete manner and the fluid is described as a continuum. The difference between the two approaches is that in DNS, the fluid flow around the particles is fully resolved by choosing sufficiently small fluid cells, while in CFD-DEM the fluid flow is unresolved, where fluid cells are much larger than a single particle. In both cases, the particle-particle collisions are treated deterministically, which is very expensive computationally, making these methods unsuitable for predictions at the industrial scale. To reach the industrial scale, it is necessary to make approximations to avoid the explicit deterministic treatment of particle collisions. The multiphase particle-in-cell (MP-PIC) method (Andrews and O'Rourke, 1996) and two-fluid model (TFM) (Lindborg et al., 2007) are two common approaches to deal with large scale simulations. In MP-PIC, the particles are simultaneously treated in a Lagrangian manner and as an Eulerian (continuum) field, where the effects of the collisions are treated implicitly from gradients in the continuum fields. In TFM, the particles are treated fully Eulerian, interpenetrating with the continuous fluid phase. Both approaches, and their amenability for extension to elongated particles, will be briefly described in Section 5.

Although a multiscale methodology has already been extensively described in the literature for spherical particles, e.g. van der Hoef et al. (2006, 2008) and Deen et al. (2007), in this paper, we focus on the new problems that emerge when dealing with elongated particles. Generally, we find that solving these new problems requires a strong coupling between the numerical models at different scales. In fact, the coupling is stronger than is usually required for spherical particles. The relationship between the numerical models is depicted in Fig. 2. A DNS approach is used to accurately resolve the fluid flow in the vicinity of $O(10^2–10^3)$ particles (Fig. 2(a)). Measurements from the DNS simulations can then be utilised to define hydrodynamic closures for drag, lift and torque for elongated particles subject to varying aspect ratio, orientation and Reynolds number. We present details on the DNS approach in Section 3.

For larger numbers of particles, a DNS approach is too computationally expensive. Instead, closures from DNS simulations can be
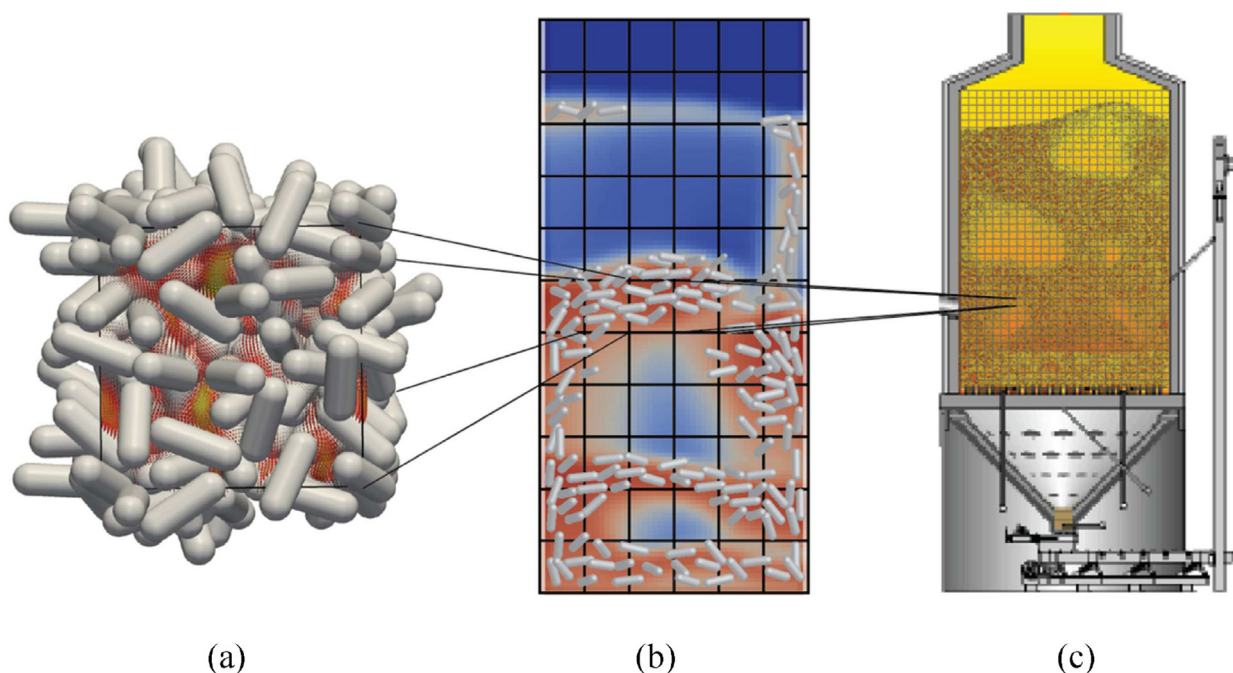
**Fig. 2.** Relationship between the numerical models at the different scales. (a) Direct numerical simulation (DNS) where the solid phase is represented in a discrete (Lagrangian) manner and the fluid flow around the particles is fully resolved. (b) Computational fluid dynamics – discrete element method (CFD-DEM) where the particles are discrete, but the fluid flow is no longer resolved at the particle scale. (c) Industrial scale model such as multiphase particle-in-cell (MP-PIC) where particles are still discrete, but the fluid flow is no longer resolved at the particle scale.

employed to couple the gas and discrete particle phases in a CFD-DEM approach where the fluid is solved on a grid that is larger than the elongated particles (Fig. 2(b)). For elongated particles, CFD-DEM has been applied to duplicate fluidization processes at the laboratory scale where the bed is composed of O($10^5$) particles (Vollmari et al., 2017; Mema et al., 2019; Mahajan et al., 2018). Details of the CFD-DEM approach are outlined in Section 4.

Although advancements in parallel programming permit CFD-DEM simulations of fluidised beds with millions of particles on dedicated parallel architectures, these studies generally represent the solid phase as spherical particles due to ease of contact detection and particle representation (Capecelatro and Desjardins, 2013; Amritkar et al., 2014). In addition, there is a necessity for expensive and often scarce parallel computing resources and the number of system particles can still be orders of magnitude less than the number in industrial settings. These issues can be somewhat addressed by considering a coarse-grained model of a fluidised bed (Fig. 2(c)). Rather than evaluating deterministic particle interactions as in CFD-DEM, a coarse-grained approach such as MP-PIC (Andrews and O'Rourke, 1996) or TFM (Lindborg et al., 2007) can evaluate the effect of numerous particle interactions concurrently without the need for parallel computing hardware. Solid stress expressions for coarse-grained approaches have been formulated for spherical particles based on the Kinetic Theory of Granular Flow (KTGF), which is based on assumptions that are valid for dilute and semi-dilute flows but applied to dense particle configurations as an approximation. In Section 5 we briefly consider the principle issues with adapting such coarse-grained models to non-spherical particles and outline potential solutions to these issues.

## 3. Particle-scale simulations: direct numerical simulations (DNS)

At the most detailed scale, one is interested in resolving the flow and transport details at the particle scale. This is often referred to as direct numerical simulation (DNS) (Deen et al.,

2012, 2014; van der Hoef et al., 2006). Typical DNS approaches use a grid for the calculation of fluid properties and for the evolution of interactions between the fluid and solid boundaries.

### 3.1. Introduction to direct numerical simulation (DNS)

To simulate mass, momentum and energy transport, there are three main approaches; namely microscopic, mesoscopic and macroscopic (or continuum). For the case of a fluid, these scales are depicted in Fig. 3. Microscopic schemes view a fluid as a set of discrete interacting particles. An example of a microscopic approach is molecular dynamics (MD) where the inter-particle forces are identified and the trajectory of the particles then calculated, similar to CFD-DEM (Section 4). MD approaches do not include a definition of fluid properties such as viscosity or temperature, and for numerical stability the time step must be less than the typical particle collision time, which for fluid particles is of the order of $10^{-14}$ s. Thus, microscopic schemes are not applicable for large scale flows (Mohamad, 2011; Krüger et al., 2017). Macroscopic or continuum approaches solve the governing differential equations by applying conservation laws of mass, momentum and energy to certain control volumes.

A number of DNS techniques are available such as the overset grid approach (Chesshire and Henshaw, 1990; Henshaw and Schwendeman, 2003; Koblitz et al., 2017), the immersed boundary method (Peskin, 1972, 1977, 2002; Zastawny et al., 2012; Mittal and Iaccarino, 2005) and the lattice Boltzmann method (LBM) (Krüger et al., 2017; Sanjeevi and Padding, 2017; Aidun and Clausen, 2010; Zarghami and Padding, 2018; Saito et al., 2017; Zarghami and Van den Akker, 2017; den Akker, 2018). In the overset grid approach, a set of structured grids representing the spatial domain and physical space overlap to provide fast moving grid generation in the case of moving geometries. For example, the overset grid approach has been extensively used to study fluid dynamics problems in aerospace (Chan, 2009). For the immersed boundary method, which was originally introduced to study flows
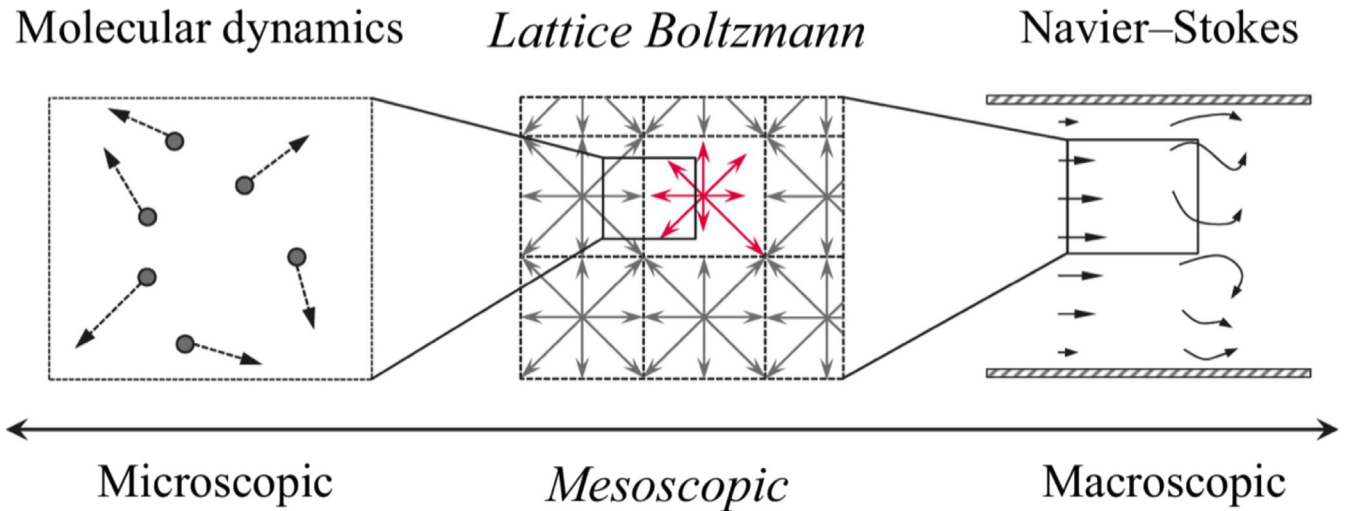
**Fig. 3.** Molecular dynamics, lattice Boltzmann and Navier-Stokes simulations of fluid flow at different scales. Image from Saito et al. (2017).

in the vicinity of heart valves (Peskin, 1972), Eulerian variables are assigned to a fixed Cartesian grid while Lagrangian variables are associated with a secondary mesh that can move relative to the Cartesian grid without constraint (Peskin, 2002).

In this paper, the focus is on the lattice Boltzmann method (LBM), which we have applied to study elongated particles in varying fluid flows (Sanjeevi and Padding, 2017; Sanjeevi et al., 2018; Zarghami and Padding, 2018). LBM is possibly the best known of so-called mesoscopic techniques, where individual detailed collisions between the fluid particles are no longer modelled explicitly. LBM has been used to simulate a range of complex fluid flows (Friedrich et al., 2001; Tatsumi and Yamamoto, 2012; Krüger et al., 2017; Aidun and Clausen, 2010; Mukherjee et al., 2018). Central to LBM is the solution of the discrete Boltzmann equation, which describes the dynamics of a fluid on a mesoscopic scale and leads to emergent Navier-Stokes fluid dynamics at the macroscale. LBM is naturally scalable to parallel computing platforms, extendable, and can easily handle complex shapes or geometries, such as elongated particles. Moreover, pressure fields and stress tensors are locally accessible (Mohamad, 2011; Krüger et al., 2017; Succi, 2001).

### 3.2. Lattice Boltzmann method

The lattice Boltzmann method (LBM) is based upon Ludwig Boltzmann's kinetic theory of gases (Mohamad, 2011; Krüger et al., 2017; Succi, 2001). Similar to other lattice models (Hardy et al., 1976; Frisch et al., 1986; Fitzgerald and Corcoran, 2005; Fitzgerald et al., 2014, 2011, 2017), the fundamental principle of LBM is that fluids (whether gas or liquid) can be imagined as a large number of discrete particles moving in space. In LBM, the velocity is discretised such that particles may only have specific velocity vectors dictated by the choice of velocity set and the underlying lattice. A discrete version of the continuous Boltzmann equation for a specific velocity vector or direction can be expressed as

$$\frac{\partial f_i}{\partial t} + \mathbf{c}_i \cdot \nabla f_i = -\frac{1}{\tau}(f_i - f_i^{eq}) \tag{1}$$

where $f_i$ is the density distribution function and $\mathbf{c}_i$ represents the discrete velocity vectors. In effect, Eq. (1) represents a set of equations, one for each of the discrete velocity directions in the velocity set and for macroscopic flow simulations, Eq. (1) replaces the Navier-Stokes equations. Using a first-order explicit Euler scheme,

a discrete version of Eq. (1) leads to the *lattice Boltzmann equation* (LBE), which is the combination of a collision operation

$$\tilde{f}_i(\mathbf{x}, t + \Delta t) = f_i(\mathbf{x}, t) - \frac{\Delta t}{\tau}(f_i(\mathbf{x}, t) - f_i^{eq}(\mathbf{x}, t)) \tag{2}$$

and a streaming operation

$$f_i(\mathbf{x} + \mathbf{c}_i \Delta t, t + \Delta t) = \tilde{f}_i(\mathbf{x}, t + \Delta t) \tag{3}$$

where $\Delta t$ is the time step, $\tilde{f}$ represents the post-collision state, and $f^{eq}$ is the equilibrium density distribution function. Further details on the velocity vector sets and $f^{eq}$ are available in the literature (Krüger et al., 2017; Sanjeevi and Padding, 2017; Sanjeevi et al., 2018). LBM simulations are performed on a structured Cartesian grid with a lattice spacing $\Delta x$ where it is convenient to set $\Delta t = \Delta x = 1$. The LBE and Navier-Stokes equations can be linked via Chapman-Enskog analysis (Krüger et al., 2017). Using this approach, the kinematic shear viscosity can be estimated from the relaxation time $\tau$ using $v = c_s^2(\tau - \frac{\Delta t}{2})$ where $c_s = 1/\sqrt{3}$ is the speed of sound for LBM in 3D.

Eq. (3) is the general lattice equation with a single relaxation-time (SRT). Flows can also be simulated with a multi-relaxation time (MRT) approach whereby a suitable transformation matrix is used to transform the particle distribution function from velocity space to moment space (Sanjeevi et al., 2018; d'Humiéres et al., 2002). In comparison to the SRT approach, the MRT approach provides greater stability in the solution as it allows for the inclusion of relaxation times for relevant physical processes (Rui and Bao-chang, 2010; Yoshida and Nagaoka, 2010; d'Humiéres et al., 2002).

There are notable differences between LBM and the macroscopic methods based on the Navier-Stokes (NS) equation. Firstly, the governing equation of LBM is first-order, while the NS equation is a second-order partial differential equation. Secondly, LBM includes a simple advection term that allows for uniform field streaming as opposed to a nonlinear convective term inherent in NS methods. Thirdly, owing to the kinetic nature of LBM, the pressure and stress tensor fields are locally available. Hence, there is no need to solve a Pressure Poisson equation; rather the pressure is extracted from the equation of state. Fourthly, spatial discretisation in LBM is coupled to the discretisation of the velocity space and leads to regular square grids. This is a general limitation of the lattice Boltzmann approach. Finally, the kinetic nature of LBM eases the incorporation of molecular level interactions in comparison to NS-based methods.

The lattice Boltzmann method is a quasi-compressible method that solves the compressible Navier-Stokes equation in the incompressible limit. Thus, when simulating incompressible flow, the macroscopic equations recovered from LBM differ from the incompressible Navier-Stokes equations by terms of spatial derivatives of the fluid density, otherwise known as compressibility error (Succi, 2001; Lin et al., 1996). Accurate simulations of incompressible flows require that the density variation ($\delta\rho$) and the Mach number (Ma) are negligibly small, i.e. $\delta\rho/\rho \to 0$ and Ma $\to 0$. In effect, for an incompressible flow studied with LBM, the density, and hence the mass, is effectively constant. Any deviation from these requirements amplify the compressibility error and as a result significantly impact the numerical accuracy. It has been demonstrated that for finite Ma numbers, the compressibility error of LBM scales as O(Ma$^2$) (Dellar, 2003).

### 3.3. Boundary conditions and mass leakage

As LBM is based on a regular Cartesian grid, the method can be classified as a non-boundary-fitted scheme for the simulation of fluid flows with curved boundaries, including fluid flow around non-spherical particles. Implementation of boundary conditions can be achieved by changing the particle distribution function of any grid location deemed to be part of or near a solid boundary or solid particle. One of the major difficulties of implementing boundary conditions in LBM is the determination of accurate distribution functions for boundary interactions (Sanjeevi et al., 2018; Zarghami and Padding, 2018).

The most commonly used boundary condition used in LBM simulations is the bounce-back (BB) scheme. In the BB scheme, when a particle distribution streams to a wall node, it reflects back to the fluid node along its respective incoming link (Succi, 2001). Examples of implementations of the bounce-back scheme are on-site BB and halfway BB (Ziegler, 1993). In the on-site BB scheme, the physical boundary nodes lie exactly on the lattice nodes. However, in the mid-grid BB scheme, the solid boundary is located exactly mid-plane between the boundary fluid node and the off-lattice node located inside the solid. The on-site BB scheme is first-order accurate whereas the mid-grid BB scheme provides second-order accuracy in both space and time (Succi, 2001; Ginzbourg and d'Humières, 1996; Luo, 1997).

A major drawback of on-site and mid-grid BB schemes is their failure to accurately account for curved boundaries (Sanjeevi et al., 2018) as these schemes approximate curved boundaries as discrete staircase shaped boundaries (Ladd, 1994; Ladd and Verberg, 2001), leading to a loss of resolution and a non-zero wall velocity (Kandhai et al., 1999). The effects of this approximation are greater at high Reynolds number where the fluid boundary layers are thinner. A number of boundary treatments using inter/extrapolation techniques are available to model curved boundaries without the staircase representation (Mei et al., 1999; Bouzidi et al., 2001; Yu et al., 2003; Bao et al., 2008; Feng and Michaelides, 2004; Krüger et al., 2017). One such approach is the interpolated bounce-back (IBB) approach of Bouzidi et al. (Bouzidi et al., 2001; Krüger et al., 2017). Fig. 4 shows a schematic of a curved-wall boundary intersecting a fluid node $\mathbf{x}_f$ and a boundary node $\mathbf{x}_b$ at the point $\mathbf{x}_w$ where $q = |\mathbf{x}_w - \mathbf{x}_f|/|\mathbf{x}_b - \mathbf{x}_f|$, which is the fraction of the intersected lattice link in the fluid domain. In the Bouzidi scheme (Bouzidi et al., 2001; Sanjeevi et al., 2018), a linear interpolation of the distribution functions is given as

$$\tilde{f}_{\bar{i}}(\mathbf{x}_f, t + \Delta t) = \begin{cases} 2q\tilde{f}_i(\mathbf{x}_f, t) + (1-2q)\tilde{f}_i(\mathbf{x}_{ff}, t) & q \leq 1/2, \\ \frac{1}{2q}\tilde{f}_i(\mathbf{x}_f, t) + \frac{2q-1}{2q}\tilde{f}_{\bar{i}}(\mathbf{x}_f, t) & q \geqslant 1/2, \end{cases} \quad (4)$$

where $\bar{i}$ denotes the opposite direction to $i$. The mid-grid bounce-back scheme can be recovered when $q = 1/2$. A quadratic interpolation approach is also available, which is also second-order accurate (Zarghami and Padding, 2018; Bouzidi et al., 2001; Krüger et al., 2017). The use of the quadratic interpolation approach requires an additional fluid node ($\mathbf{x}_{fff}$ in Fig. 4). A disadvantage of all interpolation schemes is mass leakage, which refers to both mass loss and gain over time (Yin et al., 2012; Krüger et al., 2017; Sanjeevi et al., 2018). Issues with mass leakage are specifically prevalent for systems operating at high Reynolds number with periodic boundaries, such as for studies on flows experienced by Geldart D type particles (Sanjeevi et al., 2018). When inflow-outflow boundary conditions are used, mass leakage is not a real concern since the flow is continuously replenished. However for other boundary conditions, if the mass leakage is not monitored, there can be significant departure from constant density over time.To alleviate any mass leakage effects induced by the bounce-back scheme, mass conservation can be enforced by monitoring system mass, and adding or removing mass from the system (Sanjeevi et al., 2018).

An alternative approach to the BB schemes can also be considered for LBM studies. For instance, the immersed boundary (IB) method (Peskin, 1977, 2002) can be combined with the LBM approach and is referred to as the immersed boundary lattice Boltzmann method (IB-LBM) (Li et al., 2016; Mountrakis et al., 2017). Similar to LBM, the IB method represents the fluid on a discrete grid or mesh. In addition, solid elements such as particles or boundaries are also represented on a second grid that does not need to align with the fluid grid. Central to the IB method is the inclusion of a non-slip boundary condition between the fluid and the solid structure. To achieve this, grid points associated with a solid are affixed to the fluid, with the fluid velocity then interpo-
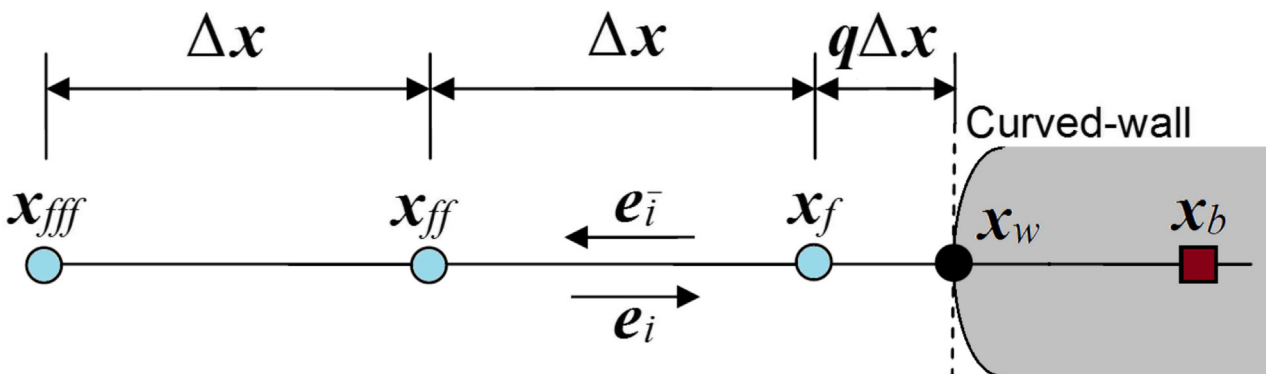


**Fig. 4.** One-dimensional regular lattice and curved-wall boundary. $\mathbf{x}_f$, $\mathbf{x}_{ff}$ and $\mathbf{x}_{fff}$ are all fluid nodes and $\mathbf{x}_b$ is a node located within the curved-wall boundary. $\mathbf{x}_w$ is the point of intersection between the curved-wall and the link between $\mathbf{x}_b$ and $\mathbf{x}_f$. Here $|\mathbf{x}_b - \mathbf{x}_f| = \Delta x$.

lated at the Lagrangian points and the resulting forces distributed over the Eulerian fluid points subject to a coupling function **f**, with this function then used to calculate a forcing term in the LBM approach (Li et al., 2016; Mountrakis et al., 2017). Both velocity interpolation and force distribution at the solid surface are controlled by kernel functions.

### 3.4. Hydrodynamic forces on elongated particles

In this section recent applications of LBM for the study of elongated particles in fluid flows are summarised. Our primary interest is studies related to hydrodynamic forces. Nonetheless, pertinent studies related to LBM studies on heat transfer in systems of non-spherical particles are also highlighted. In a fluidised bed reactor, particles experience variable hydrodynamic conditions depending on local particle density, Reynolds number, orientation, and proximity to boundaries. Here, the Reynolds number for a particle is denoted as $Re = \rho_f d_p |\mathbf{v}_f - \mathbf{v}_i| / \mu_f$ with $d_p$ (volume-equivalent sphere) particle diameter, $|\mathbf{v}_f - \mathbf{v}_i|$ the local relative velocity between the fluid and particle, $\rho_f$ the fluid density, and $\mu_f$ the fluid viscosity. In the first part of this section the focus is on the use of the LBM approach to estimate hydrodynamic correlations and coefficients for isolated and arrested elongated particles, while in the second part we compare these correlations with the state-of-the-art. It should be noted that the approximation of arrested particles for the determination of hydrodynamic forces is only well suited for particles with large Stokes number, i.e. where the particle response time to flow changes is much greater than the response time of the fluid (Rubinstein et al., 2016, 2017). Finally, we consider the influence of nearby boundaries on the hydrodynamic forces of elongated particles.

#### 3.4.1. Hydrodynamic force and torque coefficient correlations

DNS approaches have been applied to derive correlations for the hydrodynamic force coefficients associated with the differing hydrodynamic forces experienced by non-spherical particles in fluid flows (Zastawny et al., 2012; Ouchene et al., 2016; Sanjeevi and Padding, 2017; Sanjeevi et al., 2018). While spherical particles are primarily subject to hydrodynamic drag and experience negligible lift force or torque in fluidised beds, non-spherical particles are subject to drag, lift, and torque, which all need to be included appropriately in larger scale numerical simulations. For an isolated particle moving with a velocity $\mathbf{v}_i$ in a fluid flow with an undisturbed velocity $\mathbf{v}_f$, the drag force is given by

$$F_{D0} = \frac{1}{2} C_D \rho_f (\mathbf{v}_f - \mathbf{v}_i)^2 \frac{\pi}{4} d_p^2 \tag{5}$$

where $C_D$ is the drag force coefficient and $d_p$ is the diameter of a sphere with the same volume as the non-spherical particle. Note that here we have chosen the reference area for the particle equal to $\frac{\pi}{4} d_p^2$, which is the cross-sectional area of the volume equivalent sphere. We purposefully choose this reference area to be invariant to changes in the orientation of the particle to make the dependence of the drag force on the particle orientation fully explicit in the drag force coefficient $C_D$. In the case of spherical particles, a number of widely employed expressions for the drag force for differing flow conditions are available in the literature (Ergun, 1952; Wen and Yu, 1966; Hill et al., 2001; Beetstra et al., 2007).

When a non-spherical particle is not aligned with one of its symmetry axes with respect to the fluid velocity, a shape-induced lift force results that can significantly affect the trajectory of a particle. In this situation, the fluid flow near the upper and lower sides of the particle differ. The pressure drops in regions of rapid flow while the pressure increases in regions where the fluid velocity decreases. This leads to an asymmetric pressure distribution and

induces a lift force that is perpendicular to the direction of the relative fluid flow. An example of the lift force $\mathbf{F}_L$ due to a fluid flow acting on a spherocylinder that is not aligned with the direction of the flow is depicted in Fig. 5(a). $\mathbf{F}_L$ is orthogonal to the relative velocity of the fluid with respect to the particle $\mathbf{v}'_{fi}$. Due to symmetry, $\mathbf{F}_L$ lies in the plane defined by the orientation vector **u** and $\mathbf{v}'_{fi}$. We do note that at higher Reynolds numbers turbulent vortex shedding can lead to time-varying lift components perpendicular to this plane, but such lift forces are usually at least an order of magnitude weaker than the lift force discussed here, certainly in a time-averaged sense. The magnitude of the lift force for an isolated particle is given by

$$F_{L0} = \frac{1}{2} C_L \rho_f (\mathbf{v}_f - \mathbf{v}_i)^2 \frac{\pi}{4} d_p^2 \tag{6}$$

where $C_L$ is the lift force coefficient. The resultant lift force is $\mathbf{F}_L = F_L \hat{\mathbf{e}}_{L_0}$, where $\hat{\mathbf{e}}_{L_0}$ is the lift force orientation vector given by (Mema et al., 2017, 2019)

$$\hat{\mathbf{e}}_{L_0} = \frac{\mathbf{u}_i \cdot \mathbf{v}'_{fi}}{\left| \mathbf{u}_i \cdot \mathbf{v}'_{fi} \right|} \frac{\left( \mathbf{u}_i \times \mathbf{v}'_{fi} \right) \times \mathbf{v}'_{fi}}{\left\| \left( \mathbf{u}_i \times \mathbf{v}'_{fi} \right) \times \mathbf{v}'_{fi} \right\|} . \tag{7}$$

When the centre of pressure $\mathbf{x}_{cp}$ does not coincide with the centre of mass of the particle $\mathbf{x}_{cm}$, a pitching torque results that acts around the axis perpendicular to the plane of relative fluid velocity $\mathbf{v}'_{fi}$ and particle orientation vector $\mathbf{u}_i$, and as a result, can lead to changes in the angle of incidence $\phi$ of the particle, which is defined as the angle between $\mathbf{u}_i$ and $\mathbf{v}'_{fi}$. The pitching torque acting on a spherocylindrical particle is shown in Fig. 5(b). The magnitude of the pitching torque on an isolated particle is given by

$$T_0 = \frac{1}{2} C_T \rho_f (\mathbf{v}_f - \mathbf{v}_i)^2 \frac{\pi}{8} d_p^3 \tag{8}$$

where $C_T$ is the pitching torque coefficient. The hydrodynamic torque is perpendicular to the plane of the particle relative velocity and particle orientation vector such that the torque orientation vector $\hat{\mathbf{e}}_{T_0}$ is given by

$$\hat{\mathbf{e}}_{T_0} = \frac{\mathbf{v}'_{fi} \cdot \mathbf{u}_i}{\left| \mathbf{v}'_{fi} \cdot \mathbf{u}_i \right|} \frac{\mathbf{v}'_{fi} \times \mathbf{u}_i}{\left| \mathbf{v}'_{fi} \times \mathbf{u}_i \right|} . \tag{9}$$

The resultant torque is expressed as $\mathbf{T}_p = T_0 \hat{\mathbf{e}}_{T_0}$. A particle may also be subject to hydrodynamic rotational torque that acts around the axis of symmetry of the particle. However, in this paper, rotational torque is not considered. Further information on rotational torque and the calculation of a rotational torque correlation function for elongated particles is available in the immersed boundary method study of Zastawny et al. (2012).

For accurate Euler-Lagrangian simulation of elongated particle dynamics in fluidised beds or other processing equipment, dedicated correlations for the coefficients in Eqs. (5), (6) and (8) are essential. Furthermore, the correlations need to be applicable to the high $Re$ regime given that larger elongated particles can experience $Re \geqslant 2000$ (Sanjeevi et al., 2018).

Using LBM with a multi-relaxation time scheme, we have derived drag, lift and torque functions for ellipsoids and spherocylinders subject to varying flow conditions (Sanjeevi and Padding, 2017; Sanjeevi et al., 2018). In an initial study on force correlations for prolate spheroids, we established that the mean drag coefficient for different incidence angles follows a $\sin^2 \phi$ scaling between the extremes at 0 and 90 degrees. Motivated by this initial evaluation of the drag on spheroids, we extended the MRT-LBM approach to study the drag, lift and torque experienced by elongated particles of aspect ratio 5/2 and 4 when subject to a fluid flow of uniform velocity in an inflow-outflow geometry with
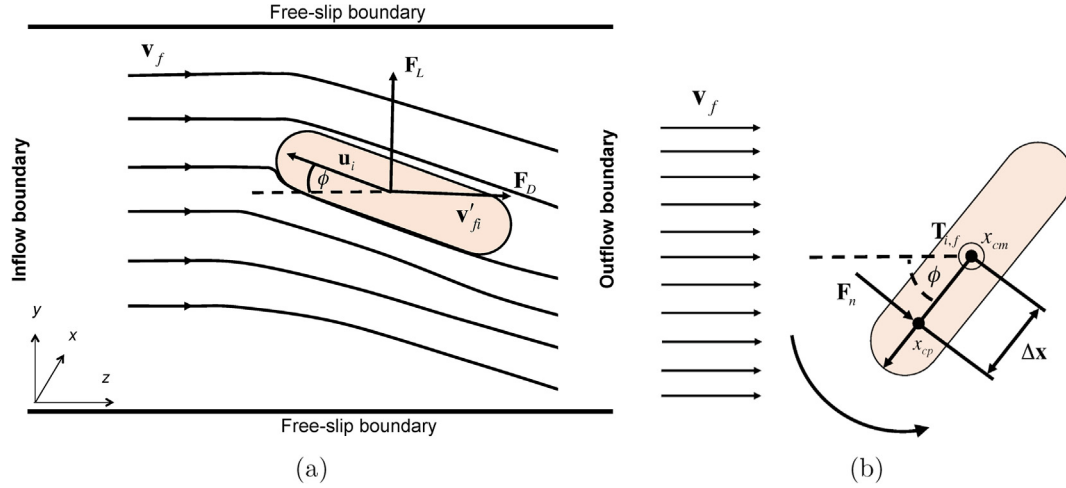
**Fig. 5.** (a) Illustration of drag and lift force acting on an inclined spherocylindrical particle in a fluid flow. The relative velocity of the fluid with respect to the particle is $\mathbf{v}'_{fi}$, $\mathbf{u}_i$ denotes the particle orientation vector, and $\phi$ is the angle of incidence of the fluid flow. This is the domain used in our MRT-LBM simulations (Sanjeevi et al., 2018). The undisturbed fluid enters the domain from the left with a velocity $\mathbf{v}_f$ while the side walls are represented as free-slip boundaries. (b) Illustration of pitching torque acting on a spherocylindrical particle. The difference between the centre of pressure $\mathbf{x}_{cp}$ and the centre of mass $\mathbf{x}_{cm}$ leads to a hydrodynamic torque $\mathbf{T}_{i,f}$ acting on the particle. $\Delta\mathbf{x}$ is the distance between $\mathbf{x}_{cp}$ and $\mathbf{x}_{cm}$.

free-slip boundaries (Sanjeevi et al., 2018). The particle Reynolds number was varied in the range $0.1 \leqslant Re \leqslant 2000$ while the incident angle was in the range $0° \leqslant \phi \leqslant 90°$. Arrested particle arrangements are used for all LBM simulations given that particle mobility can have significant effects on the hydrodynamic forces experienced by a particle. A previous DNS study on spherical particles has shown that particle mobility also influences the drag force (Tang et al., 2016). In the case of elongated particles, this effect would likely be greater as in dense configurations, such as those expected in fluidised bed reactors, elongated particles display mutual alignment when subject to sufficient deformation (Guo et al., 2012). The influence of the mobility of elongated particles on the ensuing hydrodynamic forces could be investigated in a future study.

The drag coefficient $C_D$ at varying incident angle $\phi$ and $Re$ for a prolate spheroid, an oblate spheroid and a spherocylinder interpolates as a sine-squared function between the limits at $\phi = 0°, 90°$ of the form

$$C_{D,\phi} = C_{D,\phi=0°} + \left(C_{D,\phi=90°} - C_{D,\phi=0°}\right)\sin^2\phi \tag{10}$$

where $C_{D,\phi=0°}$ and $C_{D,\phi=90°}$ are calculated from

$$C_{D,\phi=0°,90°} = \left(\frac{a_1}{Re} + \frac{a_2}{Re^{a_3}}\right)e^{-a_4 Re} + a_5\left(1 - e^{-a_4 Re}\right) \tag{11}$$

where the fitting coefficients $a_1$ to $a_5$ for the different particles can be found in the paper of Sanjeevi et al. (2018). An example of the variation of $C_D$ with $\phi$ for the three different spheroids for $Re = 100$ is shown in Fig. 6(a) where excellent correspondence is observed in all cases.

The variation of the lift coefficient $C_L$ with the incident angle $\phi$ and $Re$ for a prolate spheroid, an oblate spheroid and a spherocylinder $Re = 1,100$ is given by the correlation function

$$C_{L,\phi} = \left(\frac{b_1}{Re} + \frac{b_2}{Re^{b_3}} + \frac{b_4}{Re^{b_5}}\right)\sin\phi^{1+b_6 Re^{b_7}}\cos\phi^{1+b_8 Re^{b_9}} \tag{12}$$

with the fitting coefficients $b_1$ to $b_9$ available in the literature (Sanjeevi et al., 2018). This correlation function provides a good fit to the simulation data for all particle shapes and Reynolds number (Sanjeevi et al., 2018) with an example of the fit for $Re = 100$ provided in Fig. 6(b). The lift correlation function is dependent on powers of the sine and cosine of the incident angle, where the expo-

nents tend to 1 as $Re \to 0$, as anticipated for the Stokes flow regime. In the unsteady regime, the distribution has an inherent skewness for all particle types (Sanjeevi et al., 2018).

Finally, the variation of the pitching torque coefficient $C_T$ with the incident angle $\phi$ for a prolate spheroid, an oblate spheroid and a spherocylinder can be described by the expression

$$C_{T,\phi} = \left(\frac{c_1}{Re^{c_2}} + \frac{c_3}{Re^{c_4}}\right)\sin\phi^{1+c_5 Re^{c_6}}\cos\phi^{1+c_7 Re^{c_8}} \tag{13}$$

where the coefficients $c_1$ to $c_8$ can be found in Sanjeevi et al. (2018). As for the lift correlation function, the torque correlation function depends on the sine and cosine of the incident angle each with an associated exponent. In the Stokes regime, pitching torque is negligible and therefore can be excluded from the fit. An example of the fit applied to simulation data at $Re = 100$ is shown in Fig. 6(c). For all values of $Re$, the mean relative deviation of the correlation function from the data for the spherocylinder is just 4.12% (Sanjeevi et al., 2018).

### 3.4.2. Comparison with other coefficient correlations

Using a substantial set of experimental data and results from simulations, Hölzer and Sommerfeld (2008) formulated a drag correlation function that is applicable to arbitrary-shaped particles of the form

$$C_D = \frac{8}{Re}\frac{1}{\sqrt{\Phi_\parallel}} + \frac{16}{Re}\frac{1}{\sqrt{\Phi}} + \frac{3}{\sqrt{Re}}\frac{1}{\Phi^{3/4}} + 0.42 \times 10^{0.4(-\log\Phi)^{0.2}}\frac{1}{\Phi_\perp} \tag{14}$$

where $\Phi$ is the particle sphericity defined as the ratio between the surface area of the volume equivalent sphere and the particle of interest, $\Phi_\parallel$ is the lengthwise sphericity defined as the ratio between the cross-sectional area of the volume equivalent sphere and the difference between half the surface area and the projected cross-sectional area parallel to the direction of relative flow of the particle of interest, and $\Phi_\perp$ is the crosswise sphericity, which is the ratio between the cross-sectional area of the volume equivalent sphere and the projected cross-sectional area perpendicular to the flow for the particle of interest (Hölzer and Sommerfeld, 2008). Eq. (14) is in part based upon an expression proposed by Leith (1987) for non-spherical particles in the Stokes regime, which does not account for the orientation dependence on $C_D$ and does not
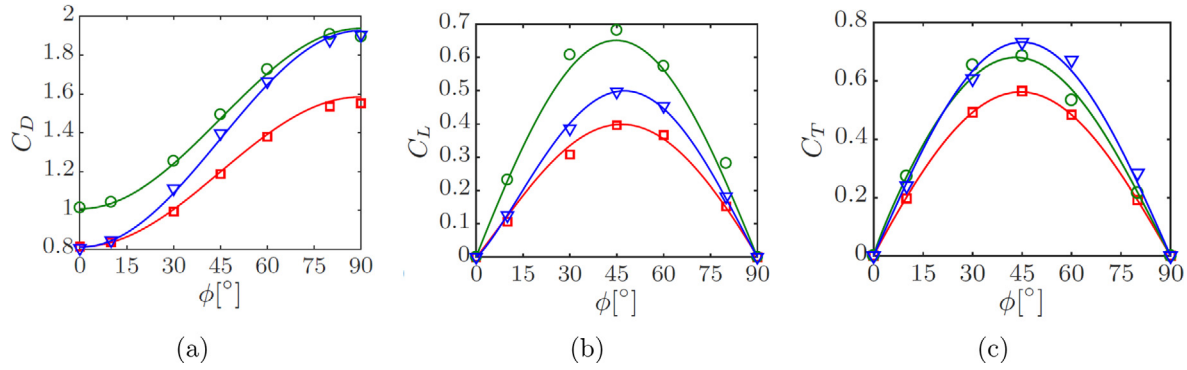
**Fig. 6.** Variation of hydrodynamic force coefficients at $Re = 100$ with $\phi$ for a prolate spheroid (red squares), oblate spheroid (green discs) and a spherocylinder (blue triangles). (a) $C_D$ (Drag) with fits given by Eq. (10); (b) $C_L$ (Lift) with fits given by Eq. (12); (c) $C_T$ (Torque) with fits given by Eq. (13). Images from Sanjeevi et al. (2018). (For interpretation of the references to colour in this figure legend, the reader is referred to the web version of this article.)

depend on $\Phi_{\parallel}$. Given that $\Phi_{\parallel}$ is more difficult to calculate in comparison to $\Phi_{\perp}$, $\Phi_{\parallel}$ can be been replaced by $\Phi_{\perp}$ in Eq. (14). This expression is easy to implement and applicable to many different particle shapes. In addition, the mean relative deviation of the expression from experimental data is 14.1% with $\Phi_{\parallel}$ and 14.4% with $\Phi_{\perp}$, which is significantly lower than previous expressions (Haider and Levenspiel, 1989; Ganser, 1993).

Hölzer and Sommerfeld (2008) only proposed a correlation function for the drag coefficient experienced by non-spherical particles. A DNS study using the immersed boundary method by Zastawny et al. (2012) proposed correlations for drag, lift, pitching torque, and rotational torque for spheroids, discs and spherocylinders. The aspect ratio of the particles was varied from 1.25 to 5 and $Re \leqslant 300$. For the drag coefficient, the correlation function has the form

$$C_{D,\phi} = C_{D,\phi=0°} + \left(C_{D,\phi=90°} - C_{D,\phi=0°}\right)\sin^{a_0}\phi \tag{15}$$

where $C_{D,\phi=0°} = a_1/Re^{a_2} + a_3/Re^{a_4}$ and $C_{D,\phi=90°} = a_5/Re^{a_6} + a_7/Re^{a_8}$. Eq. (15) is similar to the expression for Stokes flow (Happel and Brenn, 1983) and the expression from our LBM studies (Sanjeevi and Padding, 2017; Sanjeevi et al., 2018), where the central difference is the exponent $a_0$ that is dependent on particle shape. The other parameters in $C_{D,\phi=0°}$ and $C_{D,\phi=90°}$ are also specific to the particle size and shape. In the case of lift, the correlation function is expressed as

$$C_{L,\phi} = \left(\frac{b_1}{Re^{b_2}} + \frac{b_3}{Re^{b_4}}\right)\sin\phi^{b_5+b_6Re^{b_7}}\cos\phi^{b_8+b_9Re^{b_{10}}} \tag{16}$$

where the $b_k$ parameters are dependent on particle shape. Eq. (16) is comparable to the lift correlation function from our LBM study (Sanjeevi et al., 2018). One characteristic difference is that Eq. (12) explicitly captures the physical limit for Stokes flow (Happel and Brenn, 1983) where the exponents for the sine and cosine terms both tend to the expected value of 1 for low $Re$. Finally, the correlation function for pitching torque has a form similar to the function for lift (Eq. (16)) and is given by

$$C_L = \left(\frac{c_1}{Re^{c_2}} + \frac{c_3}{Re^{c_4}}\right)\sin\phi^{c_5+c_6Re^{c_7}}\cos\phi^{c_8+c_9Re^{c_{10}}} \tag{17}$$

where the $c_k$ parameters are dependent on particle shape. Zastawny et al. (2012) also provide a correlation function for the rotational torque ($C_R$) that is dependent on the rotational Reynolds number $Re_R$.

Using the commercial Finite Volume solver ANSYS FLUENT, Richter and Nikrityuk calculated drag, lift, and torque correlations for spherical, ellipsoidal, and cubic particles (Richter and Nikrityuk, 2013). We focus on the expressions for the ellipsoidal particle in

their study, which had an aspect ratio of 2. The correlation functions defined by Richter and Nikrityuk depend on a transformed angle of incidence defined as

$$\tilde{\phi} = |((\phi + 90)\text{mod}180) - 180|, \tag{18}$$

which basically means that the roles of parallel ($\phi = 0$, $\tilde{\phi} = 90$) and perpendicular ($\phi = 90$, $\tilde{\phi} = 0$) are reversed. For an ellipsoid, the drag, lift and torque correlations as a function of $\tilde{\phi}$ and calculated from fits to DNS simulation data are

$$C_D = 0.0316 + \frac{18.9}{Re} + \frac{6.25}{\sqrt{Re}} + \frac{2.21}{Re^{0.303}}\sin^2\tilde{\phi}, \tag{19}$$

$$C_L = \frac{0.97}{Re^{0.25}}\sin 2\tilde{\phi} - \frac{0.0262}{Re^{0.25}}\cos 2\tilde{\phi}, \tag{20}$$

$$C_T = -\left(\frac{0.408}{Re} + \frac{0.369}{Re^{0.126}}\right)\sin 2\tilde{\phi}. \tag{21}$$

The correlations by Richter and Nikrityuk were estimated for flows with Reynolds numbers between 10 and 200 and they also provided correlations for heat transfer studies. It is also worth highlighting the DNS study where an Immersed Boundary-lattice Boltzman method (IB-LBM) was applied to find the following drag correlation function for heated ellipsoidal particles with varying aspect ratio $w$ and incident angle, and for $10 \leqslant Re \leqslant 200$ (Ke et al., 2018)

$$C_D = \frac{a_1}{Re}w^{a_2} + \frac{a_3}{\sqrt{Re}}w^{a_4} + a_5w^{a_6} + w^{a_7}(w-1)\frac{a_8}{Re^{a_9}}\sin^2(a_{10}\phi). \tag{22}$$

The fitting parameters in Eq. (22) are provided in the literature (Ke et al., 2018).

In a subsequent DNS study with ANSYS FLUENT, Ouchene et al. (2016) derived and validated correlations for non-spherical particles, specifically prolate spheroids, with aspect ratios ranging from 1 to 32, subject to a uniform flow with $Re$ between 1.21 and 240. The correlation functions in all cases are dependent on $Re$, the aspect ratio, and the incident angle. The drag correlation proposed by Ouchene et al. is inspired by the expression for Stokes flow (Happel and Brenn, 1983) and equivalent to that proposed by Sanjeevi and Padding (2017) and Sanjeevi et al. (2018). However, the expressions for $C_{D,\phi=0°}$ and $C_{D,\phi=90°}$ from Ouchene et al. differ from Sanjeevi et al. in that they account for varying aspect ratio. Full details on $C_{D,\phi=0°}$ and $C_{D,\phi=90°}$ can be found in the literature (Ouchene et al., 2016; Arcen et al., 2017). In the case of lift, the correlation function takes the form

$$C_L = \left(F_L(w)Re^{0.25} + \frac{G_L(w)}{Re^{0.755}}\right)\cos\phi\sin^{1.002Re}\phi. \tag{23}$$

For brevity we do not include the full expressions for $F_L(w)$ and $G_L(w)$, which can be found in the relevant literature (Ouchene et al., 2016; Arcen et al., 2017). Finally, Ouchene et al. also defined a correlation function for the pitching torque. The authors identified separate pitching torque correlations for small aspect ratio ($w \leqslant 10$) and large aspect ratio ($10 \leqslant w \leqslant 32$) particles of the form

$$C_T = \left( \frac{F_T(w)}{Re^{c_1}} + \frac{G_T(w)}{Re^{c_2}} \right) \cos^{c_3^{Re}} \sin \phi \qquad (24)$$

where $c_k$ are fitting parameters related to the small and large aspect ratios, and $F_T(w)$ and $G_T(w)$ are fitting functions. For both small and large aspect ratios $c_3 \approx 1$. Values of all fitting parameters and additional function expressions are provided in the study of Ouchene et al. (Ouchene et al., 2016). These correlations have been applied to study the dynamics of ellipsoidal particles in vertical turbulent flow channels (Arcen et al., 2017). The correlation functions specified from Eqs. (14)–(24) are limited to steady flows. As outlined, the correlations of Zastawny et al. (2012) and Ouchene et al. (2016) have been derived for flows with $Re \leqslant 300$, whereas the correlations of our LBM study are applicable to steady and unsteady flows with $Re \leqslant 2000$.

Fig. 7 shows a comparison of $C_D$ at $Re = 100$ and $Re = 2000$ for a prolate spheroid of aspect ratio $w = 5/2$ and a spherocylinder of aspect ratio $w = 4$ as calculated with the correlation functions of Hölzer and Sommerfeld (2008), Zastawny et al. (2012), Ouchene et al. (2016), and the simulation data and correlations from our LBM study (Sanjeevi et al., 2018). For both particle shapes there is good agreement between our correlation and the correlation of Hölzer and Sommerfeld (2008) at $Re = 100$. Differences in the correlation at $Re = 2000$ arise as the Hölzer and Sommerfeld correlation is applicable to arbitrary shaped particles and a wide range of $Re$, while our correlation applies specifically to elongated particles such as ellipsoids and spherocylinders. For the prolate spheroid, there is good agreement between our correlation and that of Zastawny et al. (2012). In addition, the correlation function of Ouchene et al. (2016) does not match the trend at either Reynolds number with the difference most pronounced at large $\phi$.

Fig. 8 shows a comparison of $C_L$ at $Re = 100$ and $Re = 2000$ for a prolate spheroid with $w = 5/2$ as calculated with the correlation functions of Zastawny et al. (2012) and Ouchene et al. (2016), and the simulation data and correlations from our LBM study (Sanjeevi et al., 2018). Our correlation function is shown to be in good agreement with the correlation function of Zastawny et al. at $Re = 100$, while the expression of Ouchene et al. appears to underestimate $C_L$ at all incident angles with a maximum deviation of 40% observed at $\phi \approx 45°$. At $Re = 2000$, the correlation function of Zastawny et al. does not have the same agreement with the LBM simulation data and our correlation function as observed at $Re = 100$. Considering that the correlation function of Zastawny et al. (Eq. (16)) was derived for flows up to $Re = 300$, the degree of correspondence is reasonable.

Correlation functions for $C_T$ from LBM simulations and other DNS studies for a prolate spheroid with $w = 5/2$ are plotted in Fig. 9. At $Re = 100$, there is good correspondence between the correlations of Zastawny et al. and Ouchene et al. while our correlation function and LBM data estimates a larger $C_T$ at all incident angles. The difference between our correlation and the correlation of Zastawny et al. may be attributed to the powers associated with the sine and cosine terms of the correlation function. In both cases, the sine-cosine expression is inspired by the $C_L$ expression from Stokes flow (Happel and Brenn, 1983). We predict a function skewed to the left while the correlation functions of Zastawny et al. and Ouchene et al. are both skewed to the right, a difference that emerges since the correlation functions of Zastawny et al. and Ouchene et al. have been derived for flows with $Re \leqslant 300$ while our correlation function applies up to $Re = 2000$ and to even larger values of the Reynolds number.

In summary, significant work has already been done to find correlation functions for drag, lift and torque on a single isolated particle subject to idealised channel-like flow conditions. However, in a fluidised bed reactor, the flow field experienced by a specific particle will also depend on the presence of neighbouring particles. Therefore, multiparticle effects on the drag, lift, torque, and their associated correlation functions must also be taken into consideration. A recent DNS study by He and Tafti using the immersed boundary method (IBM) simulated random monodisperse suspensions of ellipsoidal particles in systems with a solid fraction ranging from 0.1 to 0.35 (191 to 669 particles) and at Reynolds
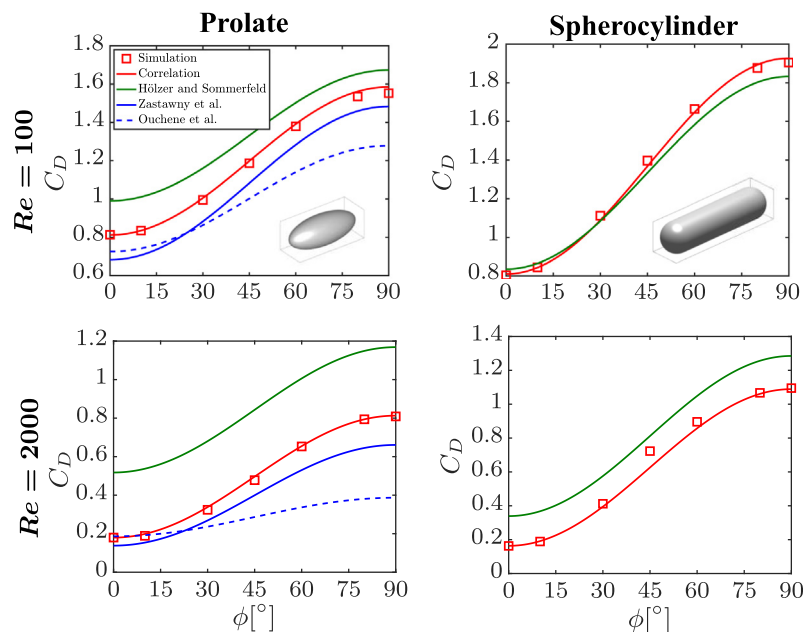


**Fig. 7.** Comparison of $C_D$ using various correlation functions for varying particle shape, incident angle $\phi$, and $Re$. In the case of the prolate spheroid, $C_D$ is plotted using the drag correlation functions of Hölzer and Sommerfeld (2008), Zastawny et al. (2012), Ouchene et al. (2016), and Sanjeevi et al. (2018). In addition the LBM simulation data from Sanjeevi et al. is also presented. Images based on those in Sanjeevi et al. (2018).

**Fig. 8.** Comparison of $C_L$ using various correlation functions for a prolate spheroid for varying incident angle and $Re$. Images based on those in Sanjeevi et al. (2018).



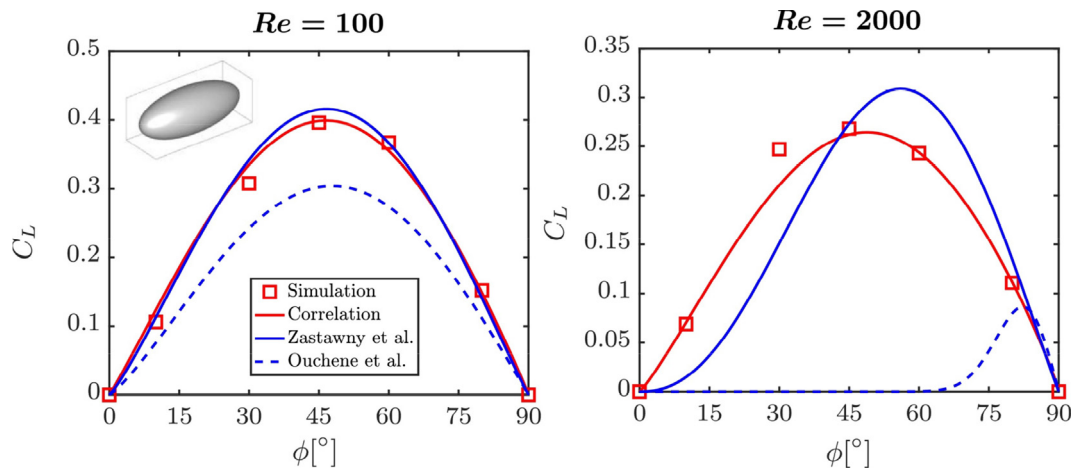**Fig. 9.** Comparison of $C_T$ using various correlation functions for a prolate spheroid for varying incident angle and $Re$. Images based on those in Sanjeevi et al. (2018).

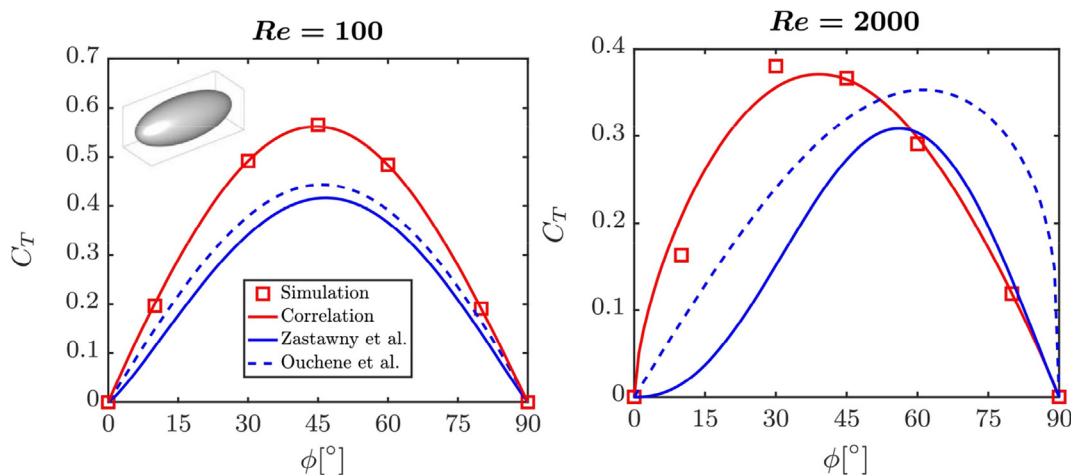numbers in the range $10 < Re < 200$ (He and Tafti, 2018). The study revealed that the variation in the mean drag, lift, and torque experienced by a particle for differing incident angles is similar to the case of an isolated particle although the authors do not present correlation expressions accounting for the effects of local solid fraction. In addition, the magnitude of the variations in the drag, lift, and torque are much larger for particle suspensions than for isolated particles. The authors also investigated the relevance of secondary forces induced by the presence of other particles in close proximity. The study of He and Tafti highlights the importance of accounting for multi-particle effects, and motivates further investigations for the derivation of multi-particle drag, lift, and torque correlations.

It is pertinent to briefly consider recent LBM studies that have focused on the hydrodynamic forces experienced by other non-spherical particles. Guan et al. (2017) used the LBM approach to study only the drag force acting on cylindrical, square, and spherical particles in a channel flow for Reynolds numbers between 0.1 and 3000, which exceeds the maximum $Re$ of our LBM studies. An important finding from their study is that the variation of the $C_D$ trend with Reynolds numbers is different for each particle shape. However, the accuracy of their results is poor at the highest grid resolution, even for intermediate values of $Re$. For example, for a spherical particle at the highest grid resolution, $C_D$ differs by

approximately 20% from the correlation expression of Haider and Levenspiel (1989) and Clift et al. (2005). Sommerfeld and Qadir investigated the hydrodynamic forces acting on highly irregular shaped particles in a flow channel for Reynolds numbers between 1 and 200 (Sommerfeld and Qadir, 2018). Results show a normal distribution for all coefficients over all particle shapes and orientations. In addition, the study concludes that the drag coefficient increases as the particles become more irregular in shape. Following their initial LBM study, Sommerfeld and Qadir formulated a stochastic modelling method whereby the fluid forces acting on a non-spherical particle in an Euler/Lagrangian approach are calculated using probability density functions (PDFs) for the drag, lift, and torque (Sommerfeld and Lain, 2018). The PDFs were estimated using data from the initial LBM simulations (Sommerfeld and Qadir, 2018). Trunk et al. (2018) used the homogenised LBM (HLBM) approach, which is a LBM variant that includes a smoother interpolation between the fluid and the particle solid than the Bouzidi bounce-back scheme, to compare the settling of arbitrarily shaped limestone particles and spheres. While this HLBM approach was not used to calculate hydrodynamic forces on the limestone particles, the drag and lift forces acting on a cylinder were calculated and compared with previous studies. A study such as that of Trunk et al. (2018) could be used to determine correlation functions for highly irregular particles.

### 3.4.3. Effect of boundaries

During fluidisation, particles will contact adjacent particles and, invariably, boundaries such as confining walls. Furthermore, even as a particle moves close to a boundary, the drag, lift, and torque experienced will differ from the case when the particle is distant from the boundary. To date, the majority of numerical studies have focused on the influence of boundaries for spherical particles (Zeng et al., 2009; Lee and Balachandar, 2010, 2017; Tsuji et al., 2013; Zhou et al., 2017; Ignatenko et al., 2017) while there have only been few studies on non-spherical particles (Gavze and Shapiro, 1997; Lee and Hyun, 2015; Zarghami and Padding, 2018).

In the study of Gavze and Shapiro (1997), the forces acting on prolate spheroids of varying aspect ratios in a shear flow near a rigid boundary were investigated in the Stokes limit. As the particle aspect ratio increased, the maximum lift force, which occurred at an incident angle $\phi = 45°$, also increased. Interestingly, the maximum lift force was observed at an aspect ratio $w \approx 3$ while particles with $w \approx 1$ (spheres) and $w = 10$ (highly prolate particles) were subject to smaller lift forces. At $w \approx 1$, this is unsurprising given that spherical particles are subject to negligible lift. For particles with $w = 10$, the major axis of the particle can extend far from the rigid boundary into a region of the system where the flow is unperturbed by the boundary. Gavze and Shapiro also derived correlation expressions for the drag, lift, and torque experienced by particles. For instance, the ratio of the lift force on a particle with aspect ratio $w$ at a distance $y$ from the boundary ($F_L$) and the lift force on a particle in an unbounded flow ($F_L^\infty$), i.e. a particle that is distant from a boundary, was expressed as

$$\frac{F_L}{F_L^\infty} = 1 + \frac{0.43 + 1.53/w}{y/a} + \frac{0.66/w}{(y/a)^2} \tag{25}$$

where $a$ is the major axis of the particle. The above expression is valid for particles with an aspect ratio in the range $1.11 < w < 10$. Additional expressions are available in Gavze and Shapiro (1997).

In a recent study motivated by particle-based drug delivery systems and the forces experienced by particles in vascular flows, Lee et al. assessed the variation of drag, lift, and torque on non-spherical particles near walls in Stokes flow using ANSYS FLUENT (Lee and Hyun, 2015). Although the flow field and forces on the particle were solved in 3D, the particles were not allowed to move in the depth direction, thus representing a pseudo-2D system. As the particle was moved closer to the boundary, the drag force and torque increased while the lift force was shown to oscillate around zero with changes in the particle orientation. Although Lee et al. did not provide correlations in the same manner as Gavze and Shapiro (1997), the simulations yielded insight with regards to the resistance portrayed by a particle as it translates and rotates in a flow.

Given the lack of studies on the hydrodynamic forces experienced by non-spherical particles beyond Stokes flow, we have made a first exploration of the drag, lift, and torque experienced by an ellipse of varying aspect ratio near a wall in a 2D flow channel using the LBM approach (Zarghami and Padding, 2018). A schematic of the flow configuration with associated boundary conditions is presented in Fig. 10.

Fig. 11 show the average drag, lift, and torque as a function of incident angle $\phi$ and various values of the gap width $h$ for an ellipse with an aspect ratio $w = 4$ and in a flow with $Re = 100$. As $\phi \to 0°$ or $\phi \to 180°$, the drag force tends to zero (Fig. 11(a)). With increasing $\phi$, the drag force increases and peaks at $\phi \to 90°$ as the frontal area of the particle facing the flow reaches the maximum value, and leads to maximum disturbance of the flow field. It should be noted that at $\phi = 90°$ the maximum drag force is observed when $h = a$. As the gap is decreased further, at $\phi = 90°$, the drag force decreases given that the wall slows down the flow through the gap at small $h$ and leads to a decrease in viscous drag.

Fig. 11(b) shows the variation of the lift force with $\phi$ for varying $h$. Unlike for drag force, the variation of lift force with $\phi$ is asymmetric. At $\phi = 0°$, the lift force is positive, indicating that the particle experiences a force directed away from the wall. As $\phi$ increases, the magnitude of the lift force increases for all $h$ and reaches a peak in all cases at $\phi \approx 45°$. However, at $\phi > 90°$, the lift force becomes negative, thus indicating a wall-directed lift force.

Finally, the variation of torque is illustrated in Fig. 11(c). The trends for torque are notably asymmetric, with the particle experiencing predominantly negative torques, especially when furthest from the wall. As $\phi$ increases from $0°$, a positive counter-clockwise torque on the particle results with a magnitude that increases with decreasing gap size. The maximum positive torque occurs for the smallest value of $h$. The continued increase of $\phi$ eventually leads to a negative clockwise torque on the particle. A negative torque emerges since the shear layer on the lower side of the particle directly interacts with the shear layer of the wall and almost cancel out each other. As a result, the shear layer on the upper side with a negative sign dominates leading to a clockwise rotation of the particle.

This investigation on the drag, lift, and torque experienced by ellipses close to a no-slip boundary is the first step towards a numerical study of ellipsoids in 3D configurations. We initially
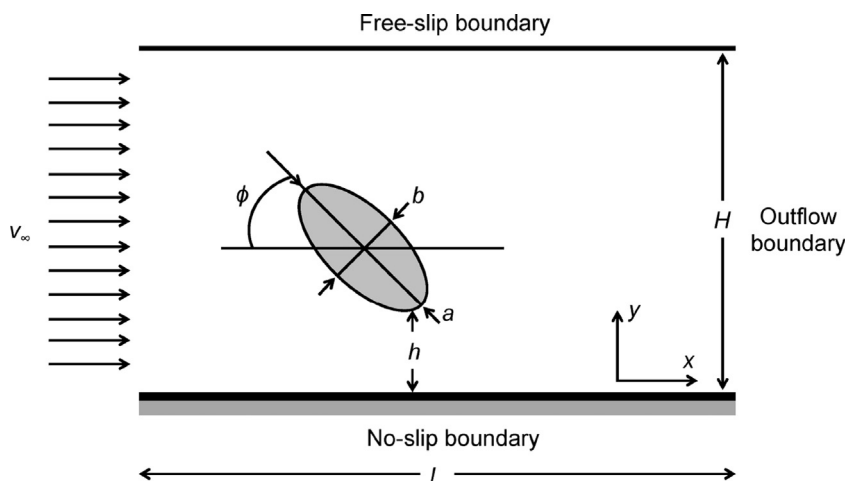


**Fig. 10.** Illustration of the flow configuration and boundary conditions for a prolate spheroid adjacent to a no-slip rigid boundary. $h$ is the gap between the base of the particle and the no-slip boundary. $a$ and $b$ are the lengths of the major and minor axes of the particle while the aspect ratio $w = a/b$.
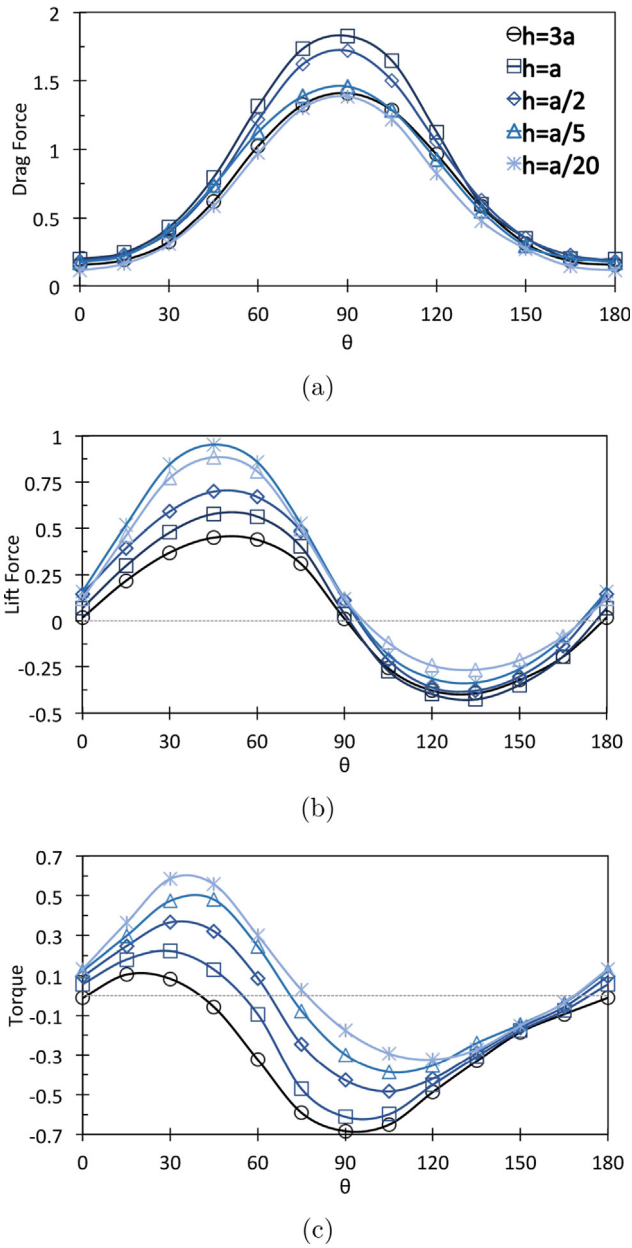
**Fig. 11.** Variation of the drag, lift, and torque with $\phi$ experienced by an ellipse with $w = 4$, $Re = 100$, and varying $h$. (a) Drag force. (b). Lift force. (c) Torque.

explored a 2D system given the lower number of degrees of freedom for an ellipse in comparison to the 3D case. In 2D, an ellipse has five degrees of freedom - centre of mass coordinates, the major diameter ($a$), the minor diameter ($b$) and the incident angle $\phi$. As demonstrated in the study, the forces are also dependent on $Re$, distance of the particle from the wall, and aspect ratio. In 3D, an ellipsoid has nine degrees of freedom - centre of mass coordinates, the semi-major diameter, the semi-intermediate diameter, the semi-minor diameter, and the three Euler angles associated with orientation. A complementary 3D study would therefore require exploration of a substantially larger parameter space.

### 3.5. The role of machine learning

While the aforementioned correlation functions for the drag, lift, and torque coefficients have been formulated in part using expressions based on the expected flow physics in different regimes, an alternative approach can be used to define and estimate these expressions. Symbolic regression is a new framework for regression analysis that is part of the genetic programming algorithms family first proposed by Koza (1994). It is a data-based machine learning algorithm that is very efficient in detecting mathematical relations between data. Thus, it facilitates finding expressions that are representative of the physics associated with the problem at hand. The principle difference between symbolic regression and other regression methods such as non-linear regression (Kass, 1990) is that the latter can only consider one equation per regression run, while the former can evaluate billions of equations in a single run. Symbolic regression searches the space of mathematical functions using methods similar to genetic evolution (Kass, 1990), where mathematical expressions are generated through mutations and random combinations. Initially, the symbolic regression algorithm is provided with selected mathematical functions that are specific to the problem investigated and act as the initial guess for a solution. The next step, which is the essential step of the algorithm, is referred to as breeding whereby offspring, which are modified versions of the initial mathematical function, are generated. They can be generated by either a crossover of the initial mathematical functions or with the introduction of a random mutation to the function that adds a new function to the existing space of functions. Fig. 12 shows an example of a mutation process for the mathematical function $\tan(1 + \cos(x))$. After breeding, the fitness of the offspring functions are evaluated with regards to how closely they capture the supplied data sets. Finally, the last step is the selection process where the offspring that have the highest fitness are selected. The majority of symbolic regression algorithms seek a balance between model complexity and accuracy. This approach allows for a deeper understanding of the underlying physics of the problem and also eliminates the possibility of overfitting.
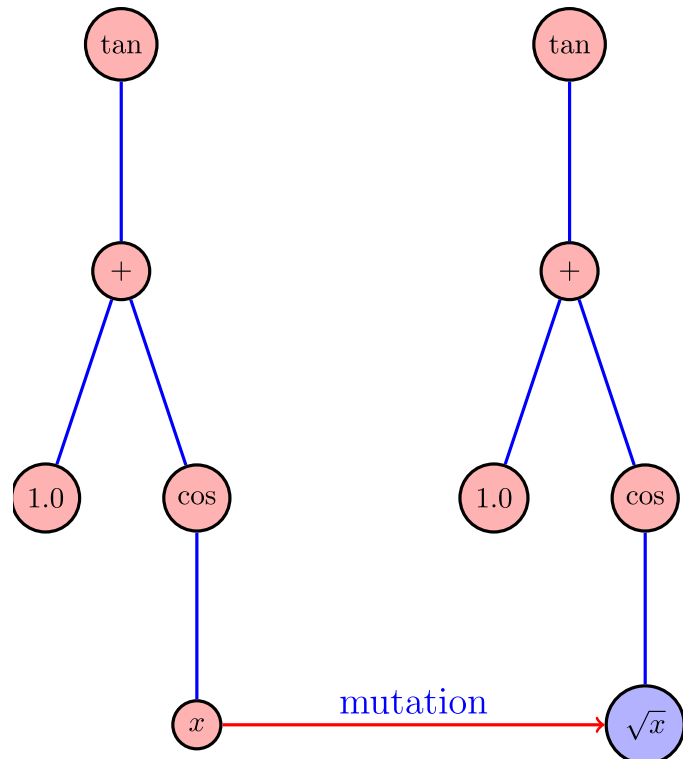


**Fig. 12.** Example of mutation process for the mathematical function $\tan(1 + \cos(x))$.

Given the functionality of symbolic regression, it is appealing to use this tool to obtain fitting correlations for hydrodynamic drag, lift, and torque from numerical data similar to that used to find the correlations defined previously (Sanjeevi et al., 2018). However, we believe that the most beneficial use for the methods of machine learning, such as symbolic regression, is in exploring their capability to obtain accurate predictive fitting equations in a higher parameter space from data obtained from a lower parameter space. For instance, the correlation expressions of Sanjeevi et al. (2018) are a function of $Re$ and the particle orientation $\phi$. However, we would like to extend the correlation expression to also account for the aspect ratio of the elongated particle using data that contains information as to how drag, lift, and torque vary with $Re$ and $\phi$. This can be achieved by using semi-supervised methods that can learn from data sets such that any input data is not associated with the output data. For instance, in such a case, the number of input data sets can exceed that of the output data sets. An attractive aspect of using symbolic regression with semi-supervised learning is the use of previous knowledge, such as functional dependencies in certain regimes of the problem under investigation. This would significantly reduce the time needed for DNS simulations. Currently, using a set of data, machine learning algorithms based on genetic programming can predict the mathematical structure of the coupled ordinary differential equations in an approach known as the advanced symbolic regression algorithm (Schmidt and Lipson, 2009). Alternatively, a more advanced method such as sparse identification can be used to ascertain the nature of the partial differential equations that best capture a data set (Brunton et al., 2016). For example, sparse identification algorithms can be used to identify the transport equation or equations that describe behaviours in fluidised beds, while advanced symbolic algorithms can assist in the formulation of a system of predictive equations that govern the fluidisation process of particulate flows. Thus, machine learning solvers such as symbolic regressions are an attractive approach for the evaluation of precise correlation functions to approximate hydrodynamic forces for elongated particles subject to variation in parameters such as $Re$, $\phi$, and aspect ratio. In addition, this approach can be applied to a multitude of length scales given that machine learning algorithms are not subject to spatial or temporal resolution constraints.

## 4. Laboratory-scale simulations: CFD-DEM

CFD-DEM is a powerful numerical tool that can be used to study dense gas-solid flows in fluidised beds (Deen et al., 2007; van der Hoef et al., 2006, 2008; Goniva et al., 2012; Zhong et al., 2016; Mahajan et al., 2017, 2018; Mema et al., 2017, 2019) as well as jet formation and cratering in granular packings (Kuang et al., 2013), gas-solid flows in cyclones (Chu et al., 2011), reacting flows in fluid catalytic cracking processes (Wu et al., 2010), stick-slip behaviour in a sheared granular fault (Dorostkar and Carmeliet, 2018), and discharge of lunar soil from a closed container similar to that included on a lunar space rover (Otto et al., 2018). Unlike DNS, CFD-DEM does not fully resolve the fluid flow in the vicinity of particles. Instead, fluid-solid interactions are included using hydrodynamic closures. Various coupling approaches between the phases can be utilised, depending on the solid volume fraction $\epsilon_s$ (van der Hoef et al., 2006). For fluid-solid suspensions in fluidized bed reactors where $\epsilon_s > 10^{-3}$, "four-way coupling" is required since the fluid affects the solid particles, the particles affect the fluid, and the particles interact with each other and the walls. The CFD-DEM approach consists of two coupled algorithms, which are computational fluid dynamics (CFD) (Anderson et al., 1995; Versteeg and Malalasekera, 2007) for the fluid phase and discrete element method (DEM) (Cundall and Strack, 1979) for the solid particle phase. CFD is used to evolve the (averaged) interstitial fluid between the particles while DEM represents the solid phase as soft deformable particles that exert forces on other particles and any boundaries upon contact. In this section, we outline the key steps for the implementation of a CFD-DEM study that are specific for elongated particles subject to a fluid flow. Theoretical considerations for the CFD-DEM modelling of other non-spherical particle shapes are available in Zhong et al. (Zhong et al., 2016). After briefly introducing the implementation of CFD, we present details of DEM and specific considerations for elongated particles.

### 4.1. Computational fluid dynamics (CFD)

The evolution of the fluid phase using a CFD approach involves the solution of the equations for continuity and momentum transport. For an incompressible fluid, the equation of continuity is

$$\frac{\partial \left( \epsilon_f \rho_f \right)}{\partial t} + \nabla \cdot \left( \epsilon_f \rho_f \mathbf{v}_f \right) = 0 \tag{26}$$

where $\epsilon_f$ is fluid volume fraction, $\rho_f$ fluid density, and $\mathbf{v}_f$ is the fluid velocity. Momentum conservation is expressed as

$$\frac{\partial \left( \epsilon_f \rho_f \mathbf{v}_f \right)}{\partial t} + \nabla \cdot \left( \epsilon_f \rho_f \mathbf{v}_f \mathbf{v}_f \right) = -\epsilon_f \nabla p + \nabla \cdot \left( \epsilon_f \boldsymbol{\tau_f} \right) + \mathbf{R}_{f,p} + \epsilon_f \rho_f \mathbf{g} \tag{27}$$

where $\boldsymbol{\tau}_f$ is the fluid stress tensor, $\mathbf{R}_{f,p}$ represents the momentum exchange between the fluid and particle phases, and $\mathbf{g}$ is gravity. Discretized versions of Eqs. (26) and (27) can be solved using the Pressure Implicit with Splitting of Operators (PISO) algorithm or the Semi-Implicit Method for Pressure-Linked Equation (SIMPLE) algorithm (Versteeg and Malalasekera, 2007). Further details on both PISO and SIMPLE can be found in the literature (Versteeg and Malalasekera, 2007; Hilton et al., 2010). When solving the fluid flow, careful consideration must be made with regards to the size of a grid cell. If the grid size is too large, crucial aspects of the fluid flow will be averaged out, while a grid size that is too small relative to the particle size can lead to anomalies in the solution (Clarke et al., 2018).

### 4.2. Discrete element method (DEM)

The discrete element method (DEM) of Cundall and Strack (Cundall and Strack, 1979) is one of the most important models currently applied to study discrete granular particle systems. The DEM approach was initially developed to simulate rock mechanics and resolve stresses between particles inside rock samples (Cundall, 1971). Development of the algorithm was further motivated by the failure of an analytical model of cubic arrays of discs or spheres (Deresiewicz, 1958) to accurately capture internal stresses recovered from experiments on packings of photoelastic disks (de Josselin de Jong and Verrujit, 1969).

In DEM, particles trajectories are determined by contact interactions with other grains and any confining boundaries. Contacts with grains create inter-particle forces that are used in DEM to evolve particle positions by integrating Newton's equations of motion. The stiffness of particles in DEM is typically chosen to be lower than the realistic particle stiffness as ascribed by Young's modulus of the material. Such a choice facilitates faster evaluation of prolonged particle contacts by allowing for a larger time step in the integration scheme. This approach is satisfactory, provided the contact time is shorter than the mean free time between subsequent collisions. Particle deformation during a contact is approximated by the overlap between two particles and used in the calculation of the resulting contact force.

In the field of granular materials DEM has been applied to model laboratory scale experiments such as the shear of grains in a planar geometry (Aharonov and Sparks, 1999, 2002; Fitzgerald et al., 2014), shear in a Couette geometry (Schöllmann, 1999; Latzel et al., 2000, 2003), and jet formation in impacted granular packings (Lohse et al., 2004). DEM has also been used to study a variety of industrial situations such as grinding processes in ceramics (Jiang et al., 2015), die filling for the manufacturing of pharmaceutical tablets (Wu, 2008), processes in agriculture (Tijskens et al., 2003), flows in hopper geometries (Balevicius et al., 2011; Cleary and Sawley, 2002), particle flows in rotating drums (Poschel and Schwager, 2004; Komossa et al., 2014; Xiao et al., 2017), and the filling of silos (Holst et al., 1999).

### 4.2.1. Equations of motion and inter-particle forces

Consider a particle $i$ with mass $m_i$ moving with a velocity $\mathbf{v}_i$ in a gas-solid system such as a fluidised bed. The translational motion of the particle can be calculated via the integration of

$$m_i \frac{d\mathbf{v}_i}{dt} = \sum_j \left( \mathbf{F}_{ij,n} + \mathbf{F}_{ij,t} \right) + \mathbf{F}_{i,f} + \mathbf{F}_{i,p} + \mathbf{F}_{i,b} \tag{28}$$

where the sum runs over all neighbours $j$ in contact with particle $i$, $\mathbf{F}_{ij,n}$ is the normal contact force acting on particle $i$ due to its interaction with particle $j$, $\mathbf{F}_{ij,t}$ is the tangential contact force acting on particle $i$ due to its interaction with particle $j$, $\mathbf{F}_{i,f}$ is the total hydrodynamic force acting on particle $i$, $\mathbf{F}_{i,p}$ represents the pressure gradient (buoyancy) force acting on particle $i$, and $\mathbf{F}_{i,b}$ is any body force acting on particle $i$ including gravity. The rotational motion of particle $i$ is solved using

$$\frac{d(\mathbf{I}_i \cdot \boldsymbol{\omega}_i)}{dt} = \sum_j \mathbf{T}_{ij} + \mathbf{T}_{i,f} + \mathbf{T}_{i,external} \tag{29}$$

where $\mathbf{I}_i$ is the moment of inertia tensor of particle $i$, $\boldsymbol{\omega}_i$ is the angular velocity of particle $i$, $\mathbf{T}_{ij}$ is the contact torque acting on particle $i$ due to its interaction with a neighbouring particle $j$, $\mathbf{T}_{i,f}$ is the fluid-induced torque acting on particle $i$, and $\mathbf{T}_{i,external}$ is any external torque acting on particle $i$. Particle velocities, positions, and orientations are evolved by time integration subject to a fixed integration time step using an approach such as the Velocity-Verlet method.

Under experimental conditions, the contact force $\mathbf{F}_{ij}$ between two contacting particles $i$ and $j$ is distributed across the contact surface. However, in DEM, contacts between adjacent particles are approximated as particle overlaps. Therefore, the contact force is assumed to act at a single point in the centre of the overlap region. In the next section, approaches for the identification of inter-particle contacts and the contact point for various particles shapes are presented. Here the focus is on the numerical description of the normal and tangential components of the contact force when a contact is identified between two particles. The normal contact force $\mathbf{F}_{ij,n}$ between two particles $i$ and $j$ can be written as

$$\mathbf{F}_{ij,n} = \mathbf{F}_{ij,el} + \mathbf{F}_{ij,dis} \tag{30}$$

where $\mathbf{F}_{ij,el}$ represents the elastic repulsion and $\mathbf{F}_{ij,dis}$ is associated with the kinetic energy dissipation. A number of normal contact force model approaches are available in the literature (Schäfer et al., 1996; Džiugys and Peters, 2001; Poschel and Schwager, 2004; Kruggel-Emden et al., 2007). A popular representation of the normal interaction in DEM is a linear spring-dashpot scheme where the elastic component is described by a linear spring and the dissipative component is represented as a dashpot, which can be expressed as

$$\mathbf{F}_{ij,n} = -k_n \delta_n \boldsymbol{n}_{ij} - \eta_n \mathbf{v}_{ij,n} \tag{31}$$

where $k_n$ is the normal spring constant, $\delta_n$ is the degree of overlap between the particles, $\mathbf{n}_{ij}$ is the normal unit vector, $\eta_n$ is a phenomenological damping coefficient, and $\mathbf{v}_{ij,n}$ is the normal relative velocity between the particles at the location of the contact point. Both $k_n$ and $\eta_n$ depend on material properties such as the particle stiffness and the coefficient of normal restitution $e_n$.

The linear spring-dashpot model in Eq. (31) assumes a constant $e_n$ at any impact speed. In reality, the amount of energy dissipation depends on the maximum amount of deformation, and therefore on the impact speed. This physics can be addressed by using a non-linear spring-dissipative model based upon the Hertz theory of elastic contacts (Schäfer et al., 1996; Kruggel-Emden et al., 2007; Antypov and Elliott, 2011) which is given as

$$\mathbf{F}_{ij,n} = -k_n^{\mathrm{Hertz}} \delta_n^{3/2} \phi_{ell}^{-3/2} \boldsymbol{n}_{ij} - \eta_n \mathbf{v}_{ij,n} \tag{32}$$

where $k_n^{\mathrm{Hertz}}$ is the Hertzian spring constant and $\phi_{ell}$ is a factor that takes into consideration the geometry of the elliptical contact area. When a circular contact area is assumed, $\phi_{ell} = 1$ (Kumar et al., 2018). The constant $k_n^{\mathrm{Hertz}}$ is given by

$$k_n^{\mathrm{Hertz}} = \frac{4}{3} E_{\mathrm{eff}} \sqrt{R_{\mathrm{eff}}}. \tag{33}$$

In Eq. (33) $E_{\mathrm{eff}}$ is the effective elastic modulus for the particle contact and expressed as

$$E_{\mathrm{eff}} = \left[ \frac{(1 - v_1^2)}{E_1} + \frac{(1 - v_2^2)}{E_2} \right]^{-1} \tag{34}$$

where $E_i$ and $v_i$ are the elastic modulus and Poisson's ratio for the $i$th particle. $R_{\mathrm{eff}}$ is the effective particle radius; for the simple case of two spheres $R_{\mathrm{eff}} = \frac{R_i R_j}{R_i + R_j}$. An expression for $R_{\mathrm{eff}}$ of an elliptical contact area is also available in the literature (Kumar et al., 2018). For spherocylindrical particles, it has been demonstrated that a linear-dashpot model or a Hertzian force model where a circular contact area is assumed are more than sufficient for studies on force data and the bulk properties of particle packings. On the other hand, if more detailed information on particles contacts such as area, overlap, duration, and frequency are required, then a Hertzian force model that accounts for variable contacting areas should be employed (Kumar et al., 2018).

If the tangential relative velocity $\mathbf{v}_{ij,t}$ at the contact point is non-zero at the start of a particle contact, then the interaction is oblique and as a result, the particles experience tangential forces. There are a number of schemes available for the description of tangential forces (Schäfer et al., 1996; Poschel and Schwager, 2004). For brevity, we highlight the Coulomb-type friction expression for the magnitude of the tangential force, given by

$$F_{ij,t} = \min \left( \left| -k_t \boldsymbol{\delta}_t - \eta_t \mathbf{v}_{ij,t} \right|, \mu \left| \mathbf{F}_{ij,n} \right| \right) \tag{35}$$

where $k_t$, $\delta_t$, $\eta_t$, and $\mu$ are the tangential spring constant, tangential overlap vector, tangential damping coefficient, and friction coefficient respectively. $\delta_t$ is calculated using the time integral of the tangential relative velocity at the contact point since the development of the initial particle contact (Mahajan et al., 2018).

Implicit to any force scheme are parameters associated with the elastic and dissipative responses whose values are dependent on particle material parameters. The two traditional approaches used to estimate representative values of DEM parameters are calibration and measurement (Marigo and Stitt, 2015; Coetzee, 2017). For the calibration approach, the DEM parameters in simulations are varied until acceptable correspondence of specific bulk properties from experiments and simulations is reached. This approach is iterative, meaning that DEM parameters must be suitably varied to enable convergence of the data sets. For the measurement

approach, the material properties are measured at the particle or contact scale (Coetzee, 2017). For instance, the coefficient of restitution can be measured via high-speed imaging of colliding particles (Wang et al., 2008; Mahajan et al., 2018) while the rolling friction for particles can be inferred from the motion of near-spherical particles down an incline (Ketterhagen et al., 2010).

Particle shape can also influence the measured material parameters (Marigo and Stitt, 2015; Coetzee, 2017). It is not sufficient to just measure the material parameters for a spherical particle made from the same material as the non-spherical particle geometry of interest. Collisions between non-spherical particles can lead to complex post-collision trajectories and thus complicate the process of making an accurate estimation of the coefficient of restitution. In general, it is advisable to apply statistical analysis procedures as part of a systematic method to demonstrate the importance of certain DEM parameters, such as Young's modulus and the coefficient of rolling friction, and hence aid in the timely selection and calibration of these parameters (Yan et al., 2015). Alternatively, parameters can be estimated using a weighted least squares fitting approach for experimental data (Kruggel-Emden et al., 2007) with the parameters then used as input for DEM simulations.

### 4.2.2. DEM collision detection schemes

As outlined previously, particles in fluidised bed reactors for biomass processing tend to be elongated in nature and can be represented as fibres, rods, spherocylinders, or ellipsoids. For any DEM simulation, the most important step is the identification of particle contacts. Any contact detection algorithm must satisfy three primary requirements. Firstly, the algorithm should accurately detect a contact between particles. Secondly, the algorithm should determine the contact point and the associated contact tangent. Finally, the algorithm should calculate the magnitude of the particle overlap, which is used to calculate the normal contact force subject to a specified force law. A number of pertinent collision detection schemes for particle shapes relevant to fluidisation processes are now presented.

The simplest representation of a solid particle in CFD-DEM simulations is a sphere. A sphere can be described by a single parameter *i.e.* the particle radius, and has no discernible orientation. Two spherical grains of radius $R_i$ and $R_j$ are deemed to be in contact

when the length of the vector between their respective centres of mass $\mathbf{r}_{ij}$ is less than the sum of their radii. The degree of overlap $\delta_n$ can be referred to as the mutual compression of the particles and expressed mathematically as

$$\delta_n = R_i + R_j - |\mathbf{r}_{ij}|. \tag{36}$$

Spheres (discs in two-dimensional studies) have been extensively used to represent particle shapes in simulations of gas-solid flows (Tsuji et al., 1993; Xu and Yu, 1997; Deen et al., 2007; Zhu et al., 2008; van der Hoef et al., 2008). Although spherical particles allow for rapid numerical simulations, their geometry is too simplistic to capture the realistic hydrodynamic and contact forces experienced by a particle. For spherocylindrical particles, contact detection is more complicated than for the case of spheres, as shown in Fig. 13. Two spherocylindrical particles are in contact when the shortest distance between their shafts is smaller than the sum of their respective radii such that $|\mathbf{s}_2 - \mathbf{s}_1| < 2R_p$ where $\mathbf{s}_1$ and $\mathbf{s}_2$ are the end points of the line connecting the two shafts of the particles. Therefore, the principle aim of any contact detection algorithm for spherocylinders is to calculate $\mathbf{s}_1$ and $\mathbf{s}_2$ (Pournin et al., 2005; Vega and Lago, 1994; Mema et al., 2019; Mahajan et al., 2017, 2018; Marschall and Teitel, 2018).

It is instructive to show a brief derivation of the locations $\mathbf{s}_1$ and $\mathbf{s}_2$. Parametric equations for the shafts of particles $P_1$ and $P_2$ can be written as

$$\xi_{P_1} : \lambda \mapsto \mathbf{r}_1 + \lambda\mathbf{u}_1 \tag{37}$$

$$\xi_{P_2} : \psi \mapsto \mathbf{r}_2 + \psi\mathbf{u}_2 \tag{38}$$

where $\mathbf{r}_1$ and $\mathbf{r}_2$ are the centres of mass of particles 1 and 2, respectively, $\mathbf{u}_1$ and $\mathbf{u}_2$ are the unit orientation vectors of their shafts, and $\lambda \in [-l_p/2, l_p/2]$ and $\psi \in [-l_p/2, l_p/2]$. Using these parametric equations, the vector $\mathbf{r}$ between the shafts can be expressed as

$$\mathbf{r} = \xi_{P_2} - \xi_{P_1} = \mathbf{r}_{12} + \psi\mathbf{u}_2 - \lambda\mathbf{u}_1. \tag{39}$$

with $\mathbf{r}_{12} = \mathbf{r}_2 - \mathbf{r}_1$. Without constraints on $\lambda$ and $\psi$, the squared distance is given by

$$r^2 = r_{12}^2 + \psi^2 + \lambda^2 + 2\psi\mathbf{u}_2 \cdot \mathbf{r}_{12} - 2\lambda\mathbf{u}_1 \cdot \mathbf{r}_{12} - 2\lambda\psi\mathbf{u}_2 \cdot \mathbf{u}_1. \tag{40}$$

Calculation of the minimum distance is achieved via the minimisation of $r^2$ leading to preliminary values of $\lambda$ and $\psi$:
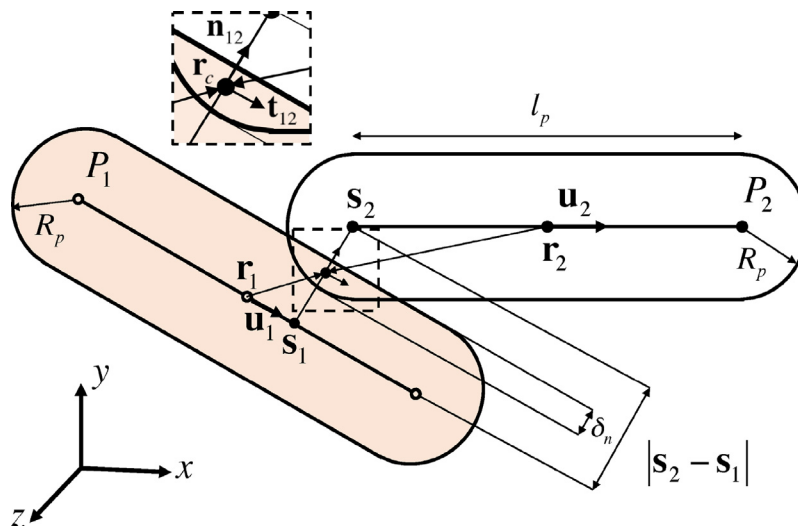


**Fig. 13.** A schematic of a sample contact between two spherocylinders with each having a shaft length $l_p$ and characteristic radius $R_p$. $\mathbf{s}_1$ and $\mathbf{s}_2$ represents the points on particles $P_1$ and $P_2$ respectively for which the shortest distance between the particles results. $\mathbf{r}_i$ is the centre of mass, $\mathbf{u}_i$ is the orientation unit vector originating at $\mathbf{r}_i$ and $\mathbf{v}_i$ is the translational velocity. The mid-point between $\mathbf{s}_1$ and $\mathbf{s}_2$ can be denoted as $\mathbf{r}_c$ and the degree of overlap between the particles is $\delta_n$. $\mathbf{n}_{12}$ and $\mathbf{t}_{12}$ are the normal and tangential unit vectors for the contact respectively, which are shown in the inset image. Image adapted from Mema et al. (2019).

$$\lambda^* = \frac{(\mathbf{r}_{12} \cdot \mathbf{u}_1) - (\mathbf{r}_{12} \cdot \mathbf{u}_2)(\mathbf{u}_1 \cdot \mathbf{u}_2)}{1 - (\mathbf{u}_1 \cdot \mathbf{u}_2)^2}, \tag{41}$$

$$\psi^* = \frac{-(\mathbf{r}_{12} \cdot \mathbf{u}_2) + (\mathbf{r}_{12} \cdot \mathbf{u}_1)(\mathbf{u}_1 \cdot \mathbf{u}_2)}{1 - (\mathbf{u}_1 \cdot \mathbf{u}_2)^2}. \tag{42}$$

If either or both $\lambda^*$ and $\psi^*$ are outside the range $[-l_p/2, l_p/2]$, corresponding to a contact at the hemispherical end of the spherocylinder, they are clipped to $\pm l_p/2$. These final values of $\lambda^*$ and $\psi^*$ are then reinserted in Eqs. (37) and (38) to find the locations $\mathbf{s}_1$ and $\mathbf{s}_2$, and the shortest distance between the particles can be evaluated by inserting the values for $\lambda^*$ and $\psi^*$ in Eq. (39) or Eq. (40). Further details on the collision detection algorithm can be found in the paper of Mahajan et al. (2018).

In an idealised case, two spherocylinders are perfectly parallel when $1 - (\mathbf{u}_1 \cdot \mathbf{u}_2)^2 = 0$. However, due to numerical accuracy, two particles are taken to be parallel when $1 - (\mathbf{u}_1 \cdot \mathbf{u}_2)^2$ is sufficiently small, e.g. less than $10^{-6}$. Once the values of $\lambda^*$ and $\psi^*$ have been attained, $\mathbf{s}_1, \mathbf{s}_2$, and $\mathbf{r}_c$, which is the mid-point between $\mathbf{s}_1, \mathbf{s}_2$ (Fig. 13), can be easily calculated.

An ellipsoid is a specific example of a superquadratic (Džiugys and Peters, 2001; Williams and Pentland, 1992) with the general formula for a superquadratic in a (body-fixed) Cartesian coordinate system given by

$$\left| \frac{x}{a} \right|^{\epsilon_1} + \left| \frac{y}{b} \right|^{\epsilon_2} + \left| \frac{z}{c} \right|^{\epsilon_3} = 1 \tag{43}$$

where $a, b$, and $c$ are the principal semi-axes of the ellipsoid, and $\epsilon_1, \epsilon_2$, and $\epsilon_3$ are powers such that $0 < \epsilon_1, \epsilon_2, \epsilon_3 < \infty$. It has been suggested that up to 80% of solids can be represented as a superquadratic (Williams and Pentland, 1992). Thus, a precise identification of contacts between ellipsoids is imperative for the numerical reproduction of particle dynamics in real processes. A number of contact detection schemes are available in the literature such as the intersection algorithm (Rothenburg and Bathurst, 1991; Ting, 1992; Lin and Ng, 1995; Džiugys and Peters, 2001), the geometrical potential algorithm (Lin and Ng, 1995; Džiugys and Peters, 2001; Džiugys and Peters, 2001), and the common normal concept (Lin and Ng, 1995; Kildashti et al., 2018).

In the intersection algorithm, the intersection points $A$ and $B$ between two overlapping ellipses are calculated, and thereafter used to calculate the midpoint between the points $C$ (Fig. 14(a)). The points $A$ and $B$ are calculated via the analytical or iterative solution of a quartic polynomial equation. While this algorithm can identify the intersection points for large overlaps, the algorithm encounters accuracy and stability issues when the overlap area between particles is small. Similar issues also arise when the semi-axes of two ellipses are aligned to each other. In these sit-

uations, the quartic equation can be ill-conditioned and thus lead to erroneous solutions. This approach is best suited for contacting ellipses (2D) with the extension of the algorithm to ellipsoids in 3D, where the intersection of two particles, denoted as a curve, is not trivial (Ting, 1992; Lin and Ng, 1995; Džiugys and Peters, 2001).

The geometrical potential algorithm provides a more stable scheme for contact detection between ellipsoids (Ng, 1994; Ting, 1992; Lin and Ng, 1995; Džiugys and Peters, 2001). A contact as described by the geometrical potential algorithm is illustrated in Fig. 14(b). In this contact scheme, the contact point $C$ is calculated as the midpoint of $T_i$ and $T_j$, where $T_i$ is defined as the deepest point of particle $i$ inside particle $j$ while $T_j$ is the deepest point of particle $j$ inside particle $i$. One approach is based on the formulation of a quartic equation (Ting, 1992) while a second approach establishes a trigonometric equation that is equivalent to the quartic equation (Ng, 1994). In addition, a geometric potential algorithm has been derived for ellipsoids (Lin and Ng, 1995; Zhou et al., 2011).

Here, we elaborate further on the quartic equation approach (Ting, 1992) in Fig. 15. This approach allows for a better-conditioned quartic polynomial in comparison to the intersection method. The function $g(x,y) = c$ associated with ellipse $j$ is the family of ellipses with the same origin, orientation, and an aspect ratio that depends on $c$. One ellipse from this family of functions just touches the ellipse $i$ described by the function $f(x,y) = 0$ at $T_i$. In the same manner, $f(x,y) = c'$ is a function associated with ellipse $i$ that just touches ellipse $j$ at $T_j$. An additional function
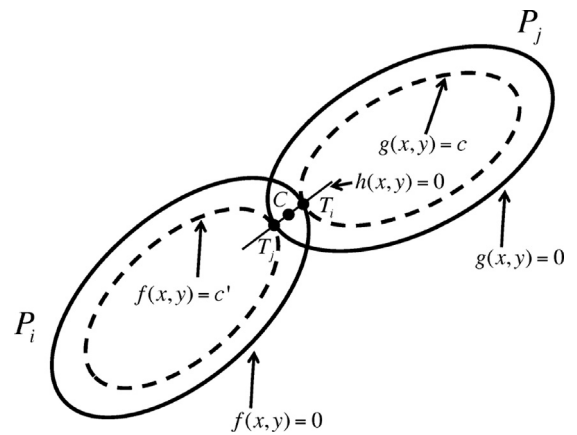


**Fig. 15.** Quartic equation approach for the geometrical potential algorithm to locate the contact point $C$ between two overlapping ellipsoids.
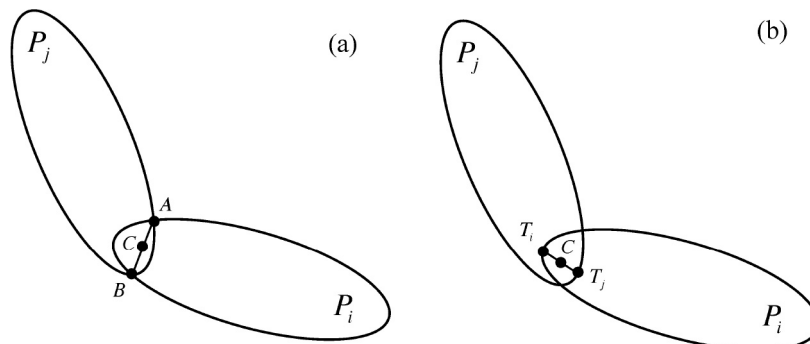


**Fig. 14.** Example of an overlapping contact between two ellipsoids $P_i$ and $P_j$. (a) Contact as described by the intersection algorithm. The points $A$ and $B$ are the intersection points of the two ellipses while $C$ is the midpoint of these intersection points. (Right) Contact as described by the geometrical potential algorithm. The point $T_i$ is the deepest point inside the particle $j$ while $T_j$ is the deepest point inside the particle $i$. Point $C$ is the contact point and the midpoint of the line joining $T_i$ and $T_j$.

$h(x,y) = 0$ is the locus of points where the ellipses $f(x,y) = c'$ and $g(x,y) = c$ have the same slope. The function $h(x,y) = 0$ intersects the functions $f(x,y) = 0$ and $g(x,y) = 0$ at approximately right angles, which allows for the formulation of two quartic functions that are well-conditioned. These equations can then be combined to calculate either analytically or iteratively the contact point $C$ between $T_i$ and $T_j$. Further details on this approach and other geometrical potential algorithms are available in the literature (Ng, 1994; Ting, 1992; Lin and Ng, 1995; Džiugys and Peters, 2001; Zhou et al., 2011,).

Spheres, spherocylinders, and ellipsoids all represent regular or symmetric particle shapes for which collision detection schemes can be analytically formulated. However, in reality, particles do not exhibit such precise symmetry and can have highly irregular shapes. Thus, a number of collision detection schemes are available for irregularly shaped particles (Džiugys and Peters, 2001; Zhong et al., 2016).

A popular approach for the representation of non-spherical particles is the composite sphere or multi-sphere approach whereby a complex particle is depicted as a combination of several spherical particles (Džiugys and Peters, 2001; Matsushima and Saomoto, 2002; Poschel and Schwager, 2004; Bing et al., 2014; Zhao et al., 2015; Zhong et al., 2016). For example, cylindrical particles can be depicted as a series of overlapping spheres (Bing et al., 2014) (Fig. 16) while more complicated shapes can be composed of multiple spheres (Poschel and Schwager, 2004; Zhao et al., 2015). This approach takes advantage of the ease of calculating the overlap between contacting spheres. Highly irregular particles can be described in simulations using multiple overlapping spheres by first taking high resolution images of the particles (Matsushima and Saomoto, 2002; Katagiri et al., 2010). In one study, a micro X-ray scanner was used to generate high resolution CT images of Toyoura sand particles (Katagiri et al., 2010). The resulting particle shapes were then modelled as a group of spherical particles using the dynamic optimisation method (Matsushima and Saomoto, 2002). Results show that grains comprising of 10 spherical elements was sufficient to reproduce shear responses in experiments for dense particle configurations.

There are alternatives for the description of irregular particles that do not rely on spherical particle elements. In the concept of potential particles, a convex shaped particle can be represented as a polynomial function (Boon et al., 2013). Contact detection between two particles $i$ and $j$ amounts to a constrained minimisation problem where, for example, the function for particle $i$ ($f_i$) is minimised subject to the constraint $f_j = 0$. This algorithm has been successfully applied to packings of pointed tetrahedral particles, rounded tetrahedral particles, prisms, and cubes (Boon et al., 2013). An approach that couples a broad-phase and a narrow-phase contact detection scheme for convex shaped particles has recently been formulated (Seelen et al., 2018). Firstly, the broad-phase scheme, which is based on a bounding volume that completely envelopes a particle, is used to construct a list of feasible particle contact pairs. From this list, a narrow-phase algorithm, based upon Minkowski differences and the Gilbert-Johnson-

Keerthi (GJK) overlap algorithm, establishes which potential contact pairs are in contact. This algorithm has been applied to study random packings of various particle shapes including complex polyhedral shapes (Seelen et al., 2018).

Another approach for irregular particles is based on orientation discretisation and applicable to any shaped particle in both two and three dimensions (Dong et al., 2015). This method calculates the degree of overlap between particles without resorting to the solution of polynomial functions. For any arbitrary shape, a database of the overlap between two particles for varying orientations and centre of mass separations is constructed prior to simulation. When two particles overlap during a simulation, their respective orientations and centre of mass distance act as database lookup parameters for the degree of overlap between the particles. This method eliminates the need to calculate the overlap region at every time step and is proposed to be more accurate than the solution of polynomial functions (Boon et al., 2013). Regardless of particle shape or the numerical detection scheme, the aforementioned approaches all seek to identify the point of contact between overlapping particles. Once a contact has been identified, the extent of that contact can be quantified by measures such as the overlap distance $\delta_n$ or the overlap volume $V_O$, with these values then used to calculate the contact force subject to a prescribed force scheme. The use of overlap distance is deemed to be insufficient for irregular non-spherical particles such as polyhedrals (Govender et al., 2018) and even ellipsoids (Dong et al., 2015; Kildashti et al., 2018). In the case of two overlapping convex shapes with a single point of contact the particle radius $R$ can be replaced with the radius of the circumscribed sphere $R_c$ and the overlap distance calculated from

$$\delta_n = \sqrt{V_O/\pi R_c}. \tag{44}$$

This expression applies to the case of spheres where $V_O \approx \pi \delta_n^2 R$ and $\delta_n \ll R$ (Dong et al., 2015). In effect, calculation of the overlap distance from the overlap volume Eq. (44) presents an alternative method of calculating the overlap distance, thus showing the non-uniqueness of the overlap depth for non-spherical particles. The issues become even more complicated when considering two contacting polyhedral particles, which can have the same overlap distance for a multitude of particle orientations. However, each contact arrangement can have a differing overlap volume. Thus, basing the contact force on the overlap distance can lead to erroneous estimates of the contact force (Govender et al., 2018). Both the overlap distance and overlap volume have been used in the calculation of contact forces in simulations of perturbed spherocylinder packings. For instance, in our studies on spherocylinders in fluidised beds, we calculated the overlap distance, which is defined graphically in Fig. 13, using the previously described scheme and then used this in the calculation of the normal contact force (Mema et al., 2019; Mahajan et al., 2018), while in DEM simulations of spherocylinder mixing in horizontal drums, the overlap distance was calculated using Eq. (44) (Yu et al., 2018), where the contact volume between spherocylinders is mainly assumed to be the same as that between two spheres. Different contact areas can be associ-
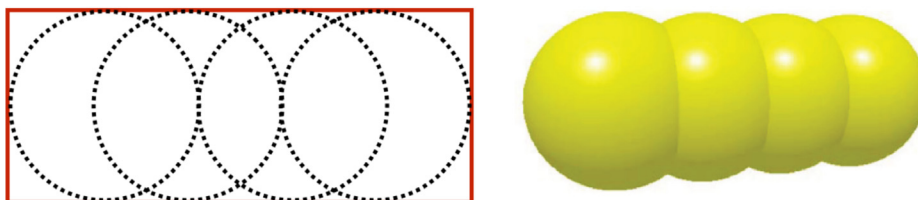


**Fig. 16.** Multi-sphere representation of a cylindrical particle. (Left) 2D view of a cylindrical particle represented by spheres. (Right) 3D view of a cylindrical particle from Bing et al. (2014).

ated with different contact scenarios as shown by Kumar et al. (2018), which can lead to better resolution of the normal and tangential forces. A key issue with using the overlap distance is the non-conservation of particle volume. One approach towards overcoming this issue is to redistribute the overlap volume over the non-overlapping surface of the particle, which would approximate real particle contacts where particle undergo deformation at the microscale. This has been defined for spheres (Haustein et al., 2017) but yet to be formulated for non-spherical particles such as spherocylinders.

### 4.2.3. Void fraction calculation schemes

As demonstrated in Section 4.1, calculations in the CFD scheme are dependent on the accurate calculation of the fluid volume fraction, otherwise referred to as the void fraction ($\epsilon_f$). A number of void fraction calculation schemes are available in the literature that must satisfy a series of conditions (Clarke et al., 2018). Firstly, the scheme must conserve the total volume of the solid particle phase at the grid-scale. Secondly, the scheme should predict a grid-independent void fraction field. Finally, the scheme should lead to smooth void fraction fields within densely packed particle phases. Violation of any of these conditions could lead to inaccuracies in the particle drag force, which in turn could lead to instabilities in the evolution of the fluid phase.

In terms of implementation, the particle-centred method (PCM) is the simplest void fraction calculation scheme. This scheme assumes that the total particle volume is located in the grid cell where the centre of mass of the particle is located. The void fraction for a grid cell $c$ as described by the PCM approach is given by

$$\epsilon_f^c = 1 - \frac{\sum_{p=1}^{N_p^c} V(p)}{V_{cell}^i} \qquad (45)$$

where $\epsilon_f^c$ is the void fraction for cell $c$, $N_p^c$ is the number of particles in cell $c$, $V(p)$ is the volume of the $p^{th}$ particle with its centre of mass in cell $c$, and $V_{cell}^i$ is the volume of the grid cell. This approach for the calculation of void fraction was used in the pioneering CFD-DEM investigation of fluidised beds by Tsuji et al. (1993). The PCM approach becomes problematic when particles intersect one or more grid cells. Note that this is more likely to occur for elongated particles than for spherical particles of equivalent volume. Large fluctuations in hydrodynamic forces can result when particle centres move between grid cells. For simulations of spheres where the PCM is used, it has been shown that these fluctuations do not emerge if the grid cell size is greater than 3.8 particle diameters (Peng et al., 2014). It is currently unknown what the critical grid cell size is for elongated particles such as spherocylinders.

To eliminate the grid cell transition effects, the particle volume can be assigned to grid cells subject to a geometrical approach known as the divided particle volume method (DPVM) (Clarke et al., 2018). This approach allows for the assignment of particle volume to multiple grid cells where applicable. Using DPVM, the void fraction in a cell is calculated using

$$\epsilon_f^c = 1 - \frac{\sum_{p=1}^{N_p^c} \phi_p^c V(p)}{V_{cell}^i} \qquad (46)$$

where $\phi_p^c$ is the volume fraction of particle $p$ in cell $c$. In this expression $N_p^c$ is the number of particles with centres located in the grid cell $c$ and in the neighbouring cells of $c$. In the cuboid DPVM approach, a particle is placed within a cuboid container. Thus a spherical particle is placed within a cube while a spherocylindrical particle is placed in a rectangular cuboid. For a spherocylindrical particle, $\phi_p^c$ is calculated from

$$\phi_p^c = \frac{\delta_x \delta_y \delta_z}{D_p^2 L_p} \qquad (47)$$

where $\delta_x, \delta_y$, and $\delta_z$ are the lengths of the cuboid that contains the particle portion in cell $c, D_p = 2R_p$ is the diameter of the particle, and $L_p = l_p + D_p$, the total length of the particle. For a sphere, $L_p = D_p$.

In our numerical studies of spherocylinders in fluidised beds, we have used the satellite point method (Hilton et al., 2010; Peng et al., 2016; Clarke et al., 2018) for the calculation of grid cell void fraction (Mema et al., 2017, 2019; Mahajan et al., 2017, 2018). In this method, which is conceptually between the PCM and DPVM approach, each particle is populated with a number of evenly-spaced satellite points $n_{sp}$ throughout the particle volume where each point is assigned an equal weight or fraction of the particle volume. The parent cell for a particle is identified subject to the centre of mass position $\mathbf{r}_i$. Particle volume is then assigned to the parent cell and the adjacent cells subject to the location of the satellite points on the underlying grid. When the entire volume is confined to the parent cell no distribution of particle volume is required. To optimise the approach, the number of satellite points and their associated weight can be varied.

The choice of void fraction scheme also influences the optimal grid cell size for the evolution of the fluid (Peng et al., 2014; Clarke et al., 2018). If the grid cell size is too large, then flow structures cannot be resolved while a grid cell that is too small can lead to anomalies in the solution of the continuity and Navier-Stokes equations for the fluid. For processes where boundaries are of relevance, such as in fluidised bed reactors, an excessively large grid cell size can affect the precision of boundary-fluid interactions. In simulations of spheres in a fluidised bed reactor with the PCM approach, an upper grid cell size of 3.8 particle diameters and lower grid size of 1.6 particle diameters is advised (Peng et al., 2014). For spherocylindrical particles, the equivalent limits would have to be expressed in terms of particle length, which could lead to a grid cell size that does not resolve flow structures. Given that we implement the satellite point method for spherocylindrical particles, these grid cell size limits are not applicable. We use a grid cell size such that a spherocylinder simultaneously intersects at most 2 grid cells in each Cartesian direction (Mema et al., 2019; Mahajan et al., 2018). For instance, we have used a particle length to grid cell size ratio of 1.25 (Mema et al., 2019). Although this value is below the lower limit advised for spheres with the PCM approach, the satellite point method is significantly more accurate than the PCM approach (Clarke et al., 2018).

### 4.2.4. Momentum exchange, voidage effects and gas-phase coupling

As presented in Eq. (28), the translational motion of an elongated particle in CFD-DEM depends on the total hydrodynamic force acting on the particle ($\mathbf{F}_{if}$), which is composed of the drag force and lift force, while the rotational motion (Eq. (29)) is dependent on the fluid-induced pitching torque $\mathbf{T}_{if}$. For an isolated elongated particle, the drag force, lift force, and torque can be calculated using the expressions and correlation functions derived using DNS methods given in Sections 3.4.1 and 3.4.2. In a fluidised bed reactor, these expressions and correlations are highly suited for particles in dilute regions of the reactor (solid fraction $\epsilon_s < 0.2$). As mentioned previously, He and Tafti studied the hydrodynamic forces experienced by ellipsoidal particles in dense packings with $\epsilon_s = 0.35$ subject to moderate Reynolds number ($Re = 200$) noting that drag, lift, and torque have correlation trends that are similar to trends for isolated particles. However, the authors did not present explicit multiparticle correlation functions. To address the lack of correlation functions, a number of approximations, some of which stem from studies on spherical particles,

can be applied for the case of elongated particles to account for variable voidage effects.

In CFD-DEM studies on spherical particles, the only hydrodynamic force considered is usually drag, given that lift and torque are deemed to be negligible. Thus, in Eq. (28), the term $\mathbf{F}_{i,f}$ can be replaced by a drag force term $\frac{V_i\beta}{\epsilon_s}(\mathbf{v}_f - \mathbf{v}_i)$ where $V_i$ is the particle volume and $\beta$ is the inter-phase momentum transfer coefficient. In beds of spherical particles, the Ergun expression (Ergun, 1952) is frequently applied for solid fraction $\epsilon_s > 0.2$, denoted as

$$\beta_{\text{Ergun}} = 150\frac{\mu_g \epsilon_s^2}{\epsilon_f d_p^2} + 1.75\frac{\rho_f \epsilon_s}{d_p}|\mathbf{v}_f - \mathbf{v}_i| \tag{48}$$

where $d_p$ is the diameter of the volume equivalent sphere. However, in the case of less dense configurations ($\epsilon_s < 0.2$), the Wen and Yu expression (Wen and Yu, 1966) can be applied, which is expressed as

$$\beta_{\text{WenYu}} = \frac{3}{4d_p}C_D \epsilon_s \epsilon_f^{-1.65}\rho_f|\mathbf{v}_f - \mathbf{v}_i|. \tag{49}$$

The combination of the Ergun (1952) and Wen and Yu (1966) leads to an abrupt or step change in the value of calculated drag force (Kafui et al., 2002). To avoid this step change in the drag force, an alternative to the Ergun/Wen and Yu correlations is to use the Di Felice approximation that accounts for the effect of neighbouring particles on the drag force experienced by a spherical particle (Di Felice, 1994), which is given by

$$\mathbf{F}_D(Re_p) = \mathbf{F}_{D0}\epsilon_f^{1-\chi} \tag{50}$$

where $\mathbf{F}_{D0}$ is the drag force experienced by an isolated particle (Eq. (5)) and $\chi$ is a correction factor given by

$$\chi = 3.7 - 0.65\exp\left[\left(-(1.5 - \log(Re_p))^2/2\right)\right] \tag{51}$$

and $Re_p$ is the particle Reynolds number defined earlier. For studies on the fluidisation of elongated particles, both the Ergun equation (Oschmann et al., 2014; Mahajan et al., 2018) and Di Felice's expression (Hilton et al., 2010; Vollmari et al., 2016; Gan et al., 2016; Mema et al., 2017, 2019) have been utilised. As an approximation, we have also applied the Di Felice expression to the lift force experienced by elongated particles (Mema et al., 2017). An updated expression for factor $\chi$ that includes the effects of porosity and Reynolds number has been defined by Rong et al. (2013) using lattice-Boltzmann simulations of flows through arrays of spherical particles and is given as

$$\chi = 2.65(\epsilon_f + 1) - (5.3 - 3.5\epsilon_f)\epsilon_f^2 \exp\left[\left(-(1.5 - \log(Re_p))^2/2\right)\right]. \tag{52}$$

This factor has been implemented in a study on the fluidisation of elongated particles with varying aspect ratio (Nan et al., 2016). In our CFD-DEM study, we have considered both the Ergun and Di Felice expression for drag force in dense domains of a fluidised bed where the minimum of the two expressions is taken as the drag force (Mahajan et al., 2018).

There are a number of alternatives to the Ergun equation and Di Felice expression. Using a particle-resolved DNS approach, Tenneti et al. derived an expression that accounts for voidage effects for flows through fixed arrays of monodisperse spheres (Tenneti et al., 2011). Variations in the normalised drag forces on the particle arrays were found to be fitted by

$$F_D(\epsilon_f, Re_p) = \frac{F_{\text{isol}}(Re_p)}{\epsilon_f^3} + F_{\epsilon_f}(\epsilon_f) + F_{\epsilon_f, Re_p}(\epsilon_f, Re_p). \tag{53}$$

The first term on the righthand side is the drag force on an isolated sphere, the second term is a component that depends on void frac-

tion only, and the final term is a component that depends on both the void fraction and $Re_p$. Full expressions for $F_{\text{isol}}(Re_p)$, $F_{\epsilon_f}(\epsilon_f)$ and $F_{\epsilon_f, Re_p}(\epsilon_f, Re_p)$ can be found in paper of Tenneti et al. (2011).

The expression of Tenneti et al. is based on sphere packings with $\epsilon_s \in [0.1, 0.5]$ and $Re_p \in [1, 300]$. However, in a fluidised bed composed of elongated particles with diameters of several millimetres, $Re_p$ can reach beyond 1000 (Sanjeevi et al., 2018). Therefore, a drag correlation that accounts for voidage effects and is applicable to large Reynolds numbers is paramount. A DNS study based upon the immersed boundary method (IBM) on fluid flows through regular and random arrays of static spheres by Tang et al. (Tang et al., 2015) derived

$$F_D(\epsilon_f, Re_p) = \frac{10(1-\epsilon_f)}{\epsilon_f^2} + \epsilon_f^2(1 + 1.5\sqrt{\epsilon_f})$$
$$+ \left[0.11(1-\epsilon_f)(2-\epsilon_f) - \frac{0.00456}{\epsilon_f^4} + \left(0.169\epsilon_f + \frac{0.0644}{\epsilon_f^4}\right)Re_p^{-0.343}\right]Re_p. \tag{54}$$

Good agreement between the correlation of Tenneti et al. (Eq. (53)) and that of Tang et al. is observed at $Re_p = 50, 100$ (Tang et al., 2015). However, at larger $Re_p$, the expression of Tenneti et al. is less accurate and diverges from the DNS simulation data of Tang et al. In a study on the simulation of spherical particles in a Wurster fluidised bed, the expression of Tang et al. was tested against the Ergun equation in addition to other voidage correction correlations (Li et al., 2016). It is important to note that Eqs. (53) and (54) have been estimated for assemblies of static spheres. Similar to the Di Felice expression (Eqs. (50) and (51)), which has also been formulated for spheres, these expressions can be applied to instances of spherocylinders as an approximation. Unfortunately, expressions to correct for voidage effects in spherocylinders are not yet available in the literature. One way to address this is to formulate multi-particle hydrodynamic correlations using the DNS approach, as suggested in Section 3.4.2.

Expressions for the hydrodynamic forces acting on the particles account for momentum transfer from the fluid to the particle. According to Newton's third law of motion, a balancing force must be exerted on the fluid. In Eq. (27), $\mathbf{R}_{f,p}$ is the momentum exchange between the fluid phase and the discrete particle phase. For the drag force, the volumetric fluid-particle interaction force (Xu and Yu, 1997) can be calculated using

$$\mathbf{R}_{f,p} = -\frac{\sum_{p=1}^{N_p}\mathbf{F}_{p,D}}{V_{\text{cell}}} \tag{55}$$

where $p$ is the particle label, $N_p$ is the number of particles in the computational fluid cell, $\mathbf{F}_{p,D}$ is the drag force acting on particle $p$ due to the fluid, and $V_{\text{cell}}$ is the volume of a computational fluid cell. Similar expressions can be applied for fluid-induced lift force, hydrodynamic torque and other variables (Link et al., 2005).

### 4.3. Application of CFD-DEM to elongated particles

We now overview recent applications of CFD-DEM for the study of suspensions of elongated particles, specifically spherocylinders, in laboratory-scale fluidised beds. First, we summarise results pertaining to the study of spherocylinder dynamics in pseudo-2D fluidised beds (Mahajan et al., 2018). Simulation results are compared with the experiments of Mahajan et al. (2018). Thereafter, the relevance of lift and torque on the dynamics of elongated particles in a wider fluidised bed using CFD-DEM is considered (Mema et al., 2017, 2019). In addition, results from recent CFD-DEM studies on elongated particles are summarised and discussed.

### 4.3.1. Fluidisation of spherocylindrical particles: pseudo-2D approach

The behaviours exhibited by collections of non-spherical particles are crucially dependent on the fluidisation velocity. When the gasification velocity $U_0$ is a little larger than the minimum fluidization velocity $U_{mf}$, bubbles form near the distribution plate at the base of the reactor and move through voids between the suspended particles, while for larger velocities, circulation patterns develop where particles move up in the centre of the reactor and return to the base via the walls. For elongated particles, such macroscopic responses are likely to be influenced by particle orientations relative to the flow and their interaction with adjacent particles. In a real reactor consisting of many millions of particles, it is impossible to measure bed attributes such as local particle orientation or coordination number. To access this information in laboratory experiments, the fluidised bed requires some degree of simplification such as decreasing the particle number to O($10^4$–$10^5$) particles and changing the geometry to a pseudo-2D system, which allows for feasible optical tracking of individual particles, while at the same time preserving the integrity of a fluidisation process (Mahajan et al., 2017, 2018).

Although a laboratory pseudo-2D fluidised bed provides a plethora of observations and measurements, certain particle properties are difficult to measure. For example, Digital Image Analysis (DIA) can only decipher the orientation of particles at the front wall that are lying parallel to the wall. However, a CFD-DEM simulation of the same system can provide access to this supplementary information on particle orientation and other relevant attributes. A schematic of the setup for a CFD-DEM simulation is presented in Fig. 17. A key step in the development of any numerical model is validation of the model by comparing simulation output with equivalent laboratory measurements (Mahajan et al., 2018). Once validated, the numerical model can be used to study properties that are difficult to access in experiments. Hence, we have compared CFD-DEM simulations with our previous laboratory experiments of pseudo-2D fluidised beds comprising of spherocylindrical particles (Mahajan et al., 2018). The numerical study focuses on the implementation of various drag force models and
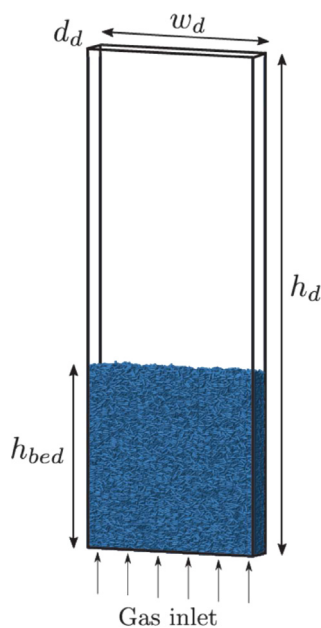
voidage calculation schemes. In particular, the drag model defined by Hölzer and Sommerfeld (2008) (Eq. (14)) is compared with the drag correlation derived from our DNS study. Voidage calculation schemes considered include those of Di Felice (1994), Tenneti et al. (2011), and Tang et al. (2015), which have been outlined in Section 4.2.4. Mahajan et al. (2018) did not yet consider the influence of lift or torque on particle dynamics. Two fluidised beds, one large and one small, were simulated and the superficial gas velocities varied from 0.2 m/s to 2.6 m/s.

We consider the comparison of pressure drop measurements from the simulations and experiments of Mahajan et al. (2018). As shown in Fig. 18, the case with the Hölzer and Sommerfeld drag model (Hölzer and Sommerfeld, 2008) and the Di Felice voidage expression (Di Felice, 1994) (HDF) under-predicts the pressure drop, particularly in the packed bed regime, and estimates a higher minimum fluidization velocity $U_{mf}$. This disparity is more than likely associated with the adaptation of the Hölzer and Sommerfeld single particle drag model for a multiparticle configuration. The cases with the Sanjeevi drag model with voidage corrections of Tang and Tenneti provide better correspondence between the simulations and the experiments, which is possibly due to the higher accuracy of these models for different Reynolds numbers. Recall that the Sanjeevi drag model has been derived specifically for flows where $Re \leqslant 2000$ in the vicinity of spherocylindrical particles (Sanjeevi et al., 2018) while the Hölzer and Sommerfeld drag model (Hölzer and Sommerfeld, 2008) has been derived using experimental and LBM results on spheres, plates, and cubes, and has been adapted for spherocylindrical particles in this study. Mahajan et al. (2018) also note differences in the bed height where the Hölzer and Sommerfeld drag model underestimates bed height, while the Sanjeevi drag model overestimates the bed height. The difference in both cases is more than likely due to the fact that the drag models do not accurately capture multiparticle effects (Mahajan et al., 2018).

Through DIA, it is possible to determine the probability density function of particle orientations of the particles (PDF($\alpha$)) that are visible through the front wall. Fig. 19(a) shows the particle orientations from experiments while Fig. 19(b) shows the particle orientations from CFD-DEM simulations. In the simulation results, it is clear that particles do not align with the flow at high gas flow velocities, which contrasts with experimental observations. In fact, the particles remain mainly horizontal, except at the highest velocities where a small peak in the PDF is observed at an orientation of $0°$. The lower figure of Fig. 19(b) shows that the central peak is a boundary effect, given the distribution for particle distances less than $2L_p$ from the side wall is the only distribution with a peak at $0°$. The differences between the experiments and the simulations is likely to be partly due to the absence of important hydrodynamic force contributions in the simulations. In the experiments, particles are subject to transverse lift, pitching torque, and rotational torque, none of which were included in the simulations. In particular, torque can aid particle rotation and thus its inclusion in CFD-DEM simulations could lead to a more accurate estimation of particle orientations as recorded in experiments.

### 4.3.2. Fluidisation of spherocylindrical particles: importance of lift and torque

The CFD-DEM study in the previous section explored the impact of specific drag correlations on the dynamics of spherocylinders in a fluidised bed reactor. However, this study did not take into account transverse lift and pitching torque. For an elongated particle in a dilute suspension, the lift force can exceed more than half the drag force acting on the particle, depending on Reynolds number, and thus greatly affect the particle trajectory. As outlined in Section 3.4.2, a number of drag and lift force coefficient correla-
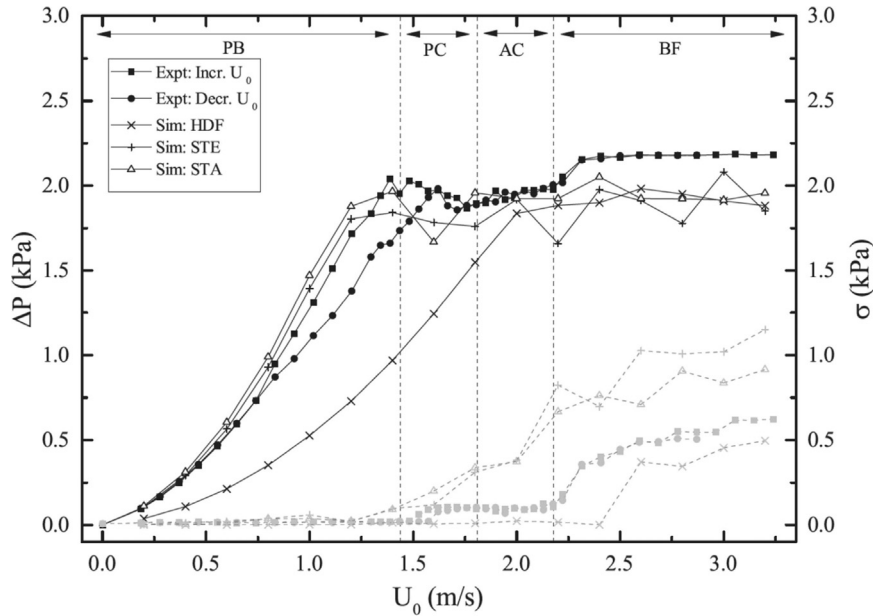


**Fig. 17.** Simulation representation of a pseudo-2D fluidised bed showing a packed bed representing the initial conditions for a simulation. $h_d$ is the reactor height, $h_{bed}$ is the initial height of the packed bed, $d_d$ is the depth of the reactor, and $w_d$ is the width of the reactor. Image from Mahajan et al. (2018). This configuration is similar to that of our experimental studies (Mahajan et al., 2017, 2018).

**Fig. 18.** Comparison of the pressure drop $\Delta P$ (black) and the standard deviation (grey) in the pressure drop $\sigma$ from pseudo-2D experiments and simulations for a fluidised bed. For the experiments, the pressure drop curves are plotted for cases of increasing and decreasing $U_0$. For the simulations, the pressure drop curves represent different cases of the drag model and voidage scheme where HDF is Hölzer and Sommerfeld drag model (Hölzer and Sommerfeld, 2008) with the Di Felice voidage expression (Di Felice, 1994), STE is the Sanjeevi drag model (Sanjeevi et al., 2018) with the Tenneti model for voidage effects (Tenneti et al., 2011), and STA is the Sanjeevi drag model with the Tang model for voidage effects (Tang et al., 2015). For the experimental data set, PB is Packed Bed, PC is Passive Channelling, AC is Active Channelling, and BF is Bubbling Fluidisation. Image from Mahajan et al. (2018).

tions are available in the literature, although there are fewer torque coefficient correlations (Sanjeevi et al., 2018; Zastawny et al., 2012). Nonetheless, the effects of lift force and pitching torque on particle dynamics in dense suspensions are poorly understood.

To address these issues, we have also investigated, using CFD-DEM simulations, the influence on particle dynamics of varying lift and torque conditions experienced by spherocylinders with an aspect ratio 4 in a 3D fluidised bed (Mema et al., 2019). We employed the correlation functions from Sanjeevi et al. (2018) for the drag, lift, and pitching torque coefficients acting on an isolated spherocylinder particle. Lift and torque were calculated using the expressions given in Section 3.4.1. In this study, we did not consider two-way coupling for the pitching torque. In other words, we implemented one-way coupling for the pitching torque where the influence of the flow on the particles is considered.

First, the effect of including different types of hydrodynamic forces on the average particle velocity parallel to the direction of gravity $v_z$ was examined at three different positions. These locations are roughly midway along the $y$-axis. The lowest position, at $z = 0.0675$ m is closest to the flow inlet, while $z = 0.3075$ m is the position furthest from the flow inlet and a region characterised by dilute particle conditions. Note that the temporally averaged velocity $v_z$ is not the same as the average mass flux, given that there may be strong correlations between the local solid volume fraction and particle velocity, which has been demonstrated for spherocylindrical particles in a pseudo-2D fluidised bed (Mahajan et al., 2018). The inclusion of lift has a significant effect on $v_z$, as shown in Fig. 20. At $z = 0.0675$ m, in comparison to the case with drag only, lift leads to an increase in $v_z$ midway along $x$-axis. Similar changes in $v_z$ are observed for the other positions, however the differences in the trends are not as pronounced at $z = 0.3075$ m, which is due to the dilute particle conditions at the higher $z$-axis position. Conversely, the inclusion of torque has a negligible effect on $v_z$ in this system. Even for the case with all hydrodynamic forces, there is no significant change in $v_z$ relative to the case with drag and lift forces only.

Including or excluding different types of hydrodynamic forces also affects the particle orientations in the fluidised bed. Particle orientation relative to the $x$-, $y$-, and $z$-axis is defined by the unit vector consisting of the components $u_x, u_y$, and $u_z$ respectively. A particle is deemed to be fully aligned with the $z$-axis when $u_z \pm 1$ and perpendicular to the flow when $u_z = 0$. Fig. 21 shows the distribution $f(u_z)$ of $u_z$ values in the fluidised bed. It demonstrates that torque critically affects the orientation of particles relative to the $z$-axis. The case with only drag force is almost indiscernible from the case with drag and lift forces, indicating that lift has a negligible effect on particle orientation in this system. However, inclusion of torque with drag leads to a decrease in the number of particles aligned with the $z$-axis and an increase in the number of particles approximately perpendicular to the flow. The addition of lift force along with drag and torque does not appreciably affect this trend.

To ascertain the preferred particle orientation in specific parts i.e. grid cells, of the reactor, the particle orientation tensor **S** is evaluated using

$$\mathbf{S} = \begin{bmatrix} \langle u_x^2 \rangle & \langle u_x u_y \rangle & \langle u_x u_z \rangle \\ \langle u_y u_x \rangle & \langle u_y^2 \rangle & \langle u_y u_z \rangle \\ \langle u_z u_x \rangle & \langle u_z u_y \rangle & \langle u_z^2 \rangle \end{bmatrix}. \tag{56}$$

where the angular brackets indicate averaging over the particles in the cell of interest and over time. The preferred alignment of the particles is determined by the diagonal components of **S**. Firstly, if one of the diagonal components is substantially greater than the other two diagonal components, the particles are deemed to be preferably aligned with that axis. Secondly, a particle is judged to be randomly orientated if the difference between any of the diagonal components is less than 0.1. Fig. 22 shows the preferred particle alignment on the $x$-$z$ plane for a cross section along the $y$-axis for differing hydrodynamic force conditions. To identify the preferred particle orientation in the grid cells, a colour scheme has been applied such that a blue cell represents alignment with the $x$-axis,
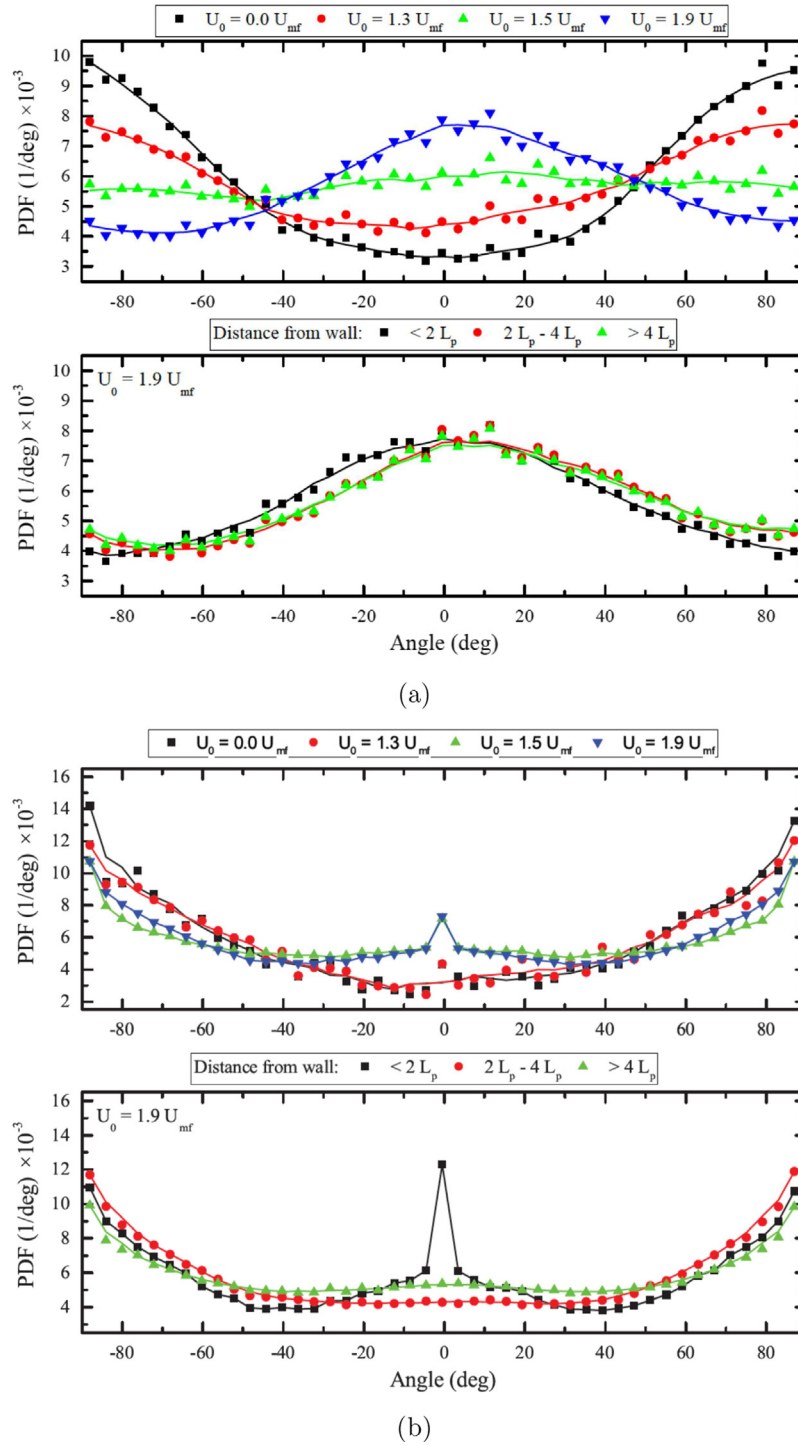
**Fig. 19.** Probability density function (PDF) of particle orientations from experiments (a) and simulations (b), based on particles that are visible through the front wall. The upper figure shows the distribution of particle orientations for four different gas velocities that correspond to the four different fluidisation regimes. The lower figure shows the distribution of particle orientations at different positions relative to the side walls of the reactor for the case $U_0 = 1.9U_{mf}$. Angles of $-90°$ and $90°$ represent particles that are horizontal and an angle of $0°$ is a particle that is vertically orientated. The length of the particles $L_p = 12$ mm. Images from Mahajan et al. (2018).

a green cell represents alignment with the $y$-axis, and a red cell represents alignment with the $z$-axis. A cyan-filled cell represents a cell with no preferred alignment. Fig. 22(b) shows the case with the addition of lift where particle orientation is observed to become more random in the central section of the reactor in comparison to the case with drag force only (Fig. 22(a)). However, when torque is considered (Fig. 22(c)), a significant change in the orientation of

particles is observed in agreement with variations in $f_p(u_z)$ (Fig. 21). With torque, particles are either randomly orientated or perpendicular to the $z$-axis in the central domain of the reactor. In addition, the alignment of particles adjacent to the walls also changes. For the case with lift, particles next to the walls are aligned with the $z$-axis and with torque, particles are aligned with the $y$-axis. The case with all forces shown in Fig. 22(d)) is similar to the
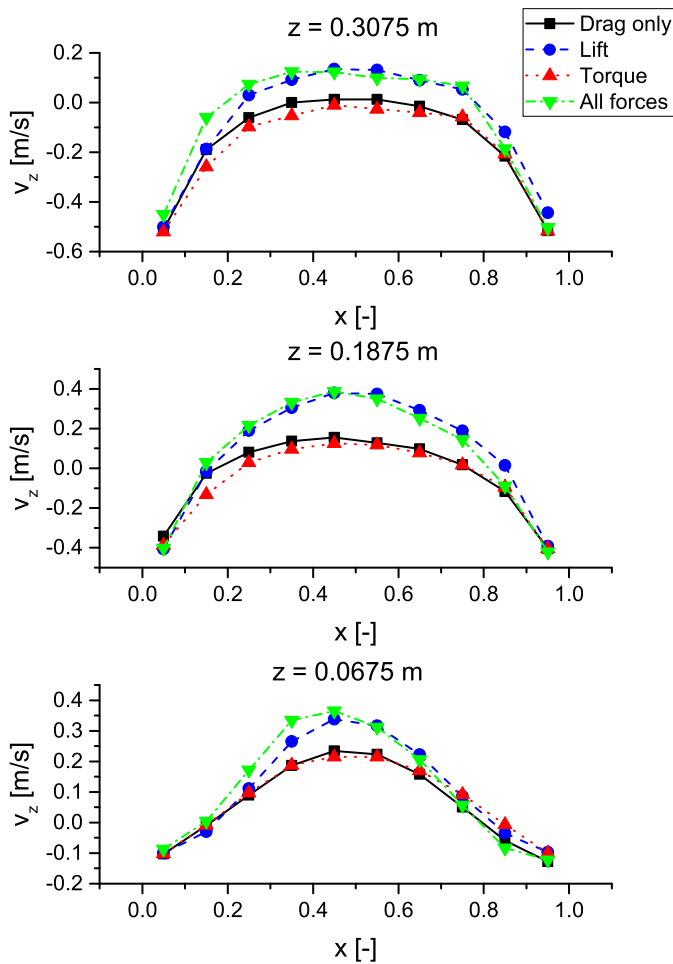
**Fig. 20.** Comparison of the temporally-averaged $v_z$ along the *x*-axis for various heights in a fluidised bed for different hydrodynamic conditions: Drag only (black), lift force and drag force (blue), torque and drag force (red), and a case with all hydrodynamic forces (green). *x* is the position normalised by the length of reactor along the *x*-axis ($L_x = 0.15$ m). Based on image from Mema et al. (2019). (For interpretation of the references to colour in this figure legend, the reader is referred to the web version of this article.)

case with torque and drag force (Fig. 22(c)), confirming the observation in Fig. 21 that the inclusion of lift does not lead to large differences in particle orientation.

### 4.4. Comparison with other CFD-DEM studies on fluidised beds

In the previous sections, we presented CFD-DEM results related to the fluidisation of spherocylinders, focusing on the effect of bed geometry (Mahajan et al., 2017, 2018) and hydrodynamic force conditions (Mema et al., 2017, 2019). We now consider briefly the findings of a number of other relevant CFD-DEM studies on fluidised non-spherical particles.

Prompted by the use of variable-shaped particles in processes such as catalysis and pyrolysis, Hilton et al. (2010) studied the fluidisation of a number of particle shapes such as spheres, cuboids, and ellipsoids. Drag forces were described by the Hölzer and Sommerfeld expression (Hölzer and Sommerfeld, 2008) while voidage effects were taken into account using the Di Felice correction (Di Felice, 1994) After validating the numerical approach using spherical particles and comparison with the work of Tsuji et al. (1993), Hilton et al. showed a larger pressure drop and lower fluidisation velocity for non-spherical particles in comparison to spherical particles due to a decrease in the porosity of the bed. Particles with varying shapes and aspect ratios can also affect mixing and particle orientations in bidisperse packings in a fluidised bed, as demonstrated by Oschmann et al. (2014). Particles were subject to the same drag force condition as Hilton et al. (2010). Simulations revealed that mixing and the maximum bed height depend on particle shape and that a large gas velocity increases mixing for complex shapes, while a low gas velocity leads to incomplete mixing. Elongated particles were shown to exhibit slower mixing with increasing elongation and these particles were also shown to align parallel to the rigid walls. We have also recovered this alignment behaviour in our CFD-DEM simulations of large 3D reactors (Fig. 22). However, the work of Oschmann et al. (2014) did not include lift forces or hydrodynamic torque, which we have shown to significantly affect particle alignment (Fig. 22) (Mema et al., 2019).

In a study combining experimental and numerical methods, Vollmari et al. (2016) explored the fluidisation of a number of Geldart D particle shapes including spheres, cylinders, cubes, plates,
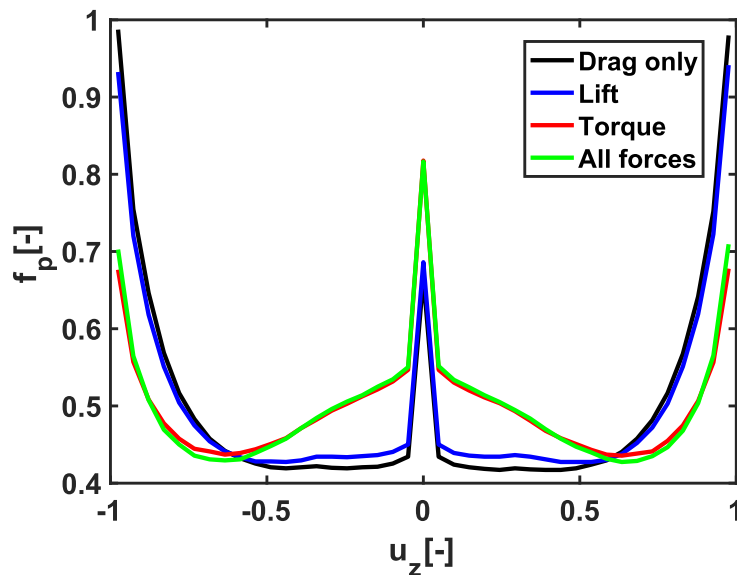


**Fig. 21.** Variation of $f_p(u_z)$ demonstrating the preferred particle orientations for differing hydrodynamic force conditions. Image from Mema et al. (2019).
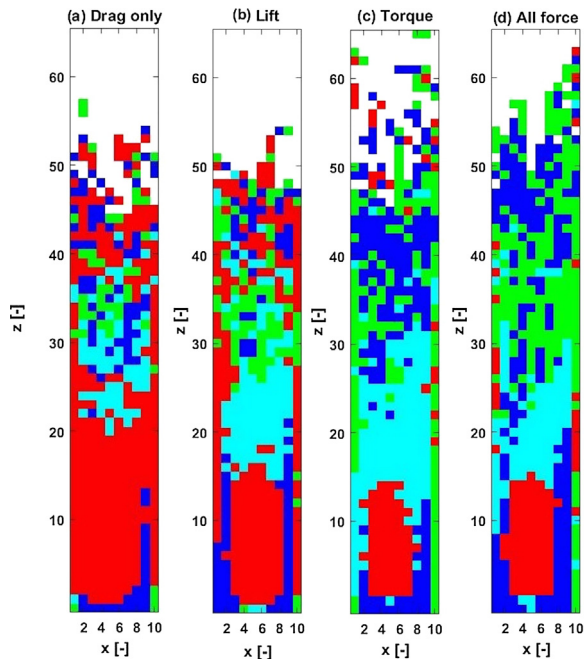
**Fig. 22.** Preferred particle orientations for differing hydrodynamic force conditions: (a) drag only, (b) lift force and drag force, (c) torque and drag force, (d) all hydrodynamic forces. The number of grid cells along the x-axis and z-axis are 10 and 66 respectively. Blue is preferred alignment with the x-axis, green is preferred alignment with the y-axis, red is preferred alignment with the z-axis. Cyan means no preferred alignment. Image from Mema et al. (2019). (For interpretation of the references to colour in this figure legend, the reader is referred to the web version of this article.)

and highly elongated variants of non-spherical particles. All particle types were subject to drag forces as described by Hölzer and Sommerfeld with multiparticle effects accounted for using the Di Felice approximation. To measure particle orientation, a DIA approach similar to that used in the experiments of Mahajan et al. (2018) on pseudo-2D beds was utilised. In terms of shape, the closest particle in their study to a spherocylinder was a flat-ended elongated cylinder. The simulations accurately captured particle orientation, particularly at high gasification velocities, where particles tend to align themselves with the direction of flow

(Fig. 23). Similar particle shapes including elongated particles have also been studied in 3D fluidised beds (Kruggel-Emden and Vollmari, 2016) where a number of particle-shape dependent flow regimes were identified.

Similar to the work presented earlier in this section, there have been CFD-DEM studies that have focused solely on the fluidisation of elongated particles. Nan et al. (2016) presented CFD-DEM simulations on the fluidisation of rod-like particles subject to hydrodynamic drag only, using the multiparticle coefficient of Rong et al. (Eq. (52)) for multiparticle effects. A multi-sphere model was used to represent rods, which is based on the model of Favier et al. (1999). Variation of the particle aspect ratio and bed porosity was shown to affect the bed permeability and coordination number (Fig. 24). The degree of horizontal particle alignment decreased during fluidisation of the bed (Fig. 24). In a similar CFD-DEM study, Ma et al. (2017) investigated rod-like particles in a pseudo-2D fluidised bed where the particles were described by the standard formula for a super-ellipsoid (Eq. (43)). Particles were subject only to a drag force described by the Hölzer and Sommerfeld expression (Hölzer and Sommerfeld, 2008) and multiparticle effects estimated using the Di Felice approximation. Both pressure drop and particle orientation were shown to depend on particle aspect ratio, with particles with the largest aspect ratio subject to greater wall effects.

CFD-DEM has also been applied to study ellipsoidal particles subject to fluidisation (Zhou et al., 2011; Jieqing et al., 2016; Gan et al., 2016). Zhou et al. (2011) considered ellipsoidal particles subject only to hydrodynamic drag, with torque excluded on the argument that the rotation of particles due to the fluid can be ignored (Hilton et al., 2010). As shown above, this assumption may have been a bit premature. The effect of neighbouring particles on the drag force was calculated using the Di Felice expression and contacts between particles calculated using the geometric potential algorithm (Ting, 1992; Džiugys and Peters, 2001). They demonstrated that particle shape, i.e. prolate or oblate, can affect bed permeability, that flow structures consisting of ellipsoids are more correlated than structures in flows of spheres, that the coordination number increases as particle aspect ratio increases, and that contact forces in packings of spheres are larger than for ellipsoids. While these results provide interesting insight on the fluidisation of ellipsoids, we note that the algorithm lacks some key details such as a custom particle-particle force model for ellipsoids and the inclusion of other hydrodynamical forces other than drag.
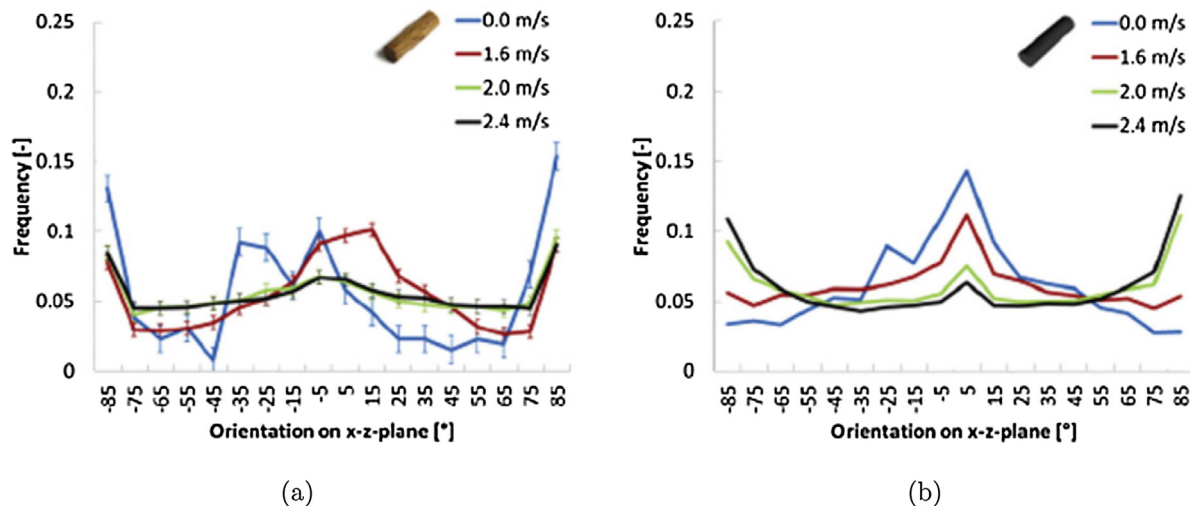


**Fig. 23.** Distribution of the orientation of elongated cylinders (4 mm × 14 mm) along the x-z plane from (a) CFD-DEM simulations and (b) experiments. Best correspondence between simulations and experiments occurs at high gasification velocities when particles align with the direction of flow. Images from Vollmari et al. (2016).
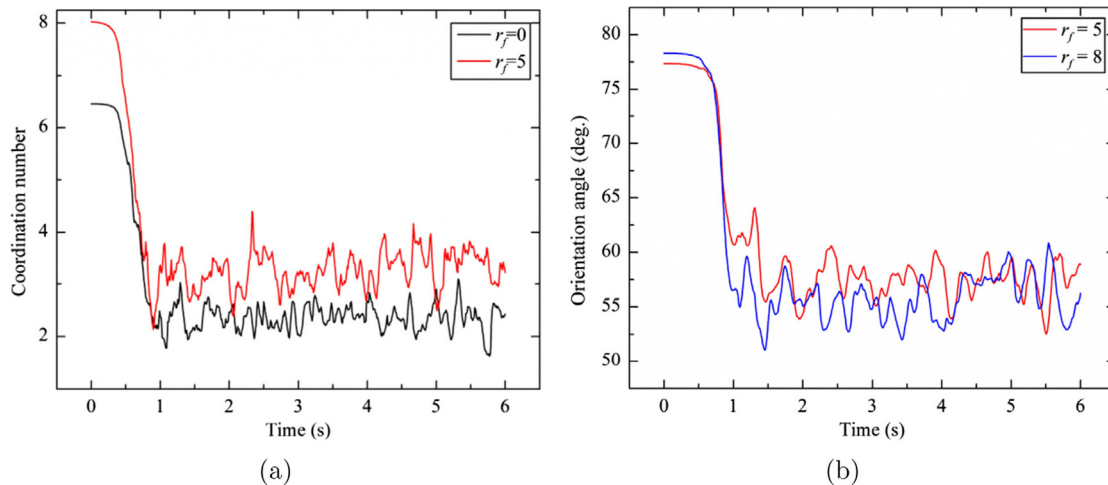
**Fig. 24.** (a) Temporal fluctuations in the average coordination number in a fluidised bed with spheres ($r_f = 0$) and spherocylinders ($r_f = 0$). (b) Temporal fluctuations in the particle orientation in a fluidised bed with two different spherocylinders ($r_f = 5$ and $r_f = 8$). The superficial gas velocity is twice the minimum fluidisation velocity. Images from Nan et al. (2016).

The studies outlined earlier apply to the fluidisation of Geldart D non-spherical particles. CFD-DEM simulations of both Geldart A particles ($25\,\mu m \leqslant d_p \leqslant 100\,\mu m$) and Geldart B particles ($500\,\mu m \leqslant d_p \leqslant 1000\,\mu m$) in fluidised beds have been examined by Jieqing et al. (2016). Particles of different shapes such as spheres and ellipsoids were subject only to a drag force that did not account for multiparticle effects. A van der Waals attractive force was also included to facilitate the formation of agglomerates. A decrease in ellipsoid size led to an increase in the size of particle agglomerates while the minimum fluidisation velocity increased exponentially with an increase in particle size. In addition, larger fluctuations in pressure drop were observed for increased particle size but little difference was observed for different particle types. The same authors have also extended the CFD-DEM approach to study the dynamics and heat transfer of Geldart A ellipsoidal-like particles, ranging from disk-type to cylinder-type particles (Gan et al., 2016). Particles were subject to drag forces described by the Holzer and Sommerfeld expression and multiparticle effects were approximated using the Di Felice correction, while lift and torque were not included. An increased aspect ratio of the particles was shown to affect the effective thermal conductivity due to an increase in particle coordination number and contact area. In addition, ellipsoids have a higher conductive heat transfer rate than spheres, but in a fluidised bed, spheres are easier to heat (Gan et al., 2016). Adhesive nanoparticle agglomerates have also been studied in a fluidised bed by Liu et al. (2016).

Although not the primary focus of this paper, we briefly consider the use of CFD-DEM for the study of binary mixtures. A CFD-DEM study by Ma et al. investigated the fluidisation of binary particulate mixtures subject only to drag force in a fluidised bed (Ma and Zhao, 2018). The binary mixture consisted of spherical particles and rod-like particles that represent the inert bed material i.e. sand, and the biomass feedstock, respectively, with both particles described as super-ellipsoids. In a fluidised bed reactor, the inert bed material facilitates the fluidisation of the biomass particles, thus CFD-DEM simulations can provide valuable insight with regards to particle dynamics that could be relevant for apparatus design and process optimisation. The simulations revealed that the minimum fluidisation velocity increased with increasing volume fraction of rod-like particles while mixing and particle coordination numbers were dependent on gas velocity and rod-like particle volume fraction. The orientation of rod-like particles differed considerably in mixtures in comparison to systems of just

rod-like particles. Results on particle orientation from this CFD-DEM study agree with an in-depth experimental study on the fluidisation of mixtures of spherical and cylindrical particles in a pseudo-2D fluidised bed by Boer et al. (2018). In these experiments, particle orientation was determined using Digital Image Analysis (DIA) of images of particle dynamics taken with a CCD camera, with the long axis of the cylindrical particles shown to align with the direction of the fluid flow. In addition, particle segregation was shown to develop in the non-bubbling flow regime. The DIA technique can only accurately analyse particle orientations for particles adjacent to the front wall of the bed, unlike the CFD-DEM simulations of Ma and Zhao (2018) where particle orientations could be isolated in any domain of the reactor.

While these CFD-DEM studies consider differing implementations of drag and associated multiparticle effects, none of the studies consider the influence of lift and torque on the dynamics of elongated particles such as ellipsoids or spherocylinders. Nevertheless, our preliminary CFD-DEM study on the fluidisation of spherocylinders has demonstrated that both lift and torque can appreciably affect particle dynamics (Mema et al., 2019). However, we have only considered lift and torque correlation functions for an isolated particle and did not yet consider the multiparticle effects on these correlations. Our work partially addresses the shortfall of studies on the importance of lift and torque on elongated particles. When multiparticle correlation functions become available in the literature, their implementation in future CFD-DEM investigations will represent a natural progression in terms of advancing existing algorithms for the accurate simulation of fluidisation apparatus.

### 4.5. Stress correlation calculations

In addition to simulating fluidised bed dynamics, the CFD-DEM algorithm for spherocylinders can be used for the calculation of particle stress correlations that can be used in the definition of a constitutive model for industrial scale models. This approach is principally motivated by the lack of applicability of Kinetic Theory of Granular Flow (KTGF) to dense flows of elongated particles since KTGF has been defined for dilute or moderately dense configurations of spheres. Rather than extracting stress expressions from a large-scale fluidised bed, a simplified system without the interstitial fluid and consisting of a collection of elongated particles subject to shear deformation can be considered (Guo et al., 2012,

2013; Berzi et al., 2016). The shearing boundaries can be implemented as either solid boundaries or as Lees-Edwards boundaries (Lees and Edwards, 1972). Such an approach allows for exact control over the particle solid volume fraction in the shear cell while algorithms can be applied to control the initial arrangement of dense particle packings (Guo et al., 2012). The particle-phase stress tensor can be based on the summation of two components. First, a kinetic component $\boldsymbol{\sigma}_k$ (Campbell and Gong, 1986) associated with momentum transfer between particles is calculated with

$$\boldsymbol{\sigma}_k = m\langle\mathbf{v}'\mathbf{v}'\rangle \tag{57}$$

where $m$ is the particle mass, $\langle\rangle$ is an average over time and space, and $\mathbf{v}' = \mathbf{v}_i - \langle\mathbf{v}\rangle$ is the fluctuating velocity. Second, a particle contact or collisional component $\boldsymbol{\sigma}_c$ is calculated using

$$\boldsymbol{\sigma}_c = \langle\mathbf{F}_{ij}\mathbf{l}_{ij}\rangle \tag{58}$$

where $\mathbf{F}_{ij}$ is the force between the particles $i$ and $j$, and $\mathbf{l}_{ij}$ is the vector from the centre of mass of $i$ to the centre of mass of $j$. Dense configurations are typically dominated by prolonged contacts between neighbouring particles, and thus the stress tensor is dominated by $\boldsymbol{\sigma}_c$ (Guo et al., 2012, 2013), while in dilute systems, where long-lasting particle contacts are less prevalent, the stress tensor is mediated by $\boldsymbol{\sigma}_k$. Previous studies have investigated the effect of volume fraction, aspect ratio, coefficient of restitution, interparticle friction, and Young's modulus on the components of the solid phase stress tensor for deformed packings of elongated particles (Guo et al., 2012, 2013; Berzi et al., 2016).

The aforementioned approach allows for the calculation of solid phase stress tensors. However, it is specifically applied in a shear cell where particle deformation subject to shear and in the absence of a fluid can be precisely regulated. Such an idealised system is not completely representative of the deformations that particles experience in a fluidised bed environment. In a recent CFD-DEM study, Gu et al. (2019) measured the particle phase stress and granular temperature of spherical particles subject to fluidisation in a fully-periodic bed geometry. Critically, this study accounted for the effects of the interstitial fluid and a fluidised bed system on the stress tensor. First, the study investigated the fluidisation of non-cohesive particles and found that simulation results corresponded well with constitutive expressions from KTGF, thus validating the approach. Gu et al. (2019) then investigated the fluidisation of cohesive particles and used the numerical results to formulate a constitutive theory for cohesive particles. The calculation of stress tensors for packings of elongated particles in a shear cell using DEM (Guo et al., 2012, 2013; Berzi et al., 2016) and for cohesive spherical particles in a fully-periodic fluidised bed (Gu et al., 2019) are both intermediate steps towards the definition of constitutive relations for elongated particles in a fluidised bed geometry. For the case of spherocylindrical particles, a first study should focus on particles subject to shear deformation in a shear cell for a range of volume fractions. Thereafter, a CFD-DEM study of a fluidised spherocylinders in a periodic fluidised bed could be used to revise relations for bulk dynamics. Finally, a fluidised bed with boundaries could be considered to explore the influence of the boundaries on the constitutive relations. Crucially, a CFD-DEM approach is the most appropriate method for the calculation of stress closures that take into account the effect of the fluid.

## 5. Macroscopic simulations

For the prediction of truly large-scale gas-solid flows, it is not feasible to resolve every individual particle collision due to the high number of calculations associated with large packings of particles. Instead, the effect of particle collisions can be modelled in an averaged approach, with an appropriate particle collision closure

relation. The two-fluid model (TFM) (Gidaspow, 1994) and multiphase particle-in-cell (MPPIC) (Snider, 2001; Andrews and O'Rourke, 1996) methods are two common approaches to evaluate interactions in systems with large numbers of particles. In TFM, both the gas and solids phase are treated as fully interpenetrating continua. The Kinetic Theory of Granular Flow (KTGF) is used to describe particle-particle interactions on a fundamental level. In the most common version of KTGF, the particle-particle collisions are described by a single parameter collision model (Jenkins and Savage, 1983). The theory assumes the particles to be perfectly smooth, and particle velocity changes in the tangential impact direction are neglected. Only the normal impact and rebound velocities of two colliding particles are taken into account using the coefficient of normal restitution. Advanced versions of KTGF also include the effects of tangential friction for spheres that gives rise to particle rotation as well as sliding and sticking collisions, as previously implemented in TFM by one of the authors of this paper (Yang et al., 2016,). This implementation of KTGF was subsequently validated via comparison with magnetic particle tracking experiments in 3D fluidised beds (Yang et al., 2017). TFM is fast, but depends on theoretical expressions for the solid stress, usually based on KTGF. In KTGF, far-reaching assumptions are made to make the theoretical calculations tractable, such as particle sphericity and isotropy, molecular chaos (no pre-collisional velocity correlations), and binary interactions. However, it is known that correlations in the velocities build up in denser flows (Radl and Sundaresan, 2014), and multiple simultaneous particle contacts can no longer be ignored. Most importantly, for non-spherical particles all distribution functions become non-isotropic and the standard kinetic theory can no longer be applied. A new kinetic theory should be proposed for non-spherical particles that describes stress transmission through the continuum particle phase. The granular temperature, which is the kinetic energy per unit mass associated with the fluctuating motion of non-spherical particles relative to the local average velocity of the particle phase, is a topic of current research. Similar to spherical particles, the particle phase stress for non-spherical particles can be expressed in terms of local particle volume fraction, granular temperature, local rate of deformation, and particle orientation. Despite the importance of non-spherical particles in industry, no efforts have been made thus far to treat non-spherical particles as a continuum phase, and thus remains a prevailing challenge for accurate simulations.

Another approach to overcome limitations on the number of particles in a simulation, is the parcels of point particles approach developed by Andrews and O'Rourke (1996). In the so-called multiphase particle-in-cell (MP-PIC) method, the fluid phase is treated as a continuum (Eulerian) and the particles are traced in a Lagrangian fashion, including a parcel approach where each simulated particle represents a large collection of real particles. Each parcel follows Newton's equations of motion, where inter-phase momentum transfer is evaluated by mapping and interpolating quantities back and forth between parcel locations and the Eulerian grid for the fluid. Particle-particle collisions in MP-PIC are not fully resolved and instead derived via gradients in particle stresses. In most commonly applied MP-PIC approaches, the particle stress is simply approximated by the (scalar) particle pressure, which for spherical particles at high solids volume fraction is given by a relation introduced by Harris and Crighton (1994). Particle stress gradients, which are difficult to calculate on the level of an individual particle, are calculated as a gradient on the Eulerian grid and then interpolated to discrete particles. The point particle and parcel approach is explained in the literature only for spherical particles (Harris and Crighton, 1994). For non-spherical particles no such approach is discussed. The principal difficulties lie in the representation as point particles, where additional degrees of freedom should be introduced for non-spherical particles. For example, an

elongated particle could be represented by its centre of mass location and an orientation vector. The distribution of centre of mass positions leads to the Eulerian solids volume fraction field. Similarly, we can imagine the distribution of the orientation vectors leads to an Eulerian order tensor field. The order tensor field and solid volume fraction fields, and their gradient, at the location of the particle can then be used to determine the fluid-particle drag, lift, and torque, as well as the (effective) forces on the particles due to particle-particle interactions.

As outlined, MP-PIC particle collisions are not fully resolved but effectively taken into account using the solid stress, and possibly also collisional dissipation rate and granular conductivity. Correlations for particle stresses for spherical particles are available in the literature (Lu et al., 2017), but no such stress relations have been defined for non-spherical particles. In fact, even for spherical particles, particle stress models are not well developed or validated. The particles stress for non-spherical particles not only depends on the particle volume fraction and granular temperature, but also on the orientation of particles. As a consequence, the constitutive equations for particle stress are no longer characterised simply by shear and bulk viscosity coefficients, but will also contain terms that couple the solids rate of deformation and rate of rotation fields to the order tensor (Sagis and van der Linden, 2001; Sagis et al., 2001). The coefficients of these constitutive equations can be obtained from CFD-DEM simulations. However, the main challenge is to obtain such expressions when the particle volume fraction becomes sufficiently large such that interactions between the non-spherical particles become prevalent. When non-spherical particles are aligned, the number of particle collisions is not the same in every direction, leading to strong anisotropy in the granular temperature. Anisotropies may become larger when the deformation rates are larger and influenced by the angles between the average particle orientation and the principle axes of the deformation or rotation flow. Therefore, the expression for particle-phase stresses for non-spherical particles cannot be generalised for particles of different shapes. However, CFD-DEM studies can aid in the derivation and validation of constitutive equations for a specific particle shape. We expect that viscous particle stresses, which are a function of granular temperature, solids volume fraction, and particle orientation, are dominant for dense granular flows of elongated particles. Viscous stresses are typically ignored in classical MP-PIC models as they are assumed to have little influence. However, viscous particle stresses represent frictional effects between particles by mutual collisions, which are expected to be very important for elongated particles at high volume fraction. The fluctuating components of the non-spherical particle velocities need proper consideration for the calculation of granular temperature, which for non-spherical particles is computable for dilute flows, but still remains a challenge for dense phase flows. Accurate information on granular temperature in dense regions is necessary for the development of MP-PIC, which can also be extracted from extensive CFD-DEM simulations.

Continuum and discrete parcel approaches on coarser computational grids facilitate more time efficient large-scale simulations. Such coarse-grid simulations can resolve large-scale behaviour, but fail to capture small-scale heterogeneous flow structures. Thus, fine grid simulations are required to capture these small-scale heterogeneities in fluidised beds (Wang et al., 2009; Andrews et al., 2005). For a system of spherical particles, Benyahia and Sundaresan (2012) demonstrated that continuum and MP-PIC approaches yield approximately homogeneous flows when coarse grids are employed. In addition, when the grid is refined, both approaches produce similar heterogeneous flow structures with essentially the same domain average slip velocity. Therefore, simulations with highly resolved grids and reduced computational costs are required for industrial applications. To overcome this problem, the effect of unresolved heterogeneous structures can be described by sub-grid modelling (Agrawal et al., 2001; Wang and Li, 2007; Ozel et al., 2013). Sub-grid and filtered models for the continuum approach can be applied in the MP-PIC approach (Benyahia and Sundaresan, 2012). To capture heterogeneous and microscopic structures within coarse-grid models, filtered constitutive relations such as for drag force, lift force, torque, and particle stresses are imperative. These sub-grid constitutive relations can be estimated by filtering fine grid TFM or CFD-DEM simulations with these relations depending significantly on the filter length and grid size (Schneiderbauer et al., 2013). For the case of elongated particles such as spherocylinders, the sub-grid heterogeneity effects may be more pronounced given that elongated particles can experience a greater frequency of inelastic interactions.

The development of coarse-grid models for elongated particles can be used in TFM and MP-PIC simulations. Filtered sub-grid constitutive models for elongated particles can be derived in similar fashion to models for spherical particles. However, unlike spherical particles, elongated particles require effective filtered drag, lift, and torque. CFD-DEM simulations can provide filtered frictional solid stresses, which, for elongated particles, depend upon filter length, particle orientation, and their packing arrangement. Constitutive frictional solid stresses from CFD-DEM for MP-PIC models can be further upgraded to obtain filtered frictional stresses through variation of filter lengths. Highly resolved TFM and MP-PIC simulations for non-spherical particles that account for frictional solid stresses in dense packings can also be used develop filtered frictional solid stresses. However, filtered frictional stresses may become important even at significantly smaller solids volume fractions. Therefore, CFD-DEM is proposed for the derivation of a filtered solid stress model. The difference in obtaining filtered quantitates from CFD-DEM and fine grid Euler-Euler simulations for spherical particles has been discussed by Ozel et al. (2016). Similar differences can be scaled for non-spherical particles in relation to torque and lift forces.

## 6. Conclusions

In this paper, we have presented the algorithms required to implement a multiscale numerical investigation of multiphase flows consisting of elongated particles in fluidised bed reactors. A multiscale approach is necessary due to the large range of length scales in fluidised beds, whereby macrometre-size flow structures in industrial apparatus emerge as a result of particle interactions at the millimetre scale. The multiscale approach consists of algorithms at three length scales; namely the particle scale, the laboratory scale, and the industrial scale.

First, the lattice Boltzmann method (LBM), which is a DNS approach and capable of accurately resolving flow and transport details such as hydrodynamic forces at the particle scale, was overviewed (Section 3). We outlined the expressions central to the algorithm and considerations with regards to implementing boundary conditions and contending with mass leakage issues. Thereafter, results from previous LBM studies of stationary elongated particles, such as spherocylinders and ellipsoids, were presented. Drag, lift, and torque correlations for various elongated particles in both steady and unsteady flows derived from our LBM studies were compared with those from other DNS investigations. Variations in the hydrodynamic forces were shown to be dependent on particle orientation, Reynolds number, and, crucially, particle shape. The correlations presented here relate to the forces acting on an isolated particle in a flow field. In reality, during fluidisation, particles will regularly collide with adjacent particles and be located in dense particle regions. Multiparticle correlation functions are logically required to properly describe

the hydrodynamic forces experienced by particles in an evolving fluidisation process. In addition, it would be pertinent to study particle mobility effects for single particle and multiparticle packings on the resulting hydrodynamic forces.

As the primary focus in this paper has been the hydrodynamic forces experienced by elongated particles, studies on the heat transfer between phases were not discussed. Details on heat transfer implementations for LBM and other DNS approaches for both spherical and elongated particles are available in the literature (Deen et al., 2014; Ke et al., 2018,). Results from a study on the effect of a nearby rigid boundary on the hydrodynamics experienced by 2D elongated particles with varying orientations and particle Reynolds number were also outlined. While there are a number of DNS studies have derived correlations for isolated elongated particles, there is a lack of studies on 3D non-spherical particles adjacent to boundaries. In fluidised bed reactors and other apparatus that manipulate multiphase flows, interactions with wall boundaries are inevitable, which motivates the potential for further studies to derive hydrodynamic correlation functions.

The second algorithm presented was the coupled CFD-DEM approach (Section 4). The CFD component of the algorithm solves the fluid phase between the solid particle phase, while DEM handles the identification of particle contacts and the subsequent calculation of contact forces. Collision detection schemes for ellipsoidal and spherocylindrical particle contacts were described and schemes for void fraction calculation were outlined. The hydrodynamic forces experienced by elongated particles can be calculated using the correlation functions defined in the DNS studies. However, these correlations typically apply to isolated particles and are best suited for dilute regions of a fluidised bed reactor i.e. where the solid fraction $\epsilon_s < 0.2$. The influence of neighbouring particles on the drag force can be estimated using a number of approximations based on $\epsilon_s$ (Di Felice, 1994; Rong et al., 2013; Tenneti et al., 2011; Tang et al., 2015). Similar corrections for hydrodynamic lift and torque are currently not available, although recent studies suggest that the drag, lift, and torque experienced by elongated particles in dense configurations have a similar trend to the hydrodynamic forces on an isolated particle (He and Tafti, 2018). CFD-DEM results from our studies on the dynamics of spherocylinders in a pseudo-2D (Mahajan et al., 2018) and 3D fluidised bed reactors (Mema et al., 2019) were summarised. A discussion on comparable CFD-DEM studies was also provided, with the significant observation that no studies besides the work of Mema et al. (2017, 2019) consider the influence of lift and torque on elongated particle dynamics. This may be due to the lack of multiparticle correlations for hydrodynamic lift and torque. While the work of Mema et al. (2019) demonstrates that torque has an appreciable effect on particle alignment, this needs further validation. Nevertheless, the absence of detailed studies on lift and torque needs to be addressed, given the extensive use of elongated particles in the bioenergy industry and the lack of understanding as to how particle geometry affects hydrodynamics, thermodynamics, chemical reactions, and the design of fluidisation processes.

In Section 5, coarse-grained methods such as the two-fluid model (TFM) and the multi-phase particle-in-cell (MP-PIC) were briefly overviewed. These models are highly suited for the study of dilute to semi-dilute flows consisting of spherical particles, given that the solid stress expressions have been derived from the Kinetic Theory of Granular Flow (KTGF). Neither algorithm is currently suited for the simulation of dense multiphase flows involving elongated particles where velocity correlations are dominant and multiple particle collisions are frequent. Thus, it is important to establish accurate hydrodynamic and rheological descriptions for non-spherical particles, and develop constitutive relations from CFD-DEM simulations that can represent stresses due to collisions between non-spherical particles. Despite the importance of non-spherical particles in many industries, approaches for the treatment of non-spherical particles in coarse-grained methods are lacking.

We have taken an idealised view of a fluidised bed reactor for the sole purpose of studying the hydrodynamical forces acting on elongated particle during fluidisation. No heat transfer, mass transfer, or chemical reactions, all of which are inherent to real fluidised bed reactors, were discussed. We also did not consider mixtures of biomass feedstock and an inert bed material, which is typically sand. In previous CFD-DEM simulations of mixtures in fluidised beds, sand particles have been approximated as spherical particles (Wang et al., 2018; Ma and Zhao, 2018). Contacts between the elongated particles presented in this paper and spherical particles can be achieved by updating the collision detection algorithm while there are a number of drag force expressions in the literature for isolated and arrays of spherical particles (Deen et al., 2007; Beetstra et al., 2007). Multiparticle hydrodynamic forces in the presence of particle mixtures have yet to be defined.

Although the dynamics of elongated particles in fluidised bed reactors has formed the basis of this paper, the numerical techniques, hydrodynamic force correlations, and collision detection schemes are applicable for the numerical study of multiphase flows involving elongated particles in other industrial processes or in geophysical flows. In terms of industrial apparatus, CFD-DEM has also been applied in the study of multiphase flows in cyclone separators (Chu et al., 2009, 2011), coupled circulating fluidised bed-cyclone arrangements (Chu and Yu, 2008; Wang et al., 2017), downer reactors (Zhao et al., 2010; Wu et al., 2010), and riser flows (Varas et al., 2017). Invariably, these studies approximate solid particles as spheres for ease of implementation when in real processes these particles are notably non-spherical. Thus, there is scope for further numerical investigations on these apparatus where the solid phase may be depicted as elongated particles such as spherocylinders or ellipsoids.

## Conflict of interest

The authors declared that there is no conflict of interest.

## Acknowledgements

## References

Agrawal, K., Loezos, P.N., Syamlal, M., Sundaresan, S., 2001. J. Fluid Mech. 445, 151–185.
Aharonov, E., Sparks, D., 1999. Phys. Rev. E 60, 6890.
Aharonov, E., Sparks, D., 2002. Phys. Rev. E 65, 051302.
Aidun, C.K., Clausen, J.R., 2010. Annu. Rev. Fluid Mech. 42, 439.
Alauddin, Z.A.B.Z., Lahijani, P., Mohammadi, M., Mohamed, A.R., 2010. Renew. Sustain. Energy Rev. 14, 2852.
Amritkar, A., Deb, S., Tafti, D., 2014. J. Comput. Phys. 256, 501.
Anderson, J., Dick, E., Degrez, G., Grundmann, R., Degroote, J., Vierendeels, J., 1995. Computational Fluid Dynamics the Basics with Applications. McGraw-Hill, New York.
Andrews, M., O'Rourke, P., 1996. Int. J. Multiph. Flow 22, 379.
Andrews, Loezos, P.N., Sundaresan, S., 2005. Industr. Eng. Chem. Res. 44, 6022.
Antypov, D., Elliott, J.A., 2011. EPL (Europhys. Lett.) 94, 50004.
Arcen, B., Ouchene, R., Khalij, M., Taniére, A., 2017. Phys. Fluids 29, 093301.
Aydin, B., Larachi, F., 2005. Chem. Eng. Sci. 60, 6687.
Azmir, J., Hou, Q., Yu, A., 2018. Powder Technol. 323, 238.
Balevicius, R., Kacianauskas, R., Mroz, Z., Sielamowicz, I., 2011. Adv. Powder Technol. 22, 226.
Bao, J., Yuan, P., Schaefer, L., 2008. J. Comput. Phys. 227, 8472.
Bauerheim, M., Jaravel, T., Esclapez, L., Riber, E., Gicquel, L.Y.M., Cuenot, B., Cazalens, M., Bourgois, S., Rullaud, M., 2015. J. Eng. Gas Turbines Power 138, 061503.
Beetstra, R., van der Hoef, M.A., Kuipers, J.A.M., 2007. AIChE J. 53, 489.

Benyahia, S., Sundaresan, S., 2012. Powder Technol. 220, 2. selected Papers from the 2010 NETL Multiphase Flow Workshop.

Berzi, D., Thai-Quang, N., Guo, Y., Curtis, J., 2016. Phys. Rev. E 93, 040901.

Bing, R., Wenqi, Z., Xiaofeng, J., Baosheng, J., Zhulin, Y., 2014. Can. J. Chem. Eng. 92, 928.

Boer, L., Buist, K.A., Deen, N.G., Padding, J.T., Kuipers, J.A.M., 2018. Powder Technol. 329, 332.

Boon, C., Houlsby, G., Utili, S., 2013. Powder Technol. 248, 94. discrete Element Modelling.

Bouzidi, M., Firdaouss, M., Lallemand, P., 2001. Phys. Fluids 13, 3452.

Brunton, S.L., Proctor, J.L., Kutz, J.N., 2016. Proc. Nat. Acad. Sci. 201517384.

Buist, K.A., Jayaprakash, P., Kuipers, J.A.M., Deen, N.G., Padding, J.T., 2017. AIChE J. 63, 5335.

Campbell, C.S., Gong, A., 1986. J. Fluid Mech. 164, 107–125.

Capecelatro, J., Desjardins, O., 2013. J. Comput. Phys. 238, 1.

Chan, W.M., 2009. Comput. Fluids 38, 496.

Chapman, S., Cowling, T., Burnett, D., Cercignani, C., 1990. The Mathematical Theory of Non- uniform Gases: An Account of the Kinetic Theory of Viscosity, Thermal Conduction and Diffusion in Gases. Cambridge Mathematical Library, Cambridge University Press.

Cheng, G.C., Farmer, R., 2006. J. Propul. Power 22, 1373.

Chesshire, G., Henshaw, W., 1990. J. Comput. Phys. 90, 1.

Chu, K., Yu, A., 2008. Powder Technol. 179, 104.

Chu, K., Wang, B., Yu, A., Vince, A., 2009. Powder Technol. 193, 235.

Chu, K., Wang, B., Xu, D., Chen, Y., Yu, A., 2011. Chem. Eng. Sci. 66, 834.

Clarke, D.A., Sederman, A.J., Gladden, L.F., Holland, D.J., 2018. Industr. Eng. Chem. Res. 57, 3002.

Cleary, P.W., Sawley, M.L., 2002. Appl. Math. Model. 26, 89.

Clift, R., Grace, J., Weber, M., 2005. Bubbles, Drops,Particles, Dover Civil and Mechanical Engineering Series. Dover Publications.

Coetzee, C., 2017. Powder Technol. 310, 104.

Cortes, C., Gil, A., 2007. Prog. Energy Combust. Sci. 33, 409.

Cui, H., Grace, J.R., 2007. Chem. Eng. Sci. 62, 45.

Cundall, P., 1971. Proc. Symp. Int. Soc. Rock Mech. 2, 2.

Cundall, P., Strack, O., 1979. Geotechnique 21, 47.

Dasgupta, S., Atta, A., 2018. Chem. Eng. Process.- Process Intensif. 128, 149.

Deen, N.G., van Sint Annaland, M., van der Hoef, M.A., Kuipers, J.A.M., 2007. Chem. Eng. Sci. 62, 28.

Deen, N.G., Kriebitzsch, S.H.L., van der Hoef, M.A., Kuipers, J.A.M., 2012. Chem. Eng. Sci. 81, 329.

Deen, N.G., Peters, E.A.J.F., Padding, J.T., Kuipers, J.A.M., 2014. Chem. Eng. Sci. 116, 710.

Dejaloud, A., Vahabzadeh, F., Habibi, A., 2018. Fuel Process. Technol. 171, 265.

de Josselin de Jong, G., Verrujit, A., 1969. Cah. Grpe fr. Etud. Rheol. 2, 73.

Dellar, P.J., 2003. J. Comput. Phys. 190, 351.

den Akker, H.E.V., 2018. Curr. Opin. Chem. Eng. 21, 67.

Deresiewicz, H., 1958. Adv. Appl. Mech. 5, 233.

Desobgo, S.C.Z., 2018. Modernization of fermenters for large-scale production in the food and beverage industry. In: Panda, S.K., Shetty, P.H. (Eds.), Innovations in Technologies for Fermented Food and Beverage Industries. Springer International Publishing, Cham, pp. 189–220.

d'Humiéres, D., Ginzburg, I., Krafczyk, M., Lallemand, P., Luo, L.-S., 2002. Philos. Trans. Roy. Soc. London A: Math. Phys. Eng. Sci. 360, 437.

Di Felice, R., 1994. Int. J. Multiph. Flow 20, 153.

Dong, K., Wang, C., Yu, A., 2015. Chem. Eng. Sci. 126, 500.

Dong, K., Wang, C., Yu, A., 2015. Chem. Eng. Sci. 126, 500.

Dorostkar, O., Carmeliet, J., 2018. Rock Mech. Rock Eng. 51, 3281.

Džiugys, A., Peters, B., 2001. Granular Matter 3, 231.

Džiugys, A., Peters, B., 2001. Int. J. Numer. Anal. Meth. Geomech. 25, 1487.

Ergun, S., 1952. Chem. Eng. Prog. 48, 89.

Favier, J., Abbaspour-Fard, M., Kremmer, M., Raji, A., 1999. Eng. Comput. 16, 467.

Feng, Z.-G., Michaelides, E.E., 2004. J. Comput. Phys. 195, 602.

Fitzgerald, B.W., 2011. Criticality and force distribution in a lattice gas model of a sheared granular medium Ph.D. thesis. University of Limerick, Ireland.

Fitzgerald, B.W., Corcoran, D., 2005. Proceedings of 5th International Conference Powders and Grains, vol. 2, pp. 773–778.

Fitzgerald, B.W., Clancy, I., Corcoran, D., 2014. Phys. A 410, 582.

Fitzgerald, B.W., Padding, J.T., van Santen, R., 2017. Phys. Rev. E 95, 013307.

Friedrich, R., Httl, T., Manhart, M., Wagner, C., 2001. Comput. Fluids 30, 555.

Frisch, U., Hasslacher, B., Pomeau, Y., 1986. Phys. Rev. Lett. 56, 1505.

Gan, J., Zhou, Z., Yu, A., 2016. Chem. Eng. Sci. 144, 201.

Ganser, G.H., 1993. Powder Technol. 77, 143.

Gao, Z.-K., Yang, Y.-X., Fang, P.-C., Jin, N.-D., Xia, C.-Y., Hu, L.-D., 2015. Sci. Rep. 5, 8222.

Gavze, E., Shapiro, M., 1997. Int. J. Multiph. Flow 23, 155.

Geldart, D., 1973. Powder Technol. 7, 285.

Gidaspow, D., 1994. Multiphase Flow and Fluidization: Continuum and Kinetic Theory Descriptions. Academic Press Inc, London.

Ginzbourg, I., d'Humières, D., 1996. J. Stat. Phys. 84, 927.

Goniva, C., Kloss, C., Deen, N.G., Kuipers, J.A.M., Pirker, S., 2012. Particuology 10, 582.

Govender, N., Wilke, D.N., Wu, C.-Y., Khinast, J., Pizette, P., Xu, W., 2018. Chem. Eng. Sci. 188, 34.

Guan, Y., Guadarrama-Lara, R., Jia, X., Zhang, K., Wen, D., 2017. Adv. Powder Technol. 28, 1486.

Gu, Y., Ozel, A., Kolehmainen, J., Sundaresan, S., 2019. J. Fluid Mech. 860, 318–349.

Guo, Y., Wassgren, C., Ketterhagen, W., Hancock, B., James, B., Curtis, J., 2012. J. Fluid Mech. 713, 1–26.

Guo, Y., Wassgren, C., Ketterhagen, W., Hancock, B., Curtis, J., 2012. Powder Technol. 228, 193.

Guo, Q., Chen, X., Liu, H., 2012. Fuel 94, 551.

Guo, Y., Wassgren, C., Ketterhagen, W., Hancock, B., Curtis, J., 2012. Powder Technol. 228, 193.

Guo, Y., Wassgren, C., Hancock, B., Ketterhagen, W., Curtis, J., 2013. Phys. Fluids 25, 063304.

Gutmann, B., Cantillo, D., Kappe, C.O., 2015. Angew. Chem. Int. Ed. 54, 6688.

Haider, A., Levenspiel, O., 1989. Powder Technol. 58, 63.

Happel, J., Brenn, H., 1983. Low Reynolds Number Hydrodynamics: with Special Applications to Particulate Media. Springer Science & Business Media.

Hardy, J., de Pazzis, O., Pomeau, Y., 1976. Phys. Rev. A 13, 1949.

Harris, S.E., Crighton, D.G., 1994. J. Fluid Mech. 266, 243?276.

Haustein, M., Gladkyy, A., Schwarze, R., 2017. SoftwareX 6, 118.

He, L., Tafti, D., 2018. Powder Technol. 335, 409.

He, Y., Yan, S., Wang, T., Jiang, B., Huang, Y., 2016. Powder Technol. 287, 264.

Hejazi, B., Grace, J.R., Bi, X., Mahecha-Botero, A., 2014. Fuel 117, 1256.

Henshaw, W.D., Schwendeman, D.W., 2003. J. Comput. Phys. 191, 420.

Hill, R.J., Kock, D.L., Ladd, A.J., 2001. J. Fluid Mech. 448, 243.

Hilton, J., Mason, L., Cleary, P., 2010. Chem. Eng. Sci. 65, 1584.

Holst, J.M.F.G., Rotter, J.M., Ooi, J.Y., Rong, G.H., 1999. J. Eng. Mech. 125.

Hölzer, A., Sommerfeld, M., 2008. Powder Technol. 184, 361.

Hoomans, B., Kuipers, J., Briels, W., van Swaaij, W., 1996. Chem. Eng. Sci. 51, 99.

Ignatenko, Yaroslav, Bocharov, Oleg, May, Roland, 2017. EPJ Web Conf. 159, 00014.

Jafari, A., Zamankhan, P., Mousavi, S., Pietarinen, K., 2008. Chem. Eng. J. 144, 476.

Jenkins, J.T., Savage, S.B., 1983. J. Fluid Mech. 130, 187–202.

Jiang, S., Li, T., Tan, Y., 2015. Procedia Eng. 102, 1803.

Jieqing, G., Zongyan, Z., Aibing, Y., 2016. AIChE J. 62, 62.

Joardder, M.U., Kumar, C., Karim, M., 2017. Int. J. Multiph. Flow 95, 101.

Kafui, K., Thornton, C., Adams, M., 2002. Chem. Eng. Sci. 57, 2395.

Kandhai, D., Koponen, A., Hoekstra, A., Kataja, M., Timonen, J., Sloot, P., 1999. J. Comput. Phys. 150, 482.

Kapteijn, F., Nijhuis, T., Heiszwolf, J., Moulijn, J., 2001. Catal. Today 66, 133.

Kass, R.E., 1990. J. Am. Stat. Assoc. 85, 594.

Katagiri, J., Matsushima, T., Yamada, Y., 2010. Granular Matter 12, 491.

Ke, C., Shu, S., Zhang, H., Yuan, H., Yang, D., 2018. Powder Technol. 325, 134.

Ke, C., Shu, S., Zhang, H., Yuan, H., 2018. Appl. Math. Model. 64, 556.

Ketterhagen, W., Bharadwaj, R., Hancock, B.C., 2010. Int. J. Pharm. 392, 107.

Kildashti, K., Dong, K., Samali, B., Zheng, Q., Yu, A., 2018. Chem. Eng. Sci. 177, 1.

Koblitz, A., Lovett, S., Nikiforakis, N., Henshaw, W., 2017. J. Comput. Phys. 343, 414.

Komossa, H., Wirtz, S., Scherer, V., Herz, F., Specht, E., 2014. Powder Technol. 264, 96.

Koza, J.R., 1994. Stat. Comput. 4, 87.

Kremer, D., Hancock, B., 2006. J. Pharm. Sci. 95, 517.

Kreutzer, M.T., Kapteijn, F., Moulijn, J.A., Heiszwolf, J.J., 2005. Chem. Eng. Sci. 60, 5895.

Krüger, T., Kusumaatmaja, H., Kuzmin, A., Shardt, O., Silva, G., Viggen, E.M., 2017. The Lattice Boltzmann Method: Principles and Practice. Springer.

Kruggel-Emden, H., Vollmari, K., 2016. Powder Technol. 29, 1.

Kruggel-Emden, H., Simsek, E., Rickelt, S., Wirtz, S., Scherer, V., 2007. Powder Technol. 171, 157.

Kuang, S., LaMarche, C., Curtis, J., Yu, A., 2013. Powder Technol. 239, 319.

Kumar, P., Coronel, P., Simunovic, J., Truong, V., Sandeep, K., 2007. J. Food Sci. 72, E177.

Kumar, A., Jones, D.D., Hanna, M.A., 2009. Energies 2, 556.

Kumar, R., Sarkar, A., Ketterhagen, W., Hancock, B., Curtis, J., Wassgren, C., 2018. AIChE J. 64, 1986.

Ladd, A.J., 1994. J. Fluid Mech. 271, 311.

Ladd, A., Verberg, R., 2001. J. Stat. Phys. 104, 1191.

Latzel, M., Luding, S., Herrmann, H.J., 2000. Granular Matter 2, 123.

Latzel, M., Luding, S., Herrmann, H.J., Howell, D.W., Behringer, R.P., 2003. Eur. Phys. J. E 11, 325.

Lbbert, A., Larson, B., 1990. Chem. Eng. Sci. 45, 3047.

Lee, H., Balachandar, S., 2010. J. Fluid Mech. 657, 89.

Lee, H., Balachandar, S., 2017. Int. J. Multiph. Flow 88, 116.

Lee, S.Y., Hyun, J.Y., 2015. Biomed. Eng. Lett. 5, 289.

Lees, A.W., Edwards, S.F., 1972. J. Phys. C: Solid State Phys. 5, 1921.

Leith, D., 1987. Aerosol Sci. Technol. 6, 153.

Li, J., Zhang, J., Ge, W., Liu, X., 2004. Chem. Eng. Sci. 59, 1687.

Li, Z., Favier, J., D'Ortona, U., Poncet, S., 2016. An immersed boundary-lattice Boltzmann method for single-and multi-component fluid flows. J. Comput. Phys. 304, 424–440.

Li, L., Remmelgas, J., van Wachem, B.G., von Corswant, C., Folestad, S., Johansson, M., Rasmuson, A., 2016. KONA Powder Particle J. 33, 264.

Li, L., Zou, X., Wang, H., Zhang, S., Wang, K., 2018. Int. J. Multiph. Flow 101, 24.

Lin, X., Ng, T.-T., 1995. Int. J. Numer. Anal. Meth. Geomech. 19, 653.

Lindborg, H., Lysberg, M., Jakobsen, H.A., 2007. Chem. Eng. Sci. 62, 5854.

Lin, Z., Fang, H., Tao, R., 1996. Phys. Rev. E 54, 6323.

Link, J., Cuypers, L., Deen, N., Kuipers, J., 2005. Chem. Eng. Sci. 60, 3425.

Liu, D., van Wachem, B.G.M., Mudde, R.F., Chen, X., van Ommen, J.R., 2016. AIChE J. 62, 2259.

Lohse, D., Bergmann, R., Mikkelsen, R., Zeilstra, C., van der Meer, D., Versluis, M., van der Weele, K., van der Hoef, M., Kuipers, H., 2004. Phys. Rev. Lett. 93, 198003.

Lu, H., Ip, E., Scott, J., Foster, P., Vickers, M., Baxter, L.L., 2010. Fuel 89, 1156.

Lu, L., Gopalan, B., Benyahia, S., 2017. Industr. Eng. Chem. Res. 56, 7865.

Luo, L.-S., 1997. J. Stat. Phys. 88, 913.

Ma, H., Zhao, Y., 2018. Powder Technol. 336, 533.

Ma, H., Xu, L., Zhao, Y., 2017. Powder Technol. 314, 355.

Mahajan, V.V., Nijssen, T.M., Fitzgerald, B.W., Hofman, J., Kuipers, J.A.M., Padding, J. T., 2017. EPJ Web Conf. 140, 06019.

Mahajan, V.V., Padding, J.T., Nijssen, T.M.J., Buist, K.A., Kuipers, J.A.M., 2018. AIChE J. 64, 1573.

Mahajan, V.V., Nijssen, T.M.J., Kuipers, J.A.M., Padding, J.T., 2018. Chem. Eng. Sci. 192, 1105.

Marigo, M., Stitt, E.H., 2015. KONA Powder Particle J. 32, 236.

Marschall, T., Teitel, S., 2018. Phys. Rev. E 97, 012905.

Matsushima, T., Saomoto, H., 2002. In: Mestat (Ed.), NUMGE2002: Numerical Methods in Geotechnical Engineering, pp. 239–246.

Mattisson, T., Keller, M., Linderholm, C., Moldenhauer, P., Rydén, M., Leion, H., Lyngfelt, A., 2018. Fuel Process. Technol. 172, 1.

Mei, R., Luo, L.-S., Shyy, W., 1999. J. Comput. Phys. 155, 307.

Mei, Y., Zhao, M., Lu, B., Chen, S., Wang, W., 2017. Particuology 31, 42.

Mema, I., Mahajan, V.V., Fitzgerald, B.W., Kuipers, J.A.M., Padding, J.T., 2017. In: Proceedings of 12th International Conference on CFD in Oil and Gas, Metallurgical and Process Industries.

Mema, I., Mahajan, V.V., Fitzgerald, B.W., Padding, J.T., 2019. Chem. Eng. Sci. 195, 642.

Mittal, R., Iaccarino, G., 2005. Annu. Rev. Fluid Mech. 37, 239.

Mohamad, A.A., 2011. Lattice Boltzmann method: Fundamentals and Engineering Applications with Computer Codes. Springer Science & Business Media.

Molino, A., Chianese, S., Musmarra, D., 2016. J. Energy Chem. 25, 10.

Mountrakis, L., Lorenz, E., Hoekstra, A.G., 2017. Phys. Rev. E 96, 013302.

Mukherjee, S., Zarghami, A., Haringa, C., van As, K., Kenjere, S., den Akker, H.E.V., 2018. Int. J. Heat Fluid Flow 70, 59.

Nan, W., Wang, Y., Wang, J., 2016. Adv. Powder Technol. 27, 2265.

Ng, T.-T., 1994. Comput. Geotech. 16, 153.

Nikoo, M.B., Mahinpey, N., 2008. Biomass Bioenergy 32, 1245.

Norton, T., Sun, D.-W., 2006. Trends Food Sci. Technol. 17, 600.

Oschmann, T., Hold, J., Kruggel-Emden, H., 2014. Powder Technol. 258, 304.

Otto, H., Kerst, K., Roloff, C., Janiga, G., Katterfeld, A., 2018. Particuology 40, 34.

Ouchene, R., Khalij, M., Arcen, B., Taniére, A., 2016. Powder Technol. 303, 33.

Ozel, A., Fede, P., Simonin, O., 2013. Int. J. Multiph. Flow 55, 43.

Ozel, A., Kolehmainen, J., Radl, S., Sundaresan, S., 2016. Chem. Eng. Sci. 155, 258.

Paudel, B., Feng, Z.-G., 2013. Powder Technol. 237, 134.

Peng, Z., Doroodchi, E., Luo, C., Moghtaderi, B., 2014. AIChE J. 60, 2000.

Peng, Z., Moghtaderi, B., Doroodchi, E., 2016. Adv. Powder Technol. 27, 19.

Peskin, C.S., 1972. J. Comput. Phys. 10, 252.

Peskin, C.S., 1977. J. Comput. Phys. 25, 220.

Peskin, C.S., 2002. Acta Numerica 11, 479–517.

Pio, D., Tarelho, L., Matos, M., 2017. Energy 120, 915.

Poschel, T., Schwager, T., 2004. Computational Granular Dynamics. Springer, Berlin, Heiderlberg, New York.

Pournin, L., Weber, M., Tsukahara, M., Ferrez, J.-A., Ramaioli, M., Liebling, T.M., 2005. Granular Matter 7, 119.

Radl, S., Sundaresan, S., 2014. Chem. Eng. Sci. 117, 416.

Rezaei, H., Sokhansanj, S., Lim, C.J., 2018. Chem. Eng. Process. – Process Intensif. 124, 222.

Ricard, F., Brechtelsbauer, C., Xu, X., Lawrence, C., 2005. Chem. Eng. Res. Des. 83, 794.

Richter, A., Nikrityuk, P.A., 2013. Powder Technol. 249, 463.

Rong, L., Dong, K., Yu, A., 2013. Chem. Eng. Sci. 99, 44.

Rothenburg, L., Bathurst, R.J., 1991. Comput. Geotech. 11, 315.

Roy, M.M., Dutta, A., Corscadden, K., 2013. Appl. Energy 108, 298.

Rubinstein, G.J., Derksen, J.J., Sundaresan, S., 2016. J. Fluid Mech. 788, 576–601.

Rubinstein, G.J., Ozel, A., Yin, X., Derksen, J.J., Sundaresan, S., 2017. J. Fluid Mech. 833, 599?630.

Rui, D., Bao-chang, S., 2010. J. Hydrodyn. Ser. B 22, 782.

Sagis, L.M., van der Linden, E., 2001. Phys. A 297, 303.

Sagis, L.M.C., Ramaekers, M., van der Linden, E., 2001. Phys. Rev. E 63, 051504.

Saito, S., Abe, Y., Koyama, K., 2017. Phys. Rev. E 96, 013317.

Sanjeevi, S.K.P., Padding, J.T., 2017. J. Fluid Mech. 820.

Sanjeevi, S.K.P., Kuipers, J.A.M., Padding, J.T., 2018. Int. J. Multiph. Flow 106, 325.

Sanjeevi, S.K.P., Zarghami, A., Padding, J.T., 2018. Phys. Rev. E 97, 043305.

Schäfer, J., Dippel, S., Wolf, D.E., 1996. J. Phys. I France 6, 5.

Schmidt, M., Lipson, H., 2009. Science 324, 81.

Schneiderbauer, S., Puttinger, S., Pirker, S., 2013. AIChE J. 59, 4077.

Schöllmann, S., 1999. Phys. Rev. E 59, 889.

Seelen, L., Padding, J., Kuipers, J., 2018. Chem. Eng. Sci. 189, 84.

Snider, D., 2001. J. Comput. Phys. 170, 523.

Sommerfeld, M., Lain, S., 2018. Powder Technol. 332, 253.

Sommerfeld, M., Qadir, Z., 2018. Int. J. Multiph. Flow 101, 212.

Son, S.R., Kim, S.D., 2006. Industr. Eng. Chem. Res. 45, 2689.

Stitt, E., 2002. Chem. Eng. J. 90, 47.

Succi, S., 2001. The Lattice Boltzmann Equation: for uid Dynamics and Beyond. Oxford University Press.

Svoboda, K., Pohoel, M., Hartman, M., Martinec, J., 2009. Fuel Process. Technol. 90, 629.

Tang, Y., Peters, E.A.J.F., Kuipers, J.A.M., Kriebitzsch, S.H.L., Hoef, M.A., 2015. AIChE J. 61, 688.

Tang, Y., Peters, E.A.J.F., Kuipers, J.A.M., 2016. AIChE J. 62, 1958.

Tatsumi, R., Yamamoto, R., 2012. Phys. Rev. E 85, 066704.

Tenneti, S., Garg, R., Subramaniam, S., 2011. Int. J. Multiph. Flow 37, 1072.

Tijskens, E., Ramon, H., Baerdemaeker, J., 2003. J. Sound Vib. 266, 493.

Ting, J.M., 1992. Comput. Geotech. 13, 175.

Tong, Z.B., Yang, R.Y., Chan, H.K., Yu, A.B., 2017. Multiphase ows in pharmaceutical applications. In: Yeoh, G.H. (Ed.), Handbook of Multiphase Flow Science and Technology. Springer, Singapore, pp. 1–24.

Trad, Z., Fontaine, J.-P., Larroche, C., Vial, C., 2016. Renewable Energy 98, 264. special Issue: New Horizons in Biofuels Production and Technologies.

Trunk, R., Marquardt, J., Thter, G., Nirschl, H., Krause, M.J., 2018. Comput. Fluids 172, 621.

Tsuji, Y., Kawaguchi, T., Tanaka, T., 1993. Powder Technol. 77, 79.

Tsuji, T., Narita, E., Tanaka, T., 2013. Adv. Powder Technol. 24, 565.

Valus, M.G., Fontoura, D.V.R., Serfaty, R., Nunhez, J.R., 2017. Can. J. Chem. Eng. 95, 2286.

van der Hoef, M.A., Ye, M., van Sint Annaland, M., Andrews, A.T., Sundaresan, S., Kuipers, J.A.M., 2006. In: Marin, G.B. (Ed.), Computational Fluid Dynamics, vol. 31. Academic Press, pp. 65–149.

van der Hoef, M., van Sint Annaland, M., Deen, N.G., Kuipers, J.A.M., 2008. Annu. Rev. Fluid Mech. 40, 47.

Varas, A.E.C., Peters, E.A.J.F., Kuipers, J.A.M., 2017. Industr. Eng. Chem. Res. 56, 5558.

Vega, C., Lago, S., 1994. Comput. Chem. (Oxford) 18, 55.

Versteeg, H., Malalasekera, W., 2007. An Introduction to Computational Fluid Dynamics the Finite Volume Method. Pearson Education.

Vollmari, K., Oschmann, T., Wirtz, S., Kruggel-Emden, H., 2015. Powder Technol. 271, 109.

Vollmari, K., Jaseviius, R., Kruggel-Emden, H., 2016. Powder Technol. 291, 506.

Vollmari, K., Oschmann, T., Kruggel-Emden, H., 2017. Powder Technol. 308, 101.

Wang, W., Li, J., 2007. Chem. Eng. Sci. 62, 208. fluidized Bed Application.

Wang, D., Wang, Y., Yang, B., Zhang, W., Lancaster, N., 2008. Sedimentology 55, 461.

Wang, J., van der Hoef, M., Kuipers, J., 2009. Chem. Eng. Sci. 64, 622.

Wang, S., Luo, K., Hu, C., Fan, J., 2017. Chem. Eng. Sci. 172, 199.

Wang, L.-J., Wei, G.-C., Duan, S.-P., Hou, Q.-F., 2018. Part. Sci. Technol. 1.

Wen, Y., Yu, Y., 1966. Chem. Eng. Prog. Symp. Ser. 62, 100.

Williams, J.R., Pentland, A.P., 1992. Eng. Comput. 9, 115.

Williams, P.T., Williams, E.A., 1999. J. Anal. Appl. Pyrol. 51, 107.

Wu, C.-Y., 2008. Particuology 6, 412.

Wu, C., Cheng, Y., Ding, Y., Jin, Y., 2010. Chem. Eng. Sci. 65, 542. 20th International Symposium in Chemical Reaction EngineeringGreen Chemical Reaction Engineering for a Sustainable Future.

Xiao, X., Tan, Y., Zhang, H., Deng, R., Jiang, S., 2017. Powder Technol. 314, 182. special Issue on Simulation and Modelling of Particulate Systems.

Xu, B., Yu, A., 1997. Chem. Eng. Sci. 52, 2785.

Xue, Y., Kelkar, A., Bai, X., 2016. Fuel 166, 227.

Yan, Z., Wilkinson, S.K., Stitt, E.H., Marigo, M., 2015. Comput. Particle Mech. 2, 283.

Yang, L., Padding, J.T., Kuipers, J.A.M., 2016. Chem. Eng. Sci. 152, 767.

Yang, L., Padding, J.T., Kuipers, J.A.M., 2016. Chem. Eng. Sci. 152, 783.

Yang, L., Padding, J., Buist, K., Kuipers, J., 2017. Chem. Eng. Sci. 174, 238.

Yin, X., Le, G., Zhang, J., 2012. Phys. Rev. E 86, 026701.

Yoshida, H., Nagaoka, M., 2010. J. Comput. Phys. 229, 7774.

Yu, Y., Mei, R., Shyy, W., 2003. New York: AIAA 953, 2003.

Yu, F., Zhang, S., Zhou, G., Zhang, Y., Ge, W., 2018. Powder Technol. 336, 415.

Zarghami, A., Padding, J.T., 2018. Adv. Powder Technol. 29, 1507.

Zarghami, A., Van den Akker, H.E.A., 2017. Phys. Rev. E 95, 043310.

Zastawny, M., Mallouppas, G., Zhao, F., van Wachem, B., 2012. Int. J. Multiph. Flow 39, 227.

Zeng, L., Najjar, F., Balachandar, S., Fischer, P., 2009. Phys. Fluids 21, 033302.

Zhang, H., Baeyens, J., Tan, T., 2012. Energy 48, 380.

Zhao, Y., Ding, Y., Wu, C., Cheng, Y., 2010. Powder Technol. 199, 2.

Zhao, T., Dai, F., Xu, N.W., Liu, Y., Xu, Y., 2015. Granular Matter 17, 763.

Zhong, W., Yu, A., Liu, X., Tong, Z., Zhang, H., 2016. Powder Technol. 302, 108.

Zhou, Z.-Y., Zou, R.-P., Pinson, D., Yu, A.-B., 2011. Industr. Eng. Chem. Res. 50, 9787.

Zhou, Z., Pinson, D., Zou, R., Yu, A., 2011. Chem. Eng. Sci. 66, 6128.

Zhou, Z., Jin, G., Tian, B., Ren, J., 2017. Int. J. Multiph. Flow 92, 1.

Zhou, F., Sun, G., Zhang, Y., Ci, H., Wei, Q., 2018. Sep. Purif. Technol. 193, 175.

Zhu, H., Zhou, Z., Yang, R., Yu, A., 2008. Chem. Eng. Sci. 63, 5728.

Ziegler, D.P., 1993. J. Stat. Phys. 71, 1171.